Antarctic Meteorites XXXIII

Papers presented to the Thirty-third Symposium on Antarctic Meteorites

June 8–9, 2010

NATIONAL INSTITUTE OF POLAR RESEARCH
TOKYO

国立極地研究所

Tuesday, June 8, 2010

0930 – 1200 **Registration** **Auditorium (2nd Floor)**

Oral sessions will be held in the auditorium, 2nd floor of the Main Building
** denotes speaker*

0955 – 1000 Opening Address

Chairs: Imae N. and Uesugi M.

1200 – 1330 – Lunch –

Chairs: Ito M. and Gucsik A.

Special Talk

Chair: Debaille V.

Wednesday, June 9, 2010

Chairs: Mikouchi T. and Park J.

Chairs: Fagan T. J. and Nyquist L. E.

Special Talk

Chair: Arai T.

Poster Session

Abstract only

ABSTRACTS

Variations of chemical composition of matrices among carbonaceous chondrites. K. Abe[1], N. Sakamoto[2], H. Kojima[3], A. N. Krot[4] and H. Yurimoto[1,2]. [1]Department of Natural History Sciences, Hokkaido University, Sapporo 060-0810, JAPAN. E-mail: abeken@ep.sci.hokudai.ac.jp, [2]Isotope Imaging Laboratory, Creative Research Institution Sousei, Hokkaido University, Sapporo, 001-0021, JAPAN, [3]Antarctic Meteorite Research Center, National Institute of Polar Research, Tachikawa, Tokyo 190-8518, JAPAN, [4]Hawai'i Institute of Geophysics and Planetology, School of Ocean and Earth Science and Technology, University of Hawai'i at Manoa, Honolulu, HI 96822, USA.

Introduction:

Fine-grained matrix materials are susceptible to the effect by aqueous alteration and thermal metamorphism in asteroid. Therefore the variations of chemical composition of fine-grained minerals thought to reflect the degree of aqueous alteration [1]. Acfer 094, classified in ungrouped carbonaceous chondrite, is believed to one of the most primitive meteorites. This meteorite contains highly abundance of presolar grains [2] and cosmic symplectite (COS) [3] in the matrix. The COS has not been discovered in other carbonaceous chondrite [4]. The uniqueness of Acfer 094 may be appeared in chemical characteristics of the matrix. In this report, we newly studied 8 CM2 and 1 CO3 Yamato meteorites (Y-86034, Y-86039, Y-86686, Y-86688, Y-86693, Y-86694, Y-980165, Y-980183, Y-980239) in addition to previous work [5] and observed variations of chemical composition of fine grains (<~μm) in matrices of various carbonaceous chondrites to compare with Acfer 094.

Expermental:

We prepared polished thin sections of 36 carbonaceous chondrites in this study: C-ung.: Acfer 094, Adelaide, MAC87300, Tagish Lake; CI: Alais, Orgueil, Y-980115, Y-980134; CM2: Acfer 331, Murchison, Y-86034, Y-86039, Y-86686, Y-86688, Y-86693, Y-86694, Y-980050, Y-980070, Y-980085, Y-980086, Y-980093, Y-980094, Y-980183, Y-980239; CR2: Acfer 209, NWA 530, NWA 852, Renazzo; CO3: ALHA77307, Colony, Y-81025, Y-980165; CV3: Allende, Vigarano, Y-980010, Y-980011. The matrices were analyzed by X-ray elemental mapping technique using an energy dispersive X-ray spectrometer (EDS, Oxford INCA Energy) attached on a field-emission type scanning electron microprobe (FE-SEM, JEOL JSM-7000F). X-ray elemental maps of C, O, Na, Mg, Al, Si, P, S, Ca, Cr, Fe, and Ni were prepared for one or two regions of 45 x 60 μm^2 matrix area for each thin section. The X-ray maps were acquired by 15 kV electron probe with 10 nA beam current and composed by of 0.2 μm pixels, but the spatial resolution of the X-ray maps is about 1 μm due to the electron beam broadening in the thin sections. The measurement time for each pixel was about 0.5 s. Calculations of chemical compositions from X-ray spectra were performed by a commercial application "INCA Quant map". A value having the greatest number of pixel defined average value of matrix.

Results and Discussion:

The average values of fine-grained matrix are plotted onto Fe-Si-Mg ternary diagram (Fig. 1). In this diagram, the matrix compositions among carbonaceous chondrites lie along an approximately linear trend. The general trend is from the top of Fe towards the Si-Mg side with almost constant Mg/Si ratio, because of the aqueous alteration on their parent body [1]. The CM chondrites analyzed in this study have lower Fe compositions than previous work [5]. Y-980239 is plotted near the CI chondrites which is heavily altered CM chondrite with little remained olivine grains.

Previous work reported highly variable compositions in Al, S and Ca contents of fine-grained matrix minerals less than ~μm among the carbonaceous chondrite groups [5]. Fig. 2 shows Ca/Al vs. S/Al ratios for matrices of updated chondrites and Acfer 094 matrices normarized to CI chondrite. Previous results of various carbonaceous groups represent as shaded areas. CM chondrites in this study are plotted around the previous CM region differ from Acfer 094 although bulk composition of

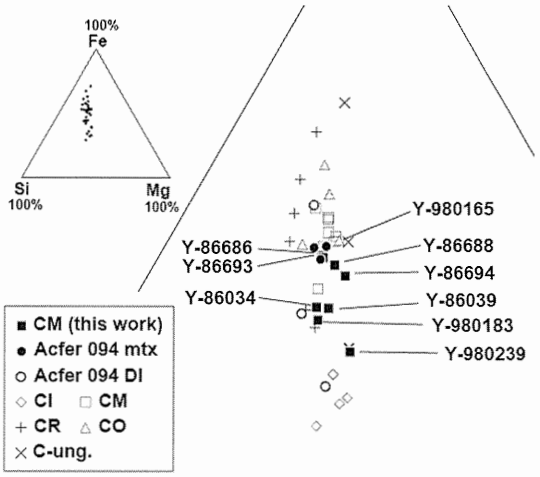

Fig. 1. Ternary Fe-Si-Mg wt% diagram plotted on the average composition of fine-grained matrices and dark inclusions in 36 carbonaceous chondrites.

Acfer 094 is similar to CM chondrite [6, 7]. The Fe contents of the fine-grained matrices in CM chondrites indicated the amount of serpentine minerals are not always related to S/Al and Ca/Al ratios (Fig. 3) whereas dark inclusions of Acfer 094 show smaller ratios of S/Al and Ca/Al ratios than the matrix. The micro scale elemental redistribution of CM chondrites by aqueous alteration may be different from that of Acfer 094.

References:

[1] Zolensky M. et al. (1993) *Geochim. Cosmochim. Acta* **57**, 3123-3148. [2] Newton J et al. (1995) *Meteoritics* **30,** 47-56. [3] Sakamoto N. et al. (2007) *Science* **317,** 231-233. [4] Abe K. et al. (2008) *Lunar Planet. Sci. XXXIX*, Abstract #1509 [5] Abe K. et al. (2009) *The 32nd Symposium on Antarctic Meteorites,* 1. [6] Wlotzka F. (1991) *Meteoritics* **26**, 255 - 262. [7] Spettel B. et al. (1992) *Meteoritics* **27**, 290 - 291.

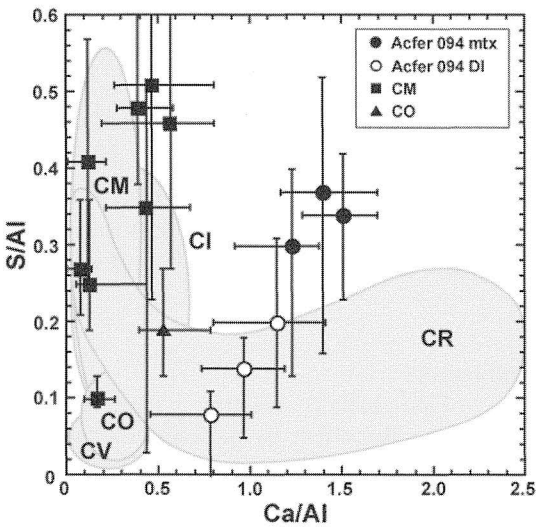

Fig. 2. Ca/Al vs. S/Al for matrices of various carbonaceous chondrite groups normalized to CI chondrite. Each symbol shows average value of matix. Error bars correspond to half maximum full width of the average value on composition histogram. Shaded areas are previous work [5]. mtx = matrix, DI = Dark inclusion.

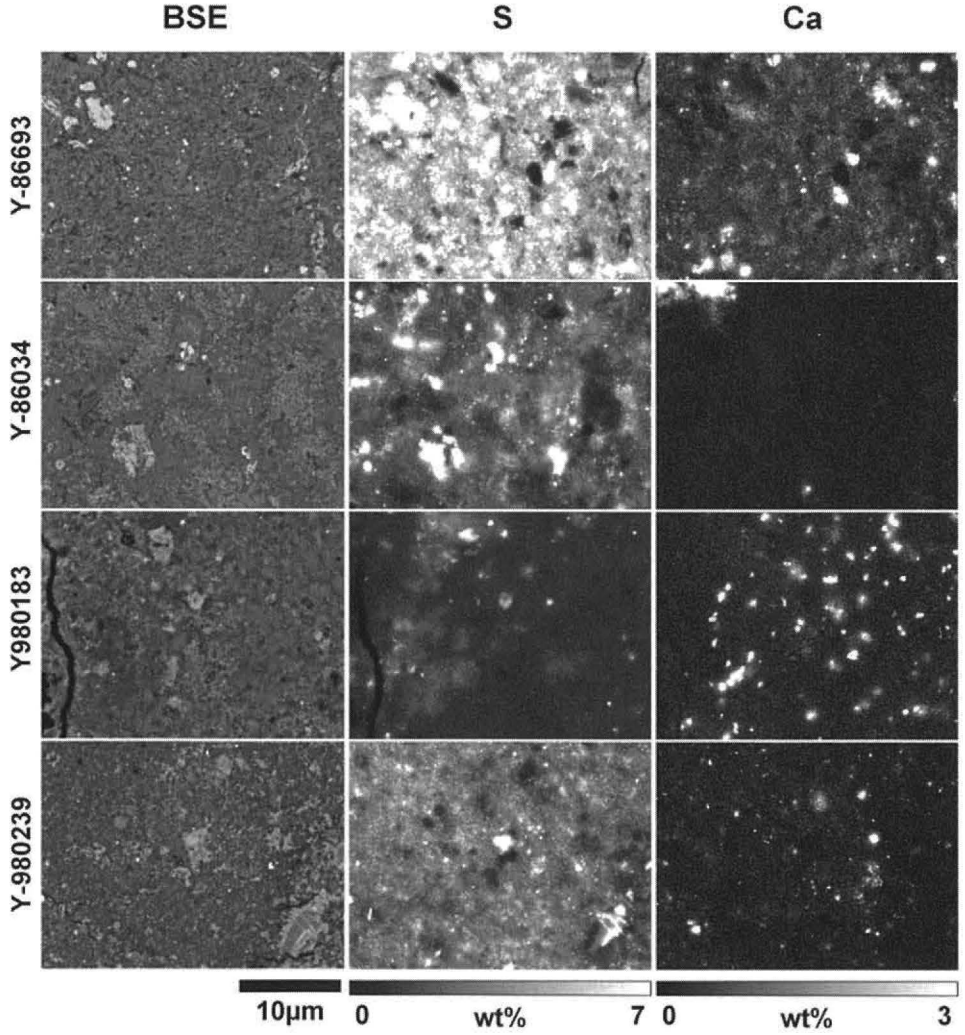

Fig. 3. Back scattered electron images and quantitative X-ray elemental maps of fine-grained matrix of four CM chondrites in this study.

U-PB AGE DATING AND MINERALOGY OF A KREEP BASALT CLAST IN LUNAR METEORITE NWA 4485. T. Arai[1], M. Yoshitake[2], T. Tomiyama[2], T. Niihara[2], T. Yokoyama[2], H. Kaiden[2], K. Misawa[2], and A. J. Irving[3]. [1]Planetary Exploration Research Center, Chiba Institute of Technology, 2-17-1 Tsudanuma, Narashino, Chiba 275-0016, Japan (tomoko.arai@it-chiba.ac.jp). [2]Antarctic Meteorite Research Center, National Institute of Polar Research, 10-3 Midoricho, Tachikawa, Tokyo 190-8518, Japan. [3]University of Washington, Seattle, USA.

Introduction: Duration, distribution, and nature of pre-mare magmatism of the Moon remains loosely constrained. Extensive late basin-forming events around 3.9 Ga and subsequent mare basalt eruption erased most of the record of the early lunar history. KREEP-rich rocks and breccias mostly predate the mare basalt volcanism, and thus hold clues to understanding the pre-mare magmatism. The U-Pb system within refractory zircon is the most reliable isotopic chronometers to date the pre-mare volcanism, because its robustness in the event of isotopic disturbance. Lunar meteorite NWA 4485 is a KREEP-rich polymict regolith breccias with high Th content [1]. Here, we present mineralogical study and U-Pb age dating of a KREEP basalt clast in NWA 4485 to further constrain the composition and timing of pre-mare KREEP magmatism.

Sample and method: A thick section of NWA 4485 was used for this study. *In situ* U-Pb and Pb-Pb age dating of zircon were conducted by a sensitive high mass-resolution ion microprobe (SHRIMP II) at National Institute of Polar Research (NIPR). Mineralogical analyses were performed with JEOL JXA8200 electron microprobe.

Results:

Petrography: NWA 4485 is a polymict breccia, including mm-sized lithic clasts with variable texture and modal abundance, isolated mineral fragments, and glasses. Fractures across the samples are filled with terrestrial calcite. Mineral fragments are pyroxene, olivine, plagioclase, ilmenite, chromite, merrilite, apatite, baddeleyite, zircon, k-feldspar, silica, Fe-metal, and FeS. Pyroxene fragments generally show a few micron to 5 micron thick exsolution lamellae. The breccia matrix consists of heterogeneous glass including degraded mineral fragments. Some matrix glasses are vesiculated. Fragments of K-feldspar and silica intergrowth are widely distributed in the matrix. Glass spherules of a few tens to 300 micron in diameter are present, but not abundant relative to those in typical regolith breccias.

Mineralogy: A relatively coarse-grained KREEP basalt is 1.7 x 1 mm in size, showing intersertal texture (Fig. 1). It consists of plagioclase, pyroxene, ilmenite, K-feldspar, merrilite, apatite, zircon, baddelyite, and Si-rich glass. Grain sizes of pyroxene and plagioclase are up to 0.5 mm across. Chemical compositons of major minerals are relatively homogeneous: Na-rich plagioclase (An_{82-85}), co-existing Mg-rich pigeonite ($Wo_{7-15}En_{44-47}$, Fe#=49-52) and augite ($Wo_{29-36}En_{34-39}$, Fe#=41-48). Magnesian pigeonites predominate with augites as exsolution lamella of up to a few micron in thickness. The both pyroxenes include 1.0-1.3 wt% TiO_2 and Al_2O_3. Large grain of ilmenite (0.7 mm across) with up to 2.5 wt% MgO is present. Modal abundance of this clast is: 38 vol% plagioclase, 32 vol% pyroxenes, 22 vol% ilmenite, 6 vol% phosphates, and others.

U-Pb age: Three zircon grains co-existing with pyroxene and plagioclase in the KREEP basalt were analyzed. $^{207}Pb/^{206}Pb$ ages of the three zircons are 4154 ± 4 Ma, 4170 ± 26 Ma, and 4173 ± 6 Ma, respectively, showing a small discordance of U-Pb system (5−10%) (Fig. 2). Their uranium content ranges from 91 ppm to 131 ppm.

Discussions: The intersertal texture and the relatively coarse grain size imply an igneous origin of the KREEP basalt clast. The low Fe# of pyroxene and high An content of plagioclase are distinct from mineral compositions of the typical mare basalts. Subhedral shape and the large grain size of ilmenite and apatite suggests their appearance at an earlier crystallization stage. The high modal abundance of ilmenite and low Fe# of the pyroxenes also indicate that pyroxenes are depleted in FeO because of prior crystallization of ilmenite. The basalt clast is probably originated from a Ti and Na-rich melt with Mg/Fe ratio which is comparable or higher than that of mare basalt. Unlike mare basalts, ilmenite could be a liquidus phase in the KREEP basalt. Apollo KREEP basalts include minor amounts of ilmenites [2]. The high modal ilmenite may be due to a fact that the clast is not representative of the whole parent rock because of the small size of the clast relative to the coarse grain size. However, the ilmenite-rich nature has been recognized in other KREEP-rich alkali anorthosite clasts, i.e. 14305 [unpublished data]. Thus, the clast could represent a Ti-rich KREEP magma which has not been explored.

The zircon ages in the KREEP basalt clast imply that the age (~4160 Ma) represents the timing of

crystallization of the rock. The age of apatite in the "evolved basalt clast" which we expect is related to the "KREEP basalt clast" in our sample is much younger age (3937 Ma) [3] than that of the zircons in the KREEP basalt clast (~4170 Ma). The age difference may have resulted from a greater susceptibility of apatite to the isotopic disturbance relative to zircon [4, 5].

This study shows that a KREEP-rich magma with high Ti and Na content occurred at ~4160 Ma around the PKT region of the Moon. The heat source to generate the parent magma could be either the internal heating due to radioactive decay and/or the external heating by impact. The Ti, Na and KREEP-rich magma can be caused by either a late-stage crystallization of plutons intruded into the crust, or crystallization of large-scale impact melt pools which formed in the KREEP-rich crust.

References: [1] Connolly Jr., H. C. et al., (2007) Met. Bull. No. 91, MAPS, 42, A413-A466. [2] G.Ryder (1976) EPSL29, 255-268. [3] Joy K. T. et al. (2009) LPS XXXX, Abstract #1708. [4] Cherniak D. J. et al. (1991) GCA, 55, 1663-1673. [5] Nemchin A. A. and Pidgeon R. T. (2008) LPS XXXIX, Abstract #1558.

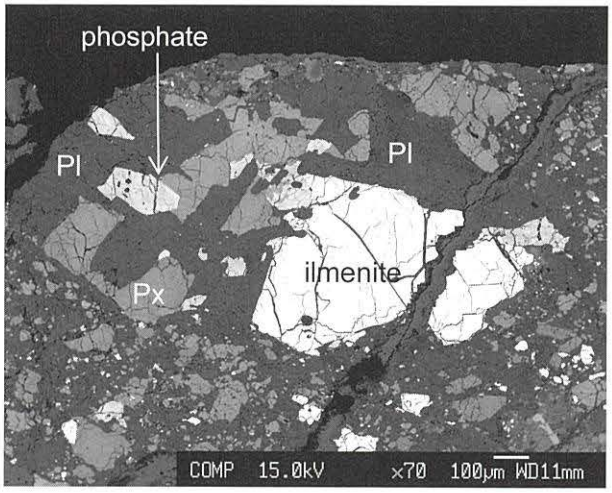

Fig. 1. Back-scattered electron image of the KREEP basalt clast. Pl: Plagioclase, Px; pyroxene.

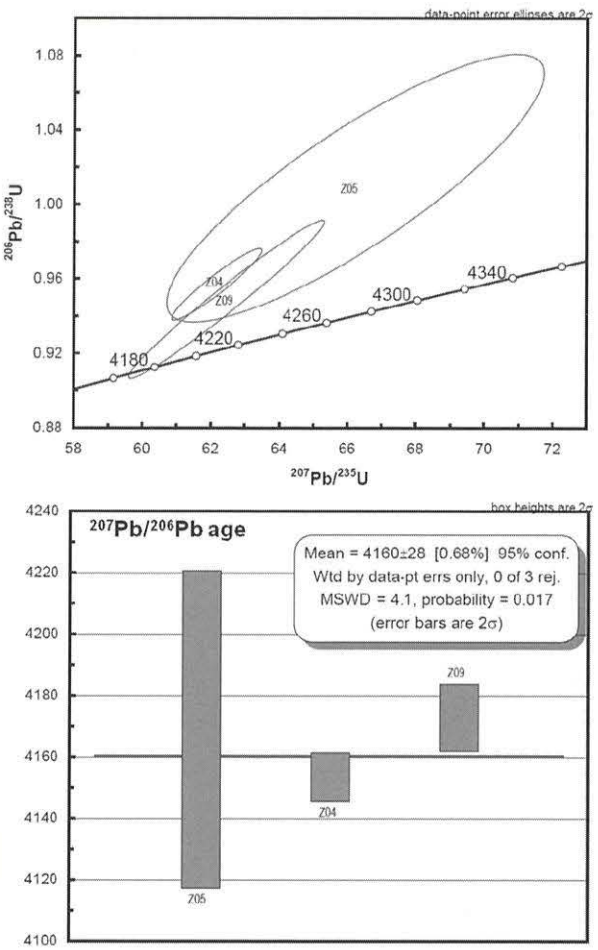

Fig. 2. U-Pb concordia plot and Pb-Pb age plot of the KREEP basalt clast.

Belgian contribution to the search for (micro)meteorites in Antarctica

Ph. Claeys[1], V. Debaille[2], S. Goderis[1], N. Mattielli[2], [1]Earth System Science, Vrije Universiteit Brussel, Pleinlaan 2, B-1050 Brussels, Belgium, phclaeys@vub.ac.be [2]Dept. Sciences de la Terre et de l'Environnement, Université Libre de Bruxelles, 50 av. F. D. Roosevelt, B-1050 Brussels, Belgium.

Belgium has been active in Antarctica since the 19th century [1]. In 1898, Adrien de Gerlache, and his crew were the first to spend a whole winter South of the Antarctic Circle, when their exploration vessel "Belgica" intentionally sailed into the pack ice and became beset. During this winter, the onboard international team of scientists made numerous observations in the fields of meteorology, biology, geology, cartography etc. In 1957, as part of the Antarctica Program embedded in the International Geophysical Year, the station "King Baudouin" was build in one of the remaining open zone, on a small ice shelf in Dronning Maud Land. The station operated until 1967 before closing definitively, because of budgetary shortcomings. In 1970, Belgian activities in Antarctica were interrupted, although scientists remained active through participating in other nations programs. During its brief existence, King Baudouin station contributed greatly to the broad network of geophysical measurements carried out over the Southern Continent, including aerial photography and cartography. From the station, field expeditions led to a better knowledge of the geology, glaciology and topography of then still poorly known Sør Rondane region. Unfortunately, not all the field results were published. It is as part of the Belgian Antarctic Research Program that the first attempts were carried out to measure the amount of extraterrestrial material falling on Earth at the initiative of Edgard Picciotto from the Université Libre de Bruxelles (ULB). Most of the extraterrestrial contribution consists of fine (< mm) interplanetary dust particles (IDP); that of the larger, more impressive, meteorite fraction is limited and not well constrained. First, the determination of Ni abundances in South Pole precipitations led to ambiguous results and attention focused on the accumulation in ice of ^{53}Mn, a radioactive nuclide produced by the action of solar proton on IDP. The selection of the sampling site had to meet the following criteria, minimum snow accumulation, minimal terrestrial contamination and easy access to large ice volumes. The optimal site was selected on the East Antarctic plateau, where 3 tons of pre-thermonuclear bomb test (1952) ice was collected in 1968 and transported to Brussels. The measurements of the ^{53}Mn signal in slowly accumulated ice led to an estimate of the extraterrestrial flux on Earth of ~ 10^5 tons/yr [2], a value that withstood the test of time, and modern methodologies.

After more than 30 years of absence, the new Belgian base named "Princess Elisabeth" was officially open in February 2009. This "zero emission" station results from the efforts of Belgian polar explorer Alain Hubert, and the International Polar Foundation [3], which acts as the manager for logistics, technical, safety and general operations at and around the Station. The Belgian Federal Science Policy Office supports various research projects centered on the base. Princess Elisabeth is located on the Utsteinen ridge, at the foothills of the Sør Rondane mountains, in the Dronning Maud Land in East Antarctica [4] (coordinates 71°57' S – 23° 20' E). It is in this very same region that in 1969 a Japanese expedition recovered the first meteorites at the surface of blue ice fields. The Belgian base is thus ideally located to become a hub for meteorite research in the prolific Sør Rondane area.

The Earth Science groups at the two Brussels universities (VUB & ULB), which inherited the isotopic expertise developed by Edgard Picciotto, have joined force to carry out searches for (micro) meteorites in the fields of blue ice located near the base. In December 2009 – January 2010, the participation of Steven Goderis to the National Institute of Polar Research (NIPR), JARE 51 meteorite search expedition constituted the first initiative of this project, and made it possible for Belgium to obtain some basic knowledge in the field. During the next four years, under the label SAMBA (*Search for Antarctic Meteorites: Belgian Contribution*), the Belgian Federal Science Policy Office will support several expeditions, in collaboration with NIPR, to pursue meteorite collection. The philanthropic InBev-Bailler Latour foundation [5] also sponsors a project called MicroMetA (*Micrometeorites from Antarctica*) with the goal to recover the micrometeorites that accumulate in cracks and fractures of granitic and gneissic outcrops. Such small size extraterrestrial objects were first identified by [6] in the Transantarctic Mountains. A new facility is being established at the Royal Belgian of Natural Sciences for the curation and daily management of the collected meteorites.

The Earth System Science research unit at the VUB has a long experience in impact cratering, detection of meteoritic components and projectile identification using platinum group elements and isotopic signatures. Characterization of non-magmatic iron meteorites represents another research interest. The ULB group confirms a strong and long expertise in isotopic geochemistry. Besides

the more traditional isotopic systems (heavy masses), like Pb, Nd, Hf, and W. Expertise also exists in the non-traditional heavy stable isotopes, such as Fe, Zn, Cu and Cd, special focus is set on the potential discrepancies between Earth and primitive chondrites, and finally on the composition of the Earth as well as on the isotopic analyses of Martian meteorites (see presentation of V. Debaille this meeting).

The research on meteorites will be carried out in state of the art analytical facilities in Brussels and the Ghent University, where respectively a Nu-Plasma and a Neptune MC-ICP-MS are available, as well as clean labs (class 1000 & 100) specifically designed to carry out low-level high resolution isotopic preparations and analyses. Several other mass spectrometers (HR-ICP-MS, laser ablation etc.), as well as SEMs, TEMs, Raman and Field Emission Auger Spectroscopy are also available for the characterization of the recovered meteorites.

In the long tradition already established in 1897 by Adrien De Gerlache, international collaboration represents a major constituent of the Belgian Antarctic Meteorite Research Project.

References:

[1] Decleir H. and De Broyer C. (2001), VUB Brussels University Press, 366 p., [2] Bibron et al. (1974) *Earth & Planet. Sci. Letters,* 21, 109-116, [3] http://www.polarfoundation.org/, [4] http://www.antarcticstation.org/, [5] http://www.inbevbailletlatour.com/, [6] Rochette P. et al. (2008), *PNAS*, 105, 47, 18206-18211.

Isotopic Evidence for Mantle Overturn in Early Mars and its Geodynamic Consequences. V. Debaille[1], A.D. Brandon[2], C. O'Neill[3], Q.-Z. Yin[4], B. Jacobsen[5]
[1]Université Libre de Bruxelles, Brussels, Belgium. E-mail:vdebaill@ulb.ac.be. [2] Department of Earth and Atmospheric Sciences, University of Houston, Houston, TX. [3]Macquarie University, New South Wales, Australia. [4]University of California, Davis, CA. [5] Lawrence Livermore National laboratory, Livermore, CA.

Introduction:

Global-scale events that occur during early stages of planetary differentiation include metal-silicate segregation leading to core formation, giant impacts, large-scale melting resulting in magma ocean(s), and possibly subsequent mantle overturn. During the solidification of a magma ocean, crystallization proceeds from the bottom up [1,2]. Cumulates resulting from the last stages of crystallization at the top of the mantle, are enriched in incompatible trace elements, but also in Fe and hence, are denser than MgO-rich cumulates that crystallized earlier [3]. Because the denser cumulates are located at the top of the pile, an inverse density gradient exists which is unstable and likely results in mantle overturn [3-6]. Early large-scale mantle overturn may have been dramatic for the evolution of planets, but little is known about its occurrence and consequences, as geochemical evidence for mantle overturn is lacking. Martian meteorites offer a unique opportunity to investigate early planetary differentiation because they preserve geochemical signatures of ancient events [7]. Here, short and long-lived radioactive chronometers of ^{182}Hf-^{182}W ($t_{1/2}$= 9 million years (Myr)), ^{146}Sm-^{142}Nd ($t_{1/2}$= 103 Myr), ^{147}Sm-^{143}Nd ($t_{1/2}$= 106 billion years (Gyr)) and ^{176}Lu-^{176}Hf ($t_{1/2}$= 37.1 Gyr), are applied for 3 nakhlites, Nakhla, MIL-03346, and Yamato-000593, to resolve the timing of multiple early differentiation events in Mars including mantle overturn.

Results:

The three nakhlites show a restricted range in isotopic compositions with ^{176}Hf/^{177}Hf = 0.282998±31 to 0.283108±10 and ^{143}Nd/^{144}Nd= 0.512854±1 to 0.512873±1 (errors are 2σ) [8]. When corrected to a crystallization age of 1.27-1.36 Gyr (see compilation in [9]), these values correspond to $\varepsilon^{176}Hf_i$=+12.6 to +19.7 and $\varepsilon^{143}Nd_i$=+16.1 to +16.9 respectively. The $\varepsilon^{143}Nd_i$ compares well to that obtained in previous studies [10-13]. Using the terrestrial standard value of ^{142}Nd/^{144}Nd=1.1418402 measured during the analytical campaign for normalization, nakhlites have ε^{142}Nd=+0.61±0.01 to +0.67±0.03 (2σ). There is good agreement with a previous analysis of Nakhla of ε^{142}Nd=0.59±0.13 [7]. The ε^{176}Hf/ε^{143}Nd ratios of all nakhlites range from 0.8 to 1.2. This is consistent with melts derived from residues having experienced garnet segregation [14]. This is because of the large partition coefficient of Lu in garnet/majorite (though smaller in majorite [15]) compared to Hf, Nd and Sm. Hence, removing high Lu/Hf phases from cumulates will lower with time the ε^{176}Hf over the ε^{143}Nd, resulting in ε^{176}Hf/ε^{143}Nd<1, as observed in nakhlites.

Discussion:

Compared to the depleted shergottite, nakhlites have similar ε^{142}Nd of about +0.6 , but the two groups have ε^{182}W of -0.3 to +0.9 versus +3, respectively [7,16-20]. The homogeneous and seemingly uncomplicated isotopic signatures of nakhlites were used to constrain the timing of core segregation within the first 15 Myr after solar system condensation [18,19]. However, because the ε^{182}W of +3 in nakhlites are too high to be related solely to core-mantle separation [21-23], and because nakhlites do not plot in a two-stage evolution diagram for ^{142}Nd/^{144}Nd versus ^{143}Nd/^{144}Nd, a more complex four-stage evolution is considered and is modeled as follows.

In the first stage t_1 of the model an iron-rich core is segregated. Tungsten is strongly partitioned in metallic phases while Hf preferentially stays in silicate and oxides. This leaves a silicate residue that will be defined here as the primitive Martian mantle (PMM), which is consequently depleted in siderophile elements such as W. This first stage does not have any influence on the Lu/Hf and Sm/Nd ratios as these are lithophile elements, and PMM is identical to the chondritic uniform reservoir (CHUR) for these ratios. However, core segregation alone does not produce the high ε^{182}W values observed in nakhlites [21,23]. A second stage following core segregation, further increasing the Hf/W ratio, must be included during the life-time of ^{182}Hf (<~50 Myr after solar system condensation), and a third stage is added when ^{182}Hf is extinct, but ^{146}Sm still extant (between ~50 and ~500 Myr after solar system formation), in order to generate the high ε^{182}W anomalies decoupled from ε^{142}Nd. This third stage may be related to garnet or majoritic garnet segregation. As a consequence, the nakhlite ε^{182}W remained fixed and reflects the crystallization of nakhlites in the deep Martian mantle in stage 2 (Fig. 1). The lower than expected ε^{142}Nd records Sm/Nd fractionation from the segregation of garnet (Fig. 1). Finally, a fourth stage where nakhlite parental magma is produced corresponds to the crystallization age of nakhlites [8].

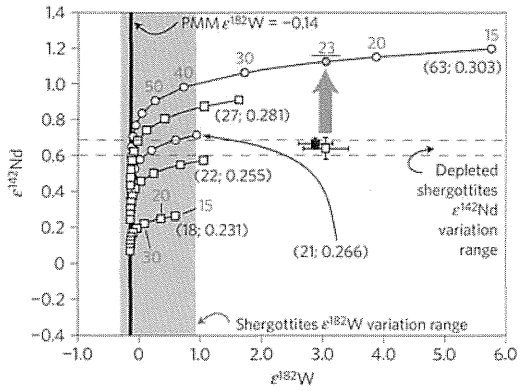

Fig. 1: $\varepsilon^{142}Nd$ vs. $\varepsilon^{182}W$ in the nakhlites from Debaille et al. [8]. Black square: Nakhla; white square: average value for all nakhlites ($\varepsilon^{142}Nd$: this study; $\varepsilon^{182}W$: [17,18]). Error bars are 2σ. Symbols on the curves represent the present-day $\varepsilon^{182}W$ and $\varepsilon^{142}Nd$ attained in a source region for the age indicated in Myr. ($^{147}Sm/^{144}Nd$; $^{180}Hf/^{183}W$) pairs are indicated for each curve. The grey arrow indicates the $\varepsilon^{142}Nd$ vs. $\varepsilon^{182}W$ value that nakhlite source should have reached when crystallizing in the majorite stability field (upper black curve) ~23 Myr after solar system formation if no garnet segregation had occurred after ^{182}Hf extinction.

The question is now to explain how mantle cumulates can experience garnet segregation 100 Myr after solar system formation, as evidenced in the nakhlite geochemical record. The inverse density gradient resulting from the solidification of a magma ocean is unstable and may result in mantle overturn [3-6]. Hot and less dense materials are brought from the deep parts of the martian mantle and may melt by adiabatic decompression [3]. To examine the potential implications of a mantle overturn to Mars evolution, a numerical model has been developed [8]. A striking implication of the overturn event is the scale and depth extent of melting accompanying it. Most of the mantle is at near solidus starting condition and can hence melt easily with any adiabatic decompression. Melting initiates very deep in the Martian mantle (>1400 km), and a 50% melt fraction is reached for depths of 700-800 km. As the large-scale upwellings reach the near surface, extreme melt fractions over 60% (maximum 65%) are reached in the immediate sub-lithosphere. Garnet and majoritic garnet are dense and negatively buoyant. They can be segregated from such low viscosity and partially molten cumulates because of their density contrasts [3,6]. The nakhlites hence provide the first geochemical evidence for a mantle overturn in Mars.

The overturn had important implications for martian tectonics. The sinking of dense subcrustal cumulate material is viscously coupled to the crust, and results in thickening of the crust over large-scale downwellings, and thinning above significant upwellings, that may have resulted in the martian dichotomy. Thickened crustal units are then susceptible to entrainment and recycled back into the convecting mantle, and a considerable portion (5-10%) of the primordial crust is lost this way.

Surprisingly, while mantle overturn was a large scale event, not all the martian mantle has been remodeled. The $\varepsilon^{142}Nd$ signatures of shergottites and ALH84001 [16,24] still record differentiation events that occurred 4.54 to 4.46 Gyr ago. This indicates that at least some portions of the martian mantle remained unchanged despite the mantle overturn.

References:

[1] Solomatov, V. S. and Stevenson, D. J. 1993 *J. Geophys. Res.* 98: 5391-5406. [2] Abe, Y. 1997 *Phys. Earth Planet. Inter.* 100: 27-39. [3] Elkins-Tanton, L. T. et al. 2005 *J. Geophys. Res.* 110: E12S01. [4] Hess, P. C. and Parmentier, E. M. 1995 *Earth Planet. Sci. Lett.* 134: 501- 514. [5] Elkins-Tanton, L. T. et al. 2003 *Meteorit. Planet. Sci.* 38: 1753-1771. [6] Elkins-Tanton, L. T. et al. 2005 *Earth Planet. Sci. Lett.* 236 1-12. [7] Harper, C. L. et al. 1995 *Science* 267: 213-217. [8] Debaille, V. et al. 2009 *Nature Geoscience* 2: 548-552. [9] Nyquist, L. E. et al. 2001 *Space Sci. Rev., Chronology and Evolution of Mars* 96: 105-164. [10] Misawa, K. et al. 2003 *Lun. Planet. Sci. Conf. XXXIV*#1556. [11] Shih, C.-Y. et al. 2006 *Lun. Planet. Sci. Conf. XXXVII*#1701. [12] Nakamura, N. et al. 1982 *Geochimica et Cosmochimica Acta* 46: 1555-1573. [13] Shih, C.-Y. et al. 1999 *Meteorit. Planet. Sci.* 34: 647-655. [14] Vervoort, J. D. and Patchett, J. 1996 *Geochim. Cosmochim. Acta* 60: 3717-3733. [15] Draper, D. S. et al. 2003 *Phys. Earth Planet. Inter.* 139: 149-169. [16] Debaille, V. et al. 2007 *Nature* 450: 525-528. [17] Lee, D.-C. and Halliday, A. N. 1997 *Nature* 388: 854-857. [18] Foley, N. C. et al. 2005 *Geochimica et Cosmochimica Acta* 69: 4557-4571. [19] Kleine, T. et al. 2004 *Geochim. Cosmochim. Acta* 68: 2935-2946. [20] Caro, G. et al. 2008 *Nature* 452: 336-339. [21] Halliday, A. N. et al. 2001 *Space Sci. Rev.* 96: 197-230. [22] Borg, L. E. et al. 2003 *Geochimica et Cosmochimica Acta* 67: 3519-3536. [23] Treiman, A. H. 2005 *Chemie der Erde-Geochemistry* 65: 203-296. [24] Lapen, T. J. et al. 2010 *Science* 328: 347-351.

Effect of Initial Ti-abundance on Si-enrichment during Magmatic Evolution of Lunar Basalts: Initial Modeling Results. T. J. Fagan[1]* A. Suginohara[1] and D. Kashima[1], [1]Department of Earth Science, Waseda University, 1-6-1 Nishiwaseda, Shinjuku-ku, Tokyo, 169-8050, Japan. *fagan@waseda.jp.

Introduction:

Tholeiitic and calc-alkaline trends on Earth. Magmatic evolution of many terrestrial igneous systems can be characterized by the tholeiitic and calc-alkaline trends. In the tholeiitic trend, successive igneous liquids (and rocks) acquire higher values of Fe/(Fe+Mg), and enrichment in SiO_2 and alkalies occurs only during the latest stages of magmatic evolution (Fig. 1). The calc-alkaline trend is also characterized by increasing Fe/(Fe+Mg), but to smaller extents than the tholeiitic trend, and SiO2 and alkalies increase during early stages of magmatic evolution.

On Earth, one of the main controls on tholeiitic vs. calc-alkaline trends is oxygen fugacity. In systems with high $f(O_2)$, a high proportion of Fe occurs as Fe^{3+} and may crystallize in Si-poor minerals such as magnetite or high-Fe^{3+}-amphibole. This results in Si-enrichment of residual liquid, a main feature of the calc-alkaline trend [1]. In contrast, in low $f(O_2)$ systems on Earth, most Fe occurs as Fe^{2+} and crystallizes in silicates such as olivine and pyroxene. Values of Fe/(Fe+Mg) are low in early-formed crystals, but increase as early-formed crystals are removed from the system. This results in an increase over a wide range of Fe/(Fe+Mg), a main feature of the tholeiitic trend.

Fe/(Fe+Mg)- vs. SiO_2-enrichment on the Moon. An iron-enrichment similar to the tholeiitic trend has been inferred from a suite of igneous clasts in breccias of lunar meteorite Northwest Africa (NWA) 773 and paired meteorites [2-4]. A contrasting, SiO_2-enrichment trend has been inferred for Apollo sample 15405 [2,5]. Therefore, trends similar to the terrestrial tholeiitic and calc-alkaline trends may characterize some lunar igneous rocks; however, oxygen fugacities in magmatic systems on the Moon were much lower than those on Earth, and it is unlikely that significant quantities of Fe^{3+} were present on the Moon. Thus, controls on magmatic evolution on the Moon differed from those on Earth.

In this paper, we review the evidence for igneous trends in NWA 773 and Apollo 15405, and use MELTS [6] modeling to help evaluate controls on lunar magmatic evolution.

Analytical Methods:

Polished thin sections (PTS) of NWA 773 (1 PTS, on loan from M. Killgore, Univ. Arizona), NWA 2727 (1 PTS, Waseda University collection), and Apollo 15405 (3 PTS, on loan from Johnson Space Center, NASA) were examined by standard petrographic and electron microprobe (EPMA) techniques. Images and quantitative elemental analyses were collected using a JEOL JXA-8900 EPMA at Waseda University. Pyroxene analyses were collected by WDS at 15 kV, 10 to 20 nA and focused beam conditions. Pyroxene crystals in these samples often have fine-scale exsolution lamellae, so many analyses may be mixtures of high-Ca and low-Ca compositions.

Modeling of high vs. low Ti liquids was conducted using MELTS software [6]. We modeled fractional crystallization at low-pressure (P = 1 atm) and $f(O_2)$ at the Fe-FeO buffer. We recognize that lower $f(O_2)$ is more appropriate for the Moon [e.g., 7], but used buffered conditions for these initial results. We used compositions of Apollo samples 10024 [8] and 70215 [9] for high-Ti starting compositions and NWA 032 [10] and "NWA 773 parent" (a model composition [3]) for low-Ti compositions.

Results:

Our EPMA analyses of pyroxene confirm previous results [2,3,5]. Namely, NWA 773 and NWA 2727 pyroxenes exhibit a broad range of Fe/(Fe+Mg) (Fe#) ranging to extremely Fe-rich compositions (Figs. 2,3). Only clasts with extremely high Fe# coexist with igneous silica. Silica in symplectite occurs with pyroxene with lower Fe#, but this silica formed by pyroxferroite breakdown, not direct crystallization from liquid. In contrast, 15405 pyroxene has a narrow range and lower values of Fe# (Fig. 2). Silica is abundant in the 15405 clasts.

Using pyroxene Fe# as a proxy for Fe-enrichment, and using the presence or absence of free silica as a proxy for SiO_2-enrichment, NWA 773 group rocks represent a tholeiite-like trend, and the 15405 samples record silica-enrichment at much lower Fe#.

Our MELTS modeling shows that fractionation of Ti-oxides results in Si-enrichment in residual liquids for high-Ti liquids (Fig. 4). In contrast, low Ti-liquids maintain near-constant SiO_2 over long stages of model fractionation. However, differences in Ti alone are not sufficient to account for the differences between NWA 773 group and 15405. Silica-enrichment occurs during model fractionation of the high-Ti liquids, but free silica becomes stable only at very high Fe#. Some other process is required to account for the presence of free silica with moderate Fe# pyroxene in 15405.

References:

[1] Yagi K. and Takeshita H. (1987) in Magmatic Processes Mysen B.O., ed., p. 183-190. [2] Fagan T.J. et al. (2003) *MaPS 38,* 529-554. [3] Jolliff B.L. et al. (2003) *GCA 67, 4857-4879.* [4] Zeigler R.A. et al. (2007) *LPSC 38,* #2109. [5] Ryder G. (1976) *Earth Planet. Sci. Lett. 29,* 255-268. [6] Ghiorso M.S. and Sack R.O. (1995) Contrib. Mineral. Petrol. 119, 197-212. [7] Karner J. et al. (2004) Amer. Mineral. 89, 1101-1109. [8] Beaty D.W. and Albee A.L. (1978) Proc. Lunar Planet. Sci. 9th, p. 359-463. [9] Kesson S.E. (1975) Proc. Lunar Sci. Conf. 6th, p. 921-944. [10] Fagan T.J. et al. (2002) *MaPS 37*, 371-394.

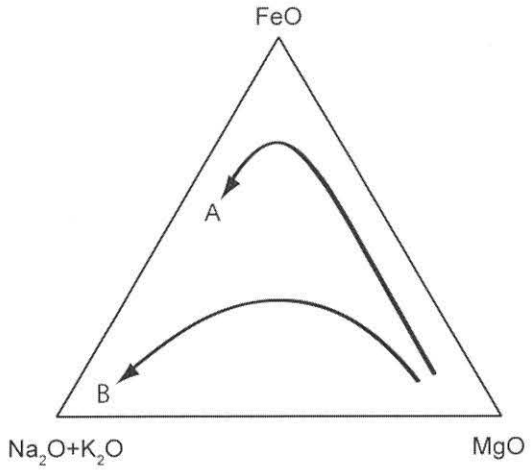

Fig. 1. Tholeiitic (A) vs. calc-alkaline (B) trends for terrestrial igneous rocks. MgO - FeO - Na_2O+K_2O represent whole-rock compositions (wt%). Because of the limited availability of lunar samples, a proxy for whole rock compositions is required to evaluate whether similar trends occurred on the Moon.

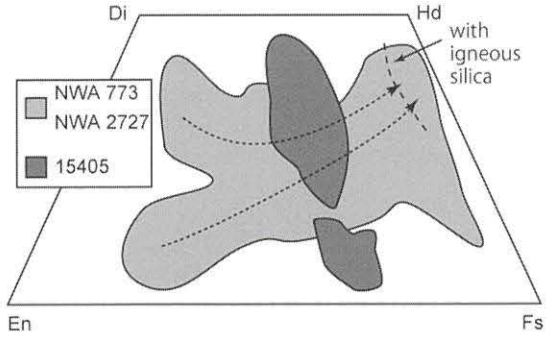

Fig. 2. Compositions of pyroxene in NWA 773 and 2727, and Apollo 15405. NWA 773 group pyroxenes have a range of compositions, interpreted as Fe-enrichment during crystallization. Igneous silica occurs only in clasts with Fe-rich pyroxene. Apollo 15405 pyroxenes have limited range in Fe/(Fe+Mg), so an igneous trend is not inferred directly; however, the 15405 pyroxenes coexist with silica, indicating SiO_2-rich composition at lower Fe# than NWA 773 group.

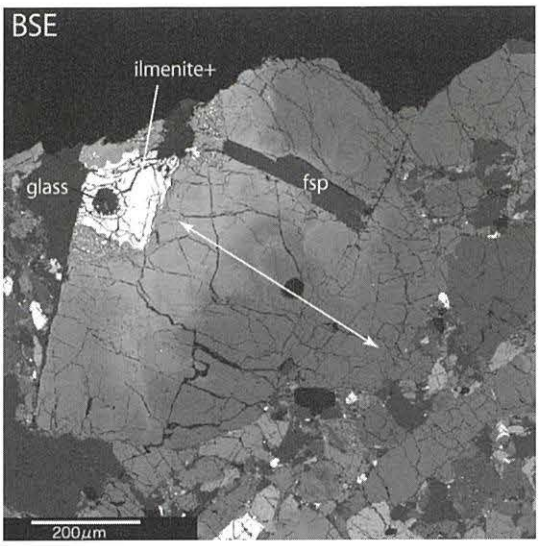

Fig. 3. Back-scattered electron (BSE) image of last from NWA 773 breccia. BSE grayscale shows zoning from Fe-poor (BSE-dark) to high Fe/(Fe+Mg) composition in pyroxene. Fe-rich minerals, including some ilmenite, occur with alkalic glass and some symplectite at the high Fe/(Fe+Mg) side of the clast.

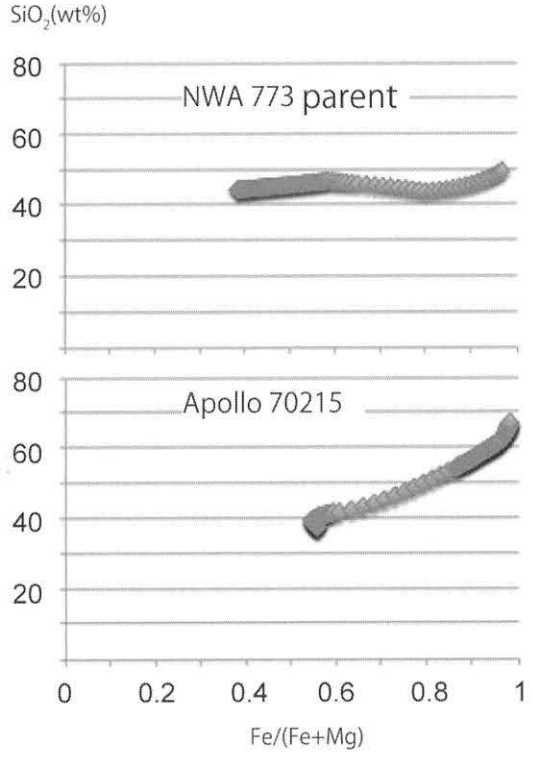

Fig. 4. Change in liquid SiO_2 vs. Fe# during model fractional crystallization of very low-Ti (NWA 773 parent, above) and high-Ti (Apollo 70215, below) starting compositions.

PROBABLE ROLE OF THE PERCHLORATE-METHANE-FORMALDEHYDE SYSTEM ON MARS AND ITS EFFECT IN THE BRINE SOLVING OF SURFACE ROCKS. E. Fodor. Eötvös University, Cosmic Materials Space Research Group. H-1117 Budapest, Pázmány P. s. 1/a. Hungary (fodorelem@freemail.hu).

Introduction:

The so far discovered components (methane, formaldehyde) of the atmosphere of planet Mars may be exposed to some form of oxidation by the interactions of the most recently discovered perchlorate ions (-ClO4). In this process methane (CH4) may undergo to spontaneous oxidation and some part of it forms formaldehyde, another part forms formic-acid. In the detailed process first formaldehyde forms, and later it is further oxidized to formic-acid (HCOOH) in the presence of large amounts of perchlorate ions. The formaldehyde sublimates into the Martian atmosphere, the formic-acid remains in the Martian soil.

The top soil on the Martian surface may absorb more formic-acid from the atmosphere provided that there are sufficient amounts of free hydrated sodium (Na+) and potassium (K+) ions. In this case the soil can also contain some amount of formic-acid in the form of dissociated format ions (-COOH). If the original pH value of the soil is 7.7, then by the effect of the format ions the pH of the soil will gradually decrease.

Results:

Over of the discovered hydrated mineral by the near past landed space probe Phoenix, from our point of view the most significant are the constituent is the sorosilicate Pumpellyite (Mg,Al)(OH)(H2O)X(SiO3). This signifies the boundary of finding water in some form, such are from the iron-alum (K,Fe(III))(SO4)2X12(H2O) and the usual alum (K,Al)(SO4)2X12(H2O). I surmise that there are some other crystallized minerals with less water than the two above cited ones, on the Martian surface within area. The potassium-iron and potassium-aluminum sulfate are very well soluble in water hence in aqueous alteration the cited silicates can be crucial sources of the potassium ion. The Martian atmosphere and watery chemical reactions the (-ClO4) ions presence favorable this type oxidation process.

In the first oxidation process water is forming which serves as solvent: Methane (CH4) + Perchlorate (-ClO4) = Formaldehyde (H2CO) + Chlorate (-OCl3) + Water (H2O). In the subsequent second reaction with the formed water Formaldehyde (H2CO) + Perchlorat (-ClO4) = Formic-acid (HCOOH) + Chlorate (-ClO3). If there is a large enough concentration of (K+) and (Na+) ions in the soil, then the format ion (-COOH) through hydration by water can partly be retained by the soil, and the rest - non hydrated - formaldehyde molecules may evaporate into the Martian atmosphere. In addition to the above described joined hydration process the Martian soil may contain much larger quantity of water originating from some other (unknown) processes. The liquid phase of the perchlorates and chlorates can also be maintained by the presence of the sufficient alkali ion constituents, in spite of the extreme cold climate at a condition of low atmospheric pressure of P=6X10 at -3 Bar.

Also the freezing point of this partly liquid mixture is lowered by the RAULT-LAW: [dT=ConstansXM(b), where M(b) is Molality (mol/gram)], and therefore a fluid chemical environment may be resulted. On our planet Earth Pumpellyite (Mg,Al)(OH)(H2O)X(SiO3) can be found for example in metagabbros (its vicinity often contains the violet and magenta colored (KFe(III))(SO4)2X12(H2O), too), and this mineral can be the largest source of the (K+) ion on Mars. The metamorphous processes of the Pumpellyites in watery medium can undergo further ionotation processes.

Conclusions:

Because of the overall a different Lambertian albedo between the wet and dry patches of the Martian surface a LASER or LIDAR Optical reflection can find these aqueous alteration sites in the Martian soil. The Pumpellyite undergo further chemical transformation with the alkaline ions and (Fe(II)), (Fe(III)) ions.

References:

[1] M.H.Hect, S.P.Kounaves, R.C.Quinn, S.J.West, S.M.M.Young, D.W.Ming,D.C.Catling,

B.C.Clark, W.V.Boyton, J.Hoffman, I.P.DeFlores, K.Gospodinova, J.Kapit, P.H.Smith (2009): Detection of Perchlorate and the Soluble Chemistry of Martian Soil at the Phoenix Lander Site. *Science* 3 July 2009, Vol. 325. no. 5936, pp. 64 – 67 :

[2] Trent Schindler, Michael Mumma, Paul Mahaffy, Scott Edgington, Eric Wilson, (2009): *Workshop on Methane on Mars* ,25-27.11.2009.ESRIN, Frascati,Italy: Methane Plume During the Northern Summer Season by the Mars Express, Methane Abundance as a Function of Longitude by the Mars Express/PFS,NASA Goddard Space Flight Center and NASA Planetary Atmospheres Program and from Jet Propulsion Laboratory/Mars Express Program Office.Pasadena ,CA 91109 ,USA.

[3] Maguire,W.S.,(1977): Martian isotopic ratios und upper limits for possible minor constituents as derived from Mariner 9 Infrared Spectrometer Data, *Icarus* 32,pp. 85-97.Article,PDF.

[4] Malin and Edgett, (2000): Hot Spots on the Mars. *Workshop on Methane on Mars*, ESRIN, Frascasti,Italy.

[5] A.S.Wong, S.K.Atreya, V.Formizano, Th.Encrenaz, N.I.Ignatiev, (2004): Atmospheric Photochemistry above possible Martian Hot Spots,and Planetary Fourier Spectrometer on Mars Express. *Advances in Space Research*, Volume 33, Issue 12, 2004, Pages 2236-2239,

Shock wave vs CVD origin of meteoritic nanodiamonds: An astromineralogical overview.

A. Gucsik[1,2], Sz. Bérczi[3] and Sz. Nagy[4] [1]Abteilung Geochemie, Max Planck Institut für Chemie, Joh-J.-Becherweg 27, Universitätscampus, Mainz, D-55128, Germany; [2]Savaria University Center, University of West Hungary, Károlyi Gáspár tér 4., H-9700, Szombathely, Hungary; [3]Eötvös Lóránd University of Budapest, Pázmány Péter sétány 1/c, H-1117 Budapest, Hungary;

Primitive meteorites contain abundant (up to 1500 ppm) amounts of nanodiamonds. At least some subpopulation must be of pre-solar (stardust?) origin, as indicated by the isotopic composition of trace elements the diamonds carry, in particular noble gases [1] and tellurium [2]. On the other hand, the isotopic composition of the major element, carbon, is unremarkable, i.e. within the range reasonably expected for Solar System materials [3]. As a consequence many workers believe that the majority of the diamonds is of local, i.e. Solar System, origin and that the fraction that is pre-solar is relatively small [4].

Two main theories exist for the formation process of the meteoritic nanodiamonds (e.g., [5]-and references therein): (1) Chemical Vapour Deposition (CVD), and (2) shock origin. TEM investigations, in particular, seem to suggest that formation by a CVD process is most likely [5].

It is well known (based on shock recovery experiments) that the required shock pressure to produce impact-induced diamonds is around 40 GPa [6]. According to Klein et al. [7] interstellar shock waves can be produced by the powerful stellar winds of massive stars, supernova explosions, cloud-cloud collisions, and spiral density waves. In the following paragraph we focus on the interaction of supernova-driven shock waves and interstellar cloud and their relationship to the linear growth rate of nanodiamonds.

Assuming a supernova shock wave front is responsible for the synthesis of diamond, its formation can be considered as a two step process. According to supernova shock wave experiment of Hansen et al. [8] the first step is the transition of the secondary shock wave through interstellar media near the supernova explosion resulting in grain-grain collisions. The initial shock wave occurs rapidly, which can give the physical conditions such as high pressure and high temperature adequately for the formation of diamond creation during the second or crystallization stage. A disadvantage of this process, however, is that, pressures obtained during such collisions are often so high that shattering, sputtering and vaporization become dominant over phase transformation [9-11], which limits the effectivity of diamond formation. In this stage, according to the linear growth rate of diamond (RD), the following relation between the linear size L of the growing diamond, the linear growth rate RD and growth time (time of crystallization) is given by

$$L(nm)=RD(nm/s)t(s) \quad (1)$$

For CVD diamonds, the RD rate of CVD ranges between 0.03 and 1.2-1.7 nm/s. Accordingly, for the meteoritic nanodiamonds with a mean size L of 2.6 nanometers the time of crystallization (t) would be between 1-2 s for relatively fast growth and on the order of 100 s for slow growth. The structural property (i.e., startwin structure) of meteoritic nanodiamonds favours rapid growth, i.e. seconds. In the case of the high pressure high temperature (HPHT) processes growth rates are high, in the order of 300-500 nm/s. This would result in growth times of 0.005-0.01 s (i.e., 5-10 ms), much shorter than for CVD processes [12-17]. The transition may have occurred on a much shorter timescale. Assuming, for example, a shock wave travelling at 20 km/sec., a rather low value [9], the transition through the grain would last 2.6 nm/20 km/sec (=0.13 picoseconds). It is also poorly understood whether or not nanodiamonds would be formed such very short period in the Universe. Of course, more detailed experimental work must be done focusing on the relationship between relatively rapid growth rate and speed of the shock wave front.

Consequently, according to Ott [18-and references therein] an origin by a CVD process seems most likely but is not confirmed up to date. The nanodiamonds contain noble gases with exotic isotopic composition that tie them to element synthesis in supernovae and that were probably introduced by ion implantation. Because of their small size it is not possible to perform chemical/isotopic analysis of single grains, which is in contrast to the case of the other identified presolar grains.

Acknowldgement-Authors are grateful for Drs Ott (Max Planck Institute for Chemistry, Mainz, Germany), Dr Karczemska and Dr Szurgot (Technical University of Lodz, Lodz, Poland) giving their useful comments on this contribution.

References

[1] Huss G. R. and Lewis R.S. (1994) *Meteoritics* 29, 791-810. [2] Richter S. et al. (1998) *Nature* 391, 261. [3] Russel S.S. (1991) *Science* 254, 1188-1191. [4] Zinner E. (1998) *Ann. Rev. Earth Planet. Sci* 26, 147-188. [5] Daulton T.L. (1996) *Geochim. Cosmochim. Acta*, 60, 4853. [6] Kenkmann T. et al.

LPSC XXXIII, #1052. [7] Klein R.I. et al. (1994) *Astrophys. J.,* 420, 213. [8] Hansen J.F. (2007) *Astrophys. J.* 662, 379. [9] Tielens A.G.G.M. (1987) *Astrophys. J.* 319, L109. [10] Jones A.P. (1996) *Astrophys. J.* 469, 740. [11] Jones A.P. (1994) *Astrophys. J.* 433, 797. [12] Battaile C.C. (1997) *J. Electron. Mat.,* 26, 960-965. [13] Chung H-K. and Sung J. C. (2001) *Diamond and Related Materials* 10, 1584. [14] Ignatenko P.I. and Sel'skaya I.V. (2002) *Phys. Semiconductors and Dielectrics* 45, 2, 180. [15] Abbashian R. et al. (2005) *Diamond and Related Materials* 14, 1916. [16] Mokuno Y. (2006) *Diamond and Related Materials*, 15, 455. [17] Karczemska, A. et al. (2008) *Diamond and Related Materials* 17, 1179.

Application of the differentiation modell of Takahashi for a chondritic asteroidal body in our studies comparing H and EH3-chondrites

I. Gyollai[1], Sz. Bérczi[1], Sz. Nagy[1], S. Józsa[2], Gy. Szakmány[2], A. Gucsik[3]
[1]Eötvös University, Cosmic Materials Space Research Group, Budapest, Hungary
[2]Eötvös University, Dept. Petrology and Geochemistry, Budapest, Hungary
[3]Max Planck Institute for Chemistry, Mainz, Germany,

Introduction, literature background

The first overview of petrographical studies of NIPR Collection have been made by Yanai and Kojima (1). Later studies (2) emphasized chemical, mineralogical and petrological changes in different (C, H, L, LL) chondritic series during thermal metamorphism.

Takahashi (3) carried out melting investigations on the Y-74191 chondrite between 6 and 30 kbar pressure range. As a result, Takahashi's model is the following: during the heating process L3 chondrite shows partial melting and firstly segregating the metallic melt later the silicate component. Segregation of the metal and sulfide component occured at first around the chondrules, as far as heat is increasing it results a pallasite-like texture.

This differenciation process has been studied in our another NIPR abstract (4).

Samples and Methods

Optical microscopy: The mineral assemblages and textures of our samples were characterized with a Nikon Eclipse LV100POL optical microscope using plane polarized and reflected light modes (at Eötvös Lorand University of Budapest, Hungary and at University of Vienna, Austria). ALH-769 75-5, 98-1 and Y-790957 (L5) 90-1 sample were prepared with 35 μm, the Y-74191 58-2, 92-2, and Y-74355 81-3, 84-7 , Y-790957 72-2 were prepared below than 30 μm in thickness.

Results

H-series

Yamato 791428 -H3 chondrite: In spite of EH3 sample, the components (chondrules, crystal-fragments) are dominant in the matrix. The matrix consist of iron-oxid, but it appears as metal patches among some chondrules which can result pallasit-like texture. Porphyritic and glassy texture are dominant in larger chondrules, but glassy and radial texture are dominant in microchondrules.

Allan Hills 77233. - H4 chondrite: This sample contains more crystal fragments in the matrix, and metal melt occurs at more places between the chondrules, as we observed in H3 sample. The troilite and iron melt have been oxidized to hematite because of terrestrial weathering. The size of the chondrules is larger and the granular and porphyritic texture is dominant in the chondrules.

Yamato 74079. - H5 chondrite: Crystal fragments are dominant in the sample. It shows less number of larger chondrules, which have glassy and porphyritic textures. The metal melt occurs such as big patches between the chondrules. The chondrule-forming minerals contains abundant fractures.

Yamato 74014. - H6 chondrite: This sample consist of chondrules and chrystal fragments furthermore recrystallized matrix. This exists less metal melt between the chondrules as can be observed in H5, and most of that has been oxidized because of iron-oxid minerals. The opaque patches area is troilite. The chondrule fragments have barred and porphiritic texture.

Yamato 691. - EH3 chondrite: This sample has high abundance of microchondrules and fractures. The fine-grained groundmass is dominant in the sample. The olivine shows weak mosaicism, the piroxenes exists mechanical twins inside the chondrules. The mineral fragments in the matrix have been fractured and show weak mosaicism. The most of the chondrules have granular and poicilitic texture, but the radial and glassy texture are dominant inside the microchondrules. The photos which were taken in reflected light shows such matrix which consist of fine-grained silicates, glass and iron-oxid, but the chondrules exhibit troilite rim, pyrrhotine and Fe-Ni metal The matrix contains splashes of troilite and nickel-iron phase. Some chondrules consist of metal and troilite and have well-developed rim of opaque minerals like the silicate chondrules.

Summary:

During the thermal evolution of H-planetary body, there is an important process not only the alteration of chondrules and matrix, but the differentiation of metal melt from silicates too. In H3 state the metal melt occurs as several larger patches among chondrules, but during the thermal evolution the metal melt occurs between more chondrules and in fractures of minerals. The oxidation rate of metal melt can be observed through increasing thermal metamorphism.

This metal melt consist of Fe-Ni and troilite.

The EH3-chondrite contains more metal melt than H-chondrites, and whole matrix consist of iron oxides. Several chondrules contains pyrrhotine and troilite.

Acknowledgments: We are grateful to the NIPR Antarctic Meteorite Research Center, Tokyo (to Prof. Kojima), for the loan of the Antarctic set and to LRG (Eötvös University) and University of Vienna (to Professor Lein) for assistance with the analytical instruments. We are grateful to Professor Csaba Szabó and Professor C. Koeberl for advices in petrography.

References

(1)Yanai K., Kojima H. (*1987*): Photographic Catalog of the *Antarctic. Meteorites*. NIPR.

(2)Bérczi Sz., S. Józsa, Zs. I. Kovács, B. Lukács, Gy. Szakmány (2004): Acta Mineralogica et Petrographica, Szeged, XLV/2. 55-60.

(3) Takahashi, E.: – NIPR Symposium, 1983. *Institute of Polar Research,* 19930500, 6, 391-400

(4)Gyollai I. et al (2009): Application of the differentiation modell of Takahashi for a chondritic asteroidal body in our studies comparing Mezőmadaras, Yamato-74191 and Yamato-84151 meteorites.–NIPR Antarctic Meteorite Symposium

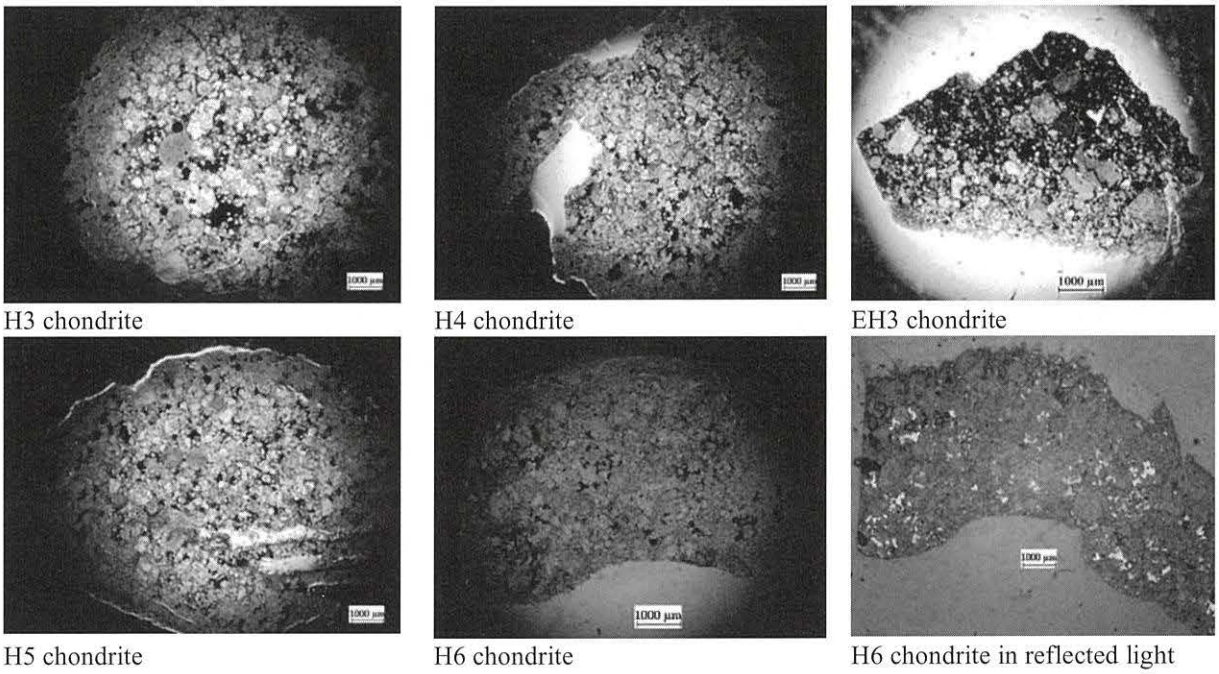

H3 chondrite | H4 chondrite | EH3 chondrite

H5 chondrite | H6 chondrite | H6 chondrite in reflected light

Fig. 1. : Differentiation of metal melt in H-chondrites. The EH3 chondrite of consist much more metal melt than H-chondrites.

New studies of thermal and shock metamorphism on the NIPR Antarctic L-chondrite series: Y-74191 (L3), Y-74355 (L4), Y-790957 (L5), and ALH-769 (L6) samples.

I. Gyollai[1], Sz. Bérczi[1], Sz. Nagy[1], S. Józsa[2], Gy. Szakmány[2], A. Gucsik[3]
[1]Eötvös University, Cosmic Materials Space Research Group, Budapest, Hungary
[2]Eötvös University, Dept. Petrology and Geochemistry, Budapest, Hungary
[3]Max Planck Institute for Chemistry, Mainz, Germany,

Introduction, literature background

The first overview of petrographical studies of NIPR Collection have been made by Yanai and Kojima (1). Later studies (2) emphasized chemical, mineralogical and petrological changes in different (C, H, L, LL) chondritic series during thermal metamorphism.

There were important earlier studies on samples of our series on ALH-769 and Y-74191. Funaki et al (3,4) concluded the ALH-769 is being transitional between the L5 and L6 thermal metamorphism stages.

According to NIPR Database, the frequency of oxides from SiO2 to MgO and Cr2O3 show decreasing trend in bulk composition during thermal metamorphism. The quantity of Fe, and Ni show increasing trend in bulk composition up to L5 thermal metamorphism stage, but from L5 to L6 is clearly decreasing it.

Methodology

Optical microscopy: The mineral assemblages and textures of our samples were characterized with a Nikon Eclipse LV100POL optical microscope using plane polarized and reflected light modes (at Eötvös Lóránd University of Budapest, Hungary and at University of Vienna, Austria). ALH-769 75-5, 98-1 and Y-790957 (L5) 90-1 sample were prepared with 35 μm, the Y-74191 58-2, 92-2, and Y-74355 81-3, 84-7 , Y-790957 72-2 were prepared less than 30 μm in thickness.

Results

Yamato-74191 (L3) chondrite: According to Sugiura (1999) (meg kéne hivatkozni!!), the Y-74191 chondrite had been classified to L 3,7 on the base of thermal metamorphism, it was below 200 °C. The sample has a fine-grained groundmass and chondrules have sharp rims. The inhomogeneity in pyroxenes of the measured sample could be well observed. The thin section consists of 45% olivine and 55% pyroxene phenocrysts. Some chondrules are bordering on opaque phases, which can be observed in both thin sections of this sample. The chondrules have generally about 0,8 mm diameter, but larger chondrules with diameter between 1 and 1,5 mm, and smaller ones with diameter between 0,1-0,3 mm can also be observed. Several chondrules have glassy, brecciated and granular texture and there are a lot of mineral fragments in the groundmass. The pyroxenes are hypidiomorphic and show pillar shape and mechanical twins in the granular chondrules. The porphyritic chondrules consist of olivines and exhibit smaller size and isometric shape. The barred chondrules are build up from needle-shaped pyroxene and olivine phenocrysts. In a small (0,5 mm) chondrule, mixed texture can be observed with barred and excentroradial texture together. This phenomenon may be in consequence of different cooling rate for two glued (attached) parts. The Y-74191 (58-2) sample has 4 poikilitic chondrules, but those do not occur in the measured sample. In both of thin sections have devitrified glassy chondrules with crystal needles. Because of the strong brecciation, of the sample and presence of mechanical twins in pyroxens the Y-74191 can be classified into the S3 shock stage on the Stöffler scale.

Yamato-74355 (L4) chondrite: The Yamato-74355 consists of well formed round-shape chondrules (60 %), chondrule fragments (10 %) and fine-grained groundmass (20 %) with olivine and pyroxene phenocrysts (10 %) of about 0,03 and 0,12 mm diameter in range. (The high amount of phenocrysts are 55% olivine and 45% pyroxene.) The chondrules have 0,1-2 mm in diameter. The biggest chondrule has radial texture (with more centres) and elongated shape (its length is 1,5 mm and width is 0,7 mm). The porphyritic chondrules are standing of different zones of olivine as shown their interference color: yellow is the rim and blue is the core. A mixed chondrule also occurs in this sample and having barred texture in inner part and granular texture in the external part. There are opaque patches which consist of troilite and metallic iron and it have in range of diameter between minimum 0,4-0,7 mm and maximum 2-3 mm. Inside of some chondrules iron oxid pigments occur on the surface of minerals which manifest itself in higher (reddish purple to orange) interference color on pyroxenes. The observed porphyritic chondrules can be divided into two groups:

1. Microporphyritic chondrules are build up from phenocrysts about between 0,02-0,05 mm in average size, where the olivines are smaller than pyroxenes.
2. Chondrules with lath-shaped, randomly oriented pyroxenes. Such chondrules are 0,5-0,8 mm in size and their texture is dominated by needle-shaped crystals which are arranged individually and randomly embedded in the groundmass.

Yamato-790957 (L5) chondrite: The Y-790957 is a strongly brecciated chondrite occuring a small number of chondrules but large number of mineral fragments which have average 0,03-0,1 mm in size. The whole sample has porphyritic texture. There

are recrystallized, the radial chondrules have elongated shape and smooth rim. The biggest chondrule is 2 mm length and 0,8 mm width in size and there is an included inclusions as a fragment as well. Some chondrules have poikilitic and granular texture, where the pyroxenes have pillar shape and mechanical twins. The mineral assemblages contain opaque veins. In the Y-790957 84-7 sample, the olivines show weak mosaicism and contain planar fractures (PFs), near the opaque mineral assemblages. All these characteristics infer the S4 shock stage of this sample on the Stöffler scale.

Allan Hills-769 (L6) chondrite: The sample consists of chondrules, crystals, chondrule fragments and recrystallized groundmass. There are more chondrules and their have much better preserved texture than in Mócs (L6) sample. (The number of chondrules is also larger than in Mócs sample.) That's it whereat ALH-769 can be classified to the boundary of the L5 and L6 groups. This classification is in accordance with Funaki's similar conclusion on the base of their NMR measurements.

The biggest chondrule is 3 mm in size and it has barred texture. In the texture the zoned, fractured olivines have lath-shape and they are overgrown by iron-rich pyroxene needles, which were crystallized from the groundmass. The largest radial chondrule is a fragment, its size is approximately 1,2 mm.

There are other chondrules which has 0,6 mm in average diameter. Their grain size is similar to that of the recrystallized matrix of the chondrite. The texture of these chondrules is microgranular and build up from isometric olivine grains.

There are some poikilitic chondrules which have sinusoidal rim. The matrix is heterogeneous and shows fine-grained recrystallized material and relict, additionally fractured olivines with tabular shape. The hematite pigments occur on 3-4 mm2 area resulting in higher interference colors in pyroxenes. Some PFs occur in opaque-inclusion-bearing minerals in the Allan-Hills-769 (75-2) sample. Near to the patchy-like opaque minerals, mosaicism can be observed in olivine. But there are no shock metamorphic feature in ALH-769 (98-1) sample. Following to Stöffler scale (1991) the Allan-Hills-769 (75-2) can be classified into S3-S4 shock level.

Summary: In this work two processes have been studied on L-series chondrites: the thermal and shock metamorphism. The mineralogical and petrological developments during thermal metamorphism have been observed in two thin section of each L-series samples. The Y-74191 L3 sample contains chondrules and shows sharp rims, opaque mineral rims and heterogeneous mineral phases common in pyroxenes. During the thermal metamorphism, the number of chondrule fragments is increasing in expense of rounded chondrules, and the number of large phenocrysts increases in expense of fine grained material. During the thermal metamorphism the smaller chondrules disappear, only the larger ones (about 1,5-3 mm in size) have been preserved even at the L6 thermal metamorphic stage. The fractures in minerals and opaque grains were observed at higher thermal metamorphic stages (L5-L6).

The shock metamorphism appears in samples only in some localities at higher thermal metamorphic stage (L5-L6) samples. Most of shock features can be seen near to the opaque mineral assemblages. This phenomenon can be due to the reflecting shock waves on opaque minerals. Reflection multiplies the power of the shock waves and it results higher shock effects in minerals with lower acoustic impedance.

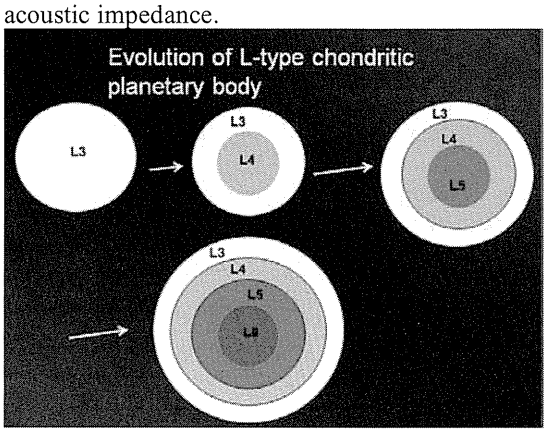

Acknowledgments: We are grateful to the NIPR Antarctic Meteorite Research Center, Tokyo (to Prof. Kojima), for the loan of the Antarctic set and to LRG (Eötvös University) and University of Vienna (to Professor Lein) for assistance with the analytical instruments. We are grateful to Professor Csaba Szabó and Professor C. Koeberl for advices in petrography.

References

(2)Bérczi Sz., S. Józsa, Zs. I. Kovács, B. Lukács, Gy. Szakmány (2004): Acta Mineralogica et Petrographica, Szeged, XLV/2. 55-60.

(3)Funaki, M.; Nagata, T. & Momose, K.-i. (1981): *Memoirs of National Institute of Polar Research. Special issue, National Institute of Polar Research,* 19811200, 20, 300-315

(4) Funaki, M. (1993) *Proceedings of the NIPR Symposium on Antarctic Meteorites, National Institute of Polar Research,* 19930500, 6, 391-400

(1)Yanai K., Kojima H. (*1987*): Photographic Catalog of the *Antarctic. Meteorites*. NIPR.

NIPR Database

Chemical compositions of lunar meteorite Dhofar 1428.

Y. Hidaka[1], A. Yamaguchi[2], M. Ebihara[1], [1]Department of chemistry, Tokyo Metropolitan University, Tokyo 192-0397, Japan, [2]National Institute of Polar Research, Tachikawa, Tokyo 190-8518, Japan.

Introduction:

Dhofar 1428 is a 213-gram lunar meteorite found in Oman in 2006 [1]. It was classified as a regolith breccia [2]. We previously showed that major element composition of this meteorite is similar to those of FANs, but has slightly high K content [3]. Here, we report additional chemical compositions of Dhofar 1428 for trace elements, rare earth elements (REEs), Th, U and platinum group elements (PGEs; Ru, Rh, Pd, Os, Ir, Pt), and discuss the chemical characteristics of Dhofar 1428 lunar meteorite.

Sample and methods:

We analyzed two fragments of Dhofar 1428, which were named Dhofar 1428,11 (363 mg) and Dhofar 1428a (155 mg). Bulk chemical compositions of these two fragments were determined by prompt gamma-ray analysis (PGA) and instrumental neutron activation analysis (INAA). Both irradiation were done at Japan atomic energy agency (JAEA). For trace elements analyses, we used the sample Dhofar 1428a for REE measurement and Dhofar 1428,11 for PGE measurement, respectively. REE and PGE compositions were determined by using an inductively coupled plasma mass spectrometry (ICP-MS) VG elemental plasma quad 3 at Tokyo Metropolitan University.

Results and Discussion:

Bulk chemical compositions of Dhofar 1428 were determined by PGA and INAA. Quantitative values of two fragments are quite consistent for major, minor and trace elements which include incompatible elements such as REEs and some siderophile elements. This indicates that Dhofar 1428 has homogeneous in chemical composition. Major and minor element compositions are almost within the range of feldspathic lunar meteorites. Bulk molar Na/(Na + Ca) ratio and bulk Mg' value (66) are also within the range of ferroan anorthosite (FAN). It clearly indicates that Dhofar 1428 is mostly composed of FAN materials, but Sr and Ba concentrations are high comparing to Antarctic lunar meteorites. Because these elements are sensitive to terrestrial contaminations, there is a possibility that these elements are somewhat affected by terrestrial contaminants. Potassium concentration of Dhofar 1428 is slightly high among feldspathic lunar meteorites, possibly due to the existence of a KREEPy clast which contains Ca-phosphates and K-feldspars and K-rich feldspars which are observed in a polished thin section made from an adjacent chip for chemical analysis of Dhofar 1428 [3].

REEs and PGEs were determined by ICP-MS. The REE abundances of Dhofar 1428 are ~ CI x 10 and slightly depleted in HREEs and have slightly small Eu-anomaly (Sm/Eu ratio = 1.54) (Fig. 1). These values are consistent with our INAA data. The REE abundances of Dhofar 1428 are quite consistent within the range of feldspathic regolith breccias, being consistent with the major element data and petrological observation [2, 3]. The REE abundances of Dhofar 1428 are slightly higher than those of FANs [3], which consistent with the higher abundance of K in this meteorite.

Based on these observations and chemical data, the REE abundances of Dhofar 1428 can be explained by a mixture of ~98 wt%-FAN plus ~2 wt%-KREEP, using the values of FAN ([4]; 60025) and KREEP ([5]; SaU 169 KREEP clast).

The PGE abundances of Dhofar 1428 are ~ CI x 0.01 and are not fractionated (Fig. 2). It is distinct from those of pristine highland rocks which have very low (< CI x 10^{-4}) concentrations and fractionated pattern of PGEs [7]. It is certain that Dhofar 1428 is contaminated by any PGE-rich impactors. These impactors can be assumed to be chondritic materials, because of the flat PGE pattern of Dhofar 1428.

The plots of Pt/Pd vs. Pt/Rh and Pd/Ir vs. Rh/Ir show that composition of contaminants is similar to those of carbonaceous chondrites, CM and CK, among chondritic materials (Fig. 3). This is consistent with the fact that CM-like materials are main source of the elevated siderophile abundances in Apollo mature soils [10].

Based on major and trace element compositions, we conclude that Dhofar 1428 is mostly composed of FAN materials, ~2 wt%-KREEP materials and ~1 wt%-CM chondritic materials.

References:

[1] Bunch T. E. et al. (2006) *Meteorit. Planet. Sci., 41,* A31. [2] Zhang A. C. et al., (2009) *Meteorit. Planet. Sci., 44,* A226. [3] Hidaka Y. et al. (2009) *Meteorit. Planet. Sci., 44,* A91. [4] Nakamura N. et al. (1973) *Proc. 6th Lunar Sci. Conf.,* 1445-1465. [5] Gnos E. et al. (2004) *Science, 305*, 657-660. [6] Anders E. and Grevesse N. (1989) *GCA, 53*, 197-214. [7] Day J. M. D. et al. (2010) *Earth and Planetary Sci. Lett., 289*, 595-605. [8] Tagle R. and Berlin J. (2008) *Meteorit. Planet. Sci., 43,* 541-559.
[9 Fischer-Gödde M. et al. (2010) *GCA, 74*, 356-379.
[10] Wasson J. T. et al. (1975) *The Moon, 13*, 121-141.

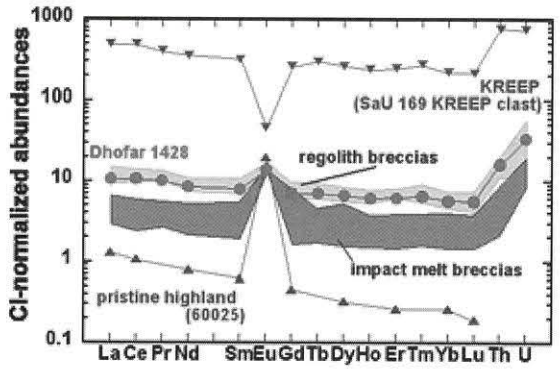

Fig. 1 CI-normalized REE abundances. Impact melt breccias and regolith breccias are among feldsphathic lunar meteorites. Data of pristine highland and KREEP are from [4] and [5], respectively. CI values are from [6].

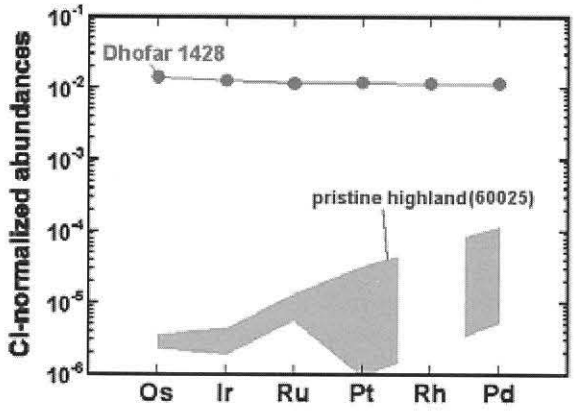

Fig. 2 CI-normalized PGE abundances. CI values are from [6], pristine highland values are from [7].

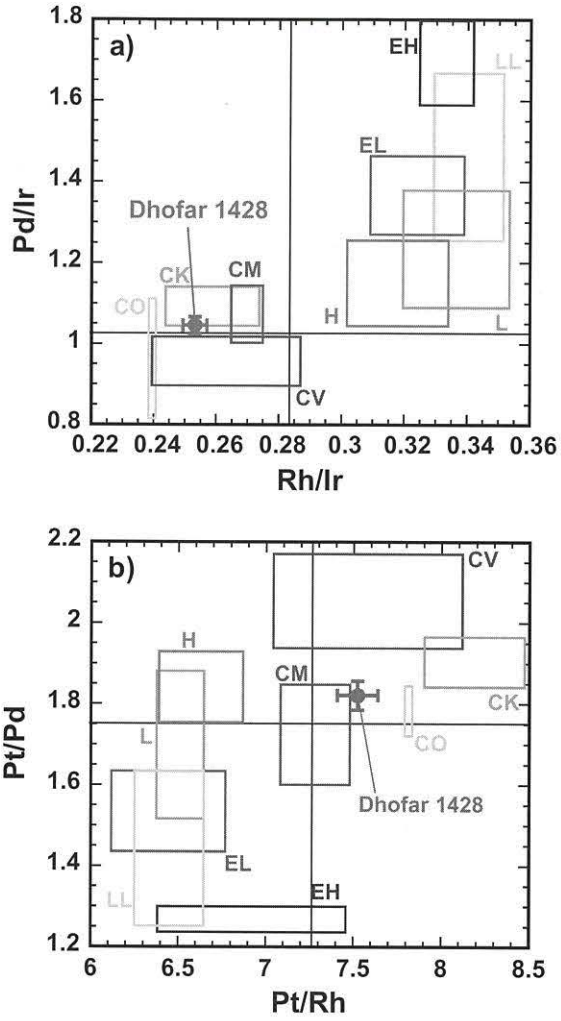

Fig. 3 PGE ratios of Dhofar 1428 and chondrites (a) for Pd/Ir vs. Rh/Ir and b) for Pt/Pd vs. Pt/Rh) Chondrites values are from [8] and [9].

What to Expect of Samples of Asteroid Itokawa Returned by Hayabusa Spacecraft. T. Hiroi, Department of Geological Sciences, Brown University, Providence, RI 02912, USA.

Introduction:

Hayabusa spacecraft landed on the asteroid 25143 Itokawa in 2005 and is coming back to Earth this month to drop its sample capsule. In this paper, the surface properties of Itokawa are reviewed based on observations by Hayabusa during its rendezvous with the asteroid, based on which considered are possible findings expected of the Itokawa samples if the recovery is successful.

Discoveries of Hayabusa's Rendezvous with Itokawa:

Visible and near-infrared (VNIR) reflectance spectra of asteroid Itokawa are all consistent with those of LL5 or LL6 chondrites based on its observations by both ground-based telescopes [1] and the Near-Infrared Spectrometer (NIRS) onboard Hayabusa [2] except for reddening and darkening due to space weathering [3]. Because the VNIR spectra are determined mainly by the olivine and pyroxene compositions and modal abundances, Itokawa's surface major silicate composition is consistent with those of LL5-6 chondrites from the km scale (ground-based telescopic observations) down to the cm scale (NIRS close-up observations) [4]. Data by the x-ray spectrometer (XRS) onboard Hayabusa also show an elemental composition consistent with L and LL chondrites [5].

Global color mapping using data by the Asteroid Multiband Imaging Camera (AMICA) onboard Hayabusa shows a high correlation between the redness, darkness, and the degree of space weathering [6], suggesting compositional uniformity except for a "black boulder" having an extremely low albedo found on the head side of Itokawa [7]. A photometric analysis of the NIRS data indicated a uniform composition of surface of Itokawa, and produced a map of particle size and degree of space weathering [8], which was the first of its kind.

All these evidences point to an idea that Itokawa's surface consists of an LL5-6 chondrite like material with uniform composition down to the cm scale, wherein no pyroxene-olivine or metal-silicate separation exists at larger than the cm scale. This describes almost exactly the equilibrated LL chondrites in our meteorite collections.

Close-up images of MUSES-C regio taken by AMICA show brighter and darker cm-size coarse regolith particles (pebbles) [9]. Combined with the above result, MUSES-C where sampling attempts were made is a mixture of materials of different degrees of space weathering or shock darkening.

Possible Properties of Itokawa Samples:

Most likely outcome of sampling attempt on the surface of Itokawa would yield mineral fragments of LL5-6 composition (olivine Fa 26-32, pyroxene Fs 22-27), some of which are space weathered or shock darkened. Space weathering could be easily detected by the presence of nanophase metallic iron ($npFe^0$) particles on the surface of mineral grains, coupled with solar wind implantation. Shock darkening can be due to either $npFe^0$ or other opaque particles distributed over the entire mineral volume just like seen with olivine in some of Martian meteorites [10]. Many fragments of metallic iron are expected, and also possibly expected is a small portion of the "black boulder", which could be a shock-darkened LL chondrite material.

Implications of the Oxygen Isotopic Trend of Itokawa Samples:

Assuming that the returned sample contains mineral fragments or complete stones of LL5-6 petrology, what do we expect of the isotopic composition, especially the oxygen isotope trend? Listed below are some thoughts:

If the oxygen isotopic trends of Itokawa sample and the LL chondrites are consistent,

(a) Itokawa came from one of many LL chondrite parent bodies;

(b) Itokawa came from the LL chondrite parent body, which is just one asteroid, from which all LL chondrites come; or

(c) Itokawa is the LL chondrite parent body, and we live in a very special era of the solar system history when Itokawa exists.

If their oxygen isotopic trends do not match,

(d) There are many mineralogically LL chondrite like asteroids, but there is only one parent body of the LL chondrites in our collections, and Itokawa came from a different asteroid.

Among the above cases, (a) and (d) would lead to the idea that LL chondrites and ordinary chondrites in general are indeed very abundant in the solar system, while (b) and (c) would not guarantee such a claim. However, it is hard to tell which of (a), (b), and (c) is true. Case (d) would demand a significant modification to our idea of utilizing the oxygen isotopic trends to identify the meteorite parent bodies.

References:

[1] Binzel R. P. et al. (2001) *Meteorit. Planet. Sci., 36*, 1167-1172. [2] Abe M. et al. (2006) *Science, 312*, 1334-1338. [3] Hiroi T. et al. (2006) *Nature, 443*, 56-58. [4] Hiroi T. et al. (2007) *LPS XXXVIII*, Abstract #1048. [5] Okada T. et al. (2006) *Science, 312*, 1338-1341. [6] Ishiguro M. et al. (2007) *Meteorit. Planet. Sci., 42*, 1791-1800. [7] Saito J. et al. (2006) *Science, 312*, 1341-1343. [8] Kitazato K. et al. (2008) *Icarus, 194*, 137-145. [9] Yano H. et al. (2006) *Science, 312*, 1350-1353. [10] Pieters C. M. et al. (2008) *J. Geophys. Res., 113*, E06004.

Mineralogy of Opaque Phases in Almahata Sitta Ureilite. R. Hochleitner[1], V.H. Hoffmann[2,3], M. Kaliwoda[1], T. Mikouchi[4], [1]Mineralogical State Collection Munich, [2]Institute for Geosciences, University of Tuebingen; [3]Dep. Geo- and Environmental Sciences, University of Muenchen; [4]Dep. Earth and Planet. Science, University of Tokyo, Japan

Introduction

Almahata Sitta meteorite is a unique case because its parent asteroid was detected in near Earth space shortly before entering the high atmosphere and fall in North Sudan [1]. The aims of our project are investigating Almahata Sitta's (AS) magnetic signature, phase composition and mineralogy (main focus on the opaques) and getting new insights to the ureilite parent body magnetism (2008TC3 belongs to the F type asteroids). First results concerning the magnetic record of AS are found in [2,3].

Samples and methods

Quantitative chemical data of the observed opaque phases in the Almahata Sitta ureilite were obtained by electron microprobe analysis (EMPA) using a CAMECA SX100 operated at 15 keV acceleration voltage and 20 nA beam current (DEG). The observations were done on a PS of AS39 [see 2,3 for details of samples].

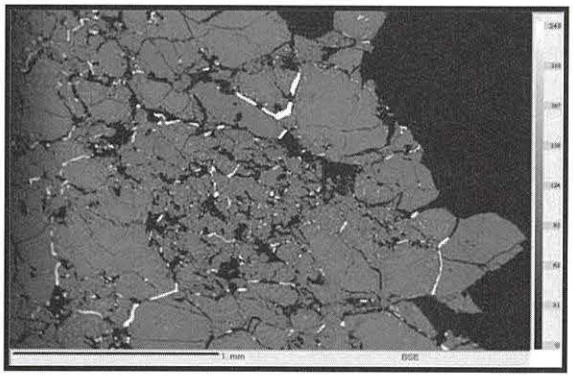

Figure 1 is a SEM backscattered image of a large portion of AS39 PS. It shows large kamacite laths or sheets seen in vein-like structures, as well as many tiny (micron-sized) particles of various metal and Fe-sulfide phases in the adjacent silicates. There is a high concentration of the tiny metal blebs in the olivines whereas the pyroxenes are nearly devoid of them. The black areas are mostly carbon-rich phases.

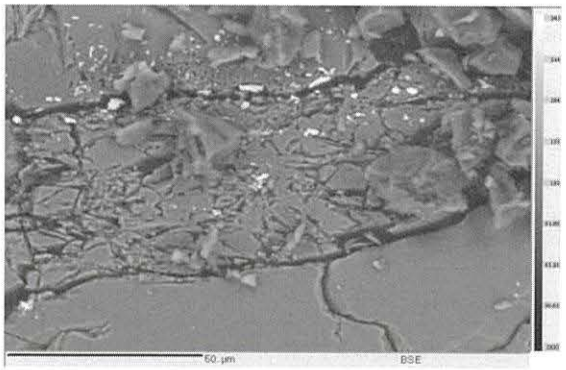

Figure 2 shows typical fracturing of olivine crystals (grey) with tiny blebs of metal (white) adjacent to metal-free pyroxene grains (below). SEM backscatter image.

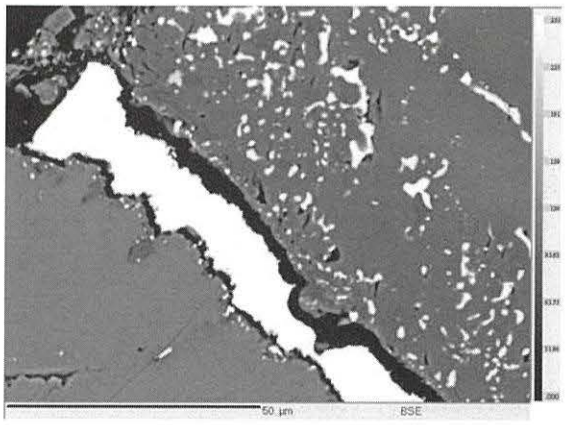

Figure 3: Sheet-like kamacite fracture filling between olivine (right) and pyroxene grains (left). The olivine grain is filled with many tiny metal blebs whereas the pyroxene is free of them. SEM backscattered image.

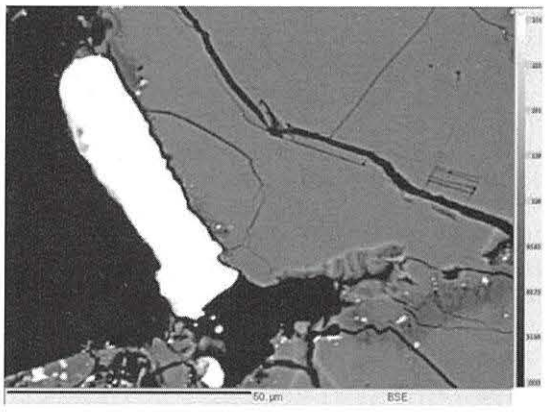

Figure 4: Kamacite sheet adjacent to pyroxene which is typically free of metal blebs. The black filling of the fracture is composed of carbon-rich phases. SEM backscatter image

Mineralogy

Kamacite

According to our EMPA analyses there are several (up to five) metal phases mainly differing in the contents of Fe, Ni, Si and Co [table 1, figure 5].

	Kamacite I n = 27	Kamacite II n = 7	Kamacite III n = 2	Kamacite IV n = 3
Fe	90.95(27)	93.28(58)	94.32(36)	95.70(46)
Ni	4.31(11)	2.21(16)	1.22(1)	2.78(13)(1)
Si	3.86(22)	3.39(49)	3.51(41)	0.22(6)
Cr	0.18(3)	0.15(2).	0.15(3)	0.13(2)
P	0.37(4)	0.43(7)	0.40(25)	0.52(31)
Co	0.20(4)	b.d.	b.d.	0.07(1)
total	99.87	99.46	99.60	99.42

The metal phase which builds up the large sheets between silicate grains (here named kamacite I) is composed of 90.95 wt% Fe, 4,31 wt% Ni, 3.86 wt% Si and 0.20 wt% Co. P and Cr are minor components. This kamacite is found in form of sheets depicting the olivines crystal shapes (figure 1). This could be used as an argument for the derivation of this kamacite by reduction of the adjacent olivine. This is in contradiction to the low iron content (15-17 wt%) of the olivin and the rim thickness of 50µm of reduced olivine which never could produce so much iron. Kamacite I contains remarkable Co, whereas the Co content of all other minerals in AS39 is near or below detection limit. This is a good hint that kamacite I is different from all other minerals in AS39 and thus has a different origin than the other metals and sulfides. In accordance with Gabriel and Pack [4] we suggest that the kamacite has been introduced into the polymict ureilite by the impact of a Ni-poor iron meteorite.

Troilite and Cr-rich troilite

Troilite is found in small grains in the carbon rich veins between the olivine and pyroxene individuals and in even smaller grains in the olivines. There it shows lines of tiny blebs which seem to follow ancient growth lines. The tiny troilite blebs in the olivines seem to be originating by reduction of the olivine along better potential paths as suggested by Berkley et al. [5].

Troilite phases with distinct chromium contents up to 6.8 wt. % have been identified as small grains in the carbon rich veins of Almahata Sitta.

Daubreelite

Daubreelite has been found in intergrowths with troilite embedded in the carbon rich veins. It shows a distinct Mn content up to 2.27 wt % similar to daubreelite from Neuschwanstein EL6 chondrite with 2.0 wt % [6].

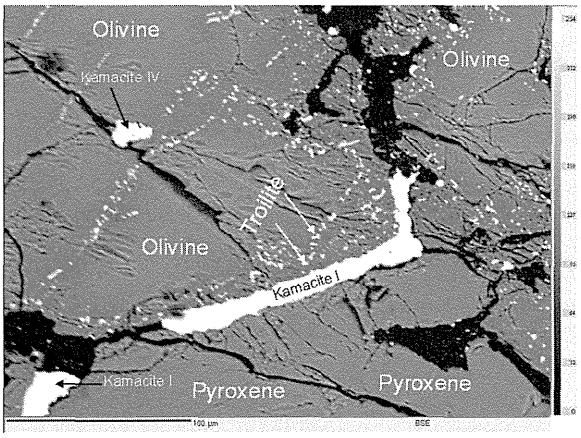

Figure 5: Distribution of mineral phases in AS 39: Kamacite type I (in veins) / III and IV (in olivine matrix), troilite (in olivine and intergrown with Kamacit I) are indicated.

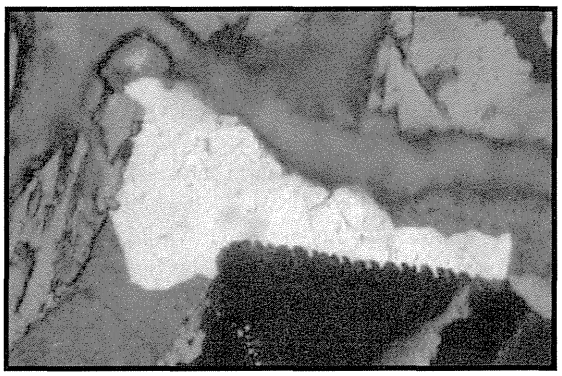

Figure 6: AS39 in optical microscope, showing typical vein metals (Kamacite), graphite and domina- ting silicate phases. The Kamacite vein metal penetrates the adjacent pyroxene along the interface, indicating high pressures (impact shock?). It seems evident that the vein metals are not indigenous but most likely represent an impactor phase.
Particle size: ca. 50µm.

Additional poster

More details about the magnetic signature, phase composition and magnetic record of Almahata Sitta samples 4 and 39 are found in our poster:
V.H. Hoffmann, R. Hochleitner, M. Torii, M. Funaki, T. Mikouchi:
Magnetism and mineralogy of Almahata Sitta.

References:

[1] Jenniskens P., et al. (2009). Nature 458: 485-488.
[2] Hoffmann V., et al. (2010). 41th LPSC, #2120.
[3] Hoffmann V., et al. (2010). Meteor. Planet. Science, subm.
[4] Gabriel A.D., Pack A. (2009). 40th LPSC, # 2462.
[5] Berkley J.L., et al. (1980). Geochim. Cosmochim. Acta 44: 1569-1597.
[6] Hochleitner, R., et al. (2004). Meteor. Planet. Sciences 39: 1643-1648.

"SNOWING" ON PLANETS AND IN THE SOLAR SYSTEM. E. Homolya[1] and Sz. Bérczi[2], [1]Eötvös University, Faculty of Science, Department of Meteorology, H-1117 Budapest, Pázmány P. s. 1/a. Hungary (emese@diex.hu), [2]Eötvös University, Institute of Physics, Cosmic Materials Space Research Group, H-1117 Budapest, Pázmány P. s. 1/a. Hungary (bercziszani@ludens.elte.hu).

Introduction: In this paper we worked out a unified p,T map of the "Snowings in the Solar System". This projection helps understanding the unusual approach of the chemical condensation model for crystallization of the solar material [1-3]. In this topics we compared the various precipitaitions occurring in planetary atmospheres and finally we compared all of them and projected them to a p,T space which contained condensations in the Solar System [4,5]. Compositional differences cause various precipitates, but the whole system of the condensing liquid droplets and crystals helps understanding the more complex process of the condensation in the Solar System. The p and T conditions prefer liquids in the higher density atmospheric regions of Jupiter, Saturn, Earth and Venus (and probably Titan). However, low pressure regions prefer sublimation type condensation.

Condensing materials in the pl anetary atmospheres: On Earth the condensing substance is water. As air mass rises and expands, the temperature of the air parcels decreases. Therefore water vapor starts condensing on condensation nuclei such as dust or salt. During this process small droplets and/or ice crystals are created [6].

The Martian atmosphere is much thiner than that of the Earth. The composition of the evolving clouds is mainly water or carbon-dioxide [7]. Due to low pressure water in liquid phase can only exist in a rather narrow range of temperature, it turnes into vapor already on +2°C. Therefore the falling precipitate is mostly CO_2-snow. However, sometimes the atmosphere is so cold that it can become saturated at a rather low humidity, therefore water ice clouds are able to come into being. According to instrumental examinations the more frequent condensation is that of the water ice. The shape of the evolving clouds is similar to the Earthly cirruses [8,9].

The conditions on Venus are much different than the other terrestrial planets mentioned above. The pressure is almost a hundred times greater then it is on Earth, and in consequence of the green-house effect the temperature is also much higher. Condensation occures in the upper atmosphere, sulfuric acid is produced through different chemical interactions.

Carbon dioxide decomposes into carbon monoxide and atomic oxygen by the effect of the solar photons. The oxygen produced is highly reactive causing reaction with sulfur dioxide to produce sulfur trioxide. This compound can react with the water vapor molecules in the Venus atmosphere and they finally result in sulfuric acid droplets, during precipitating in the atmosphere.

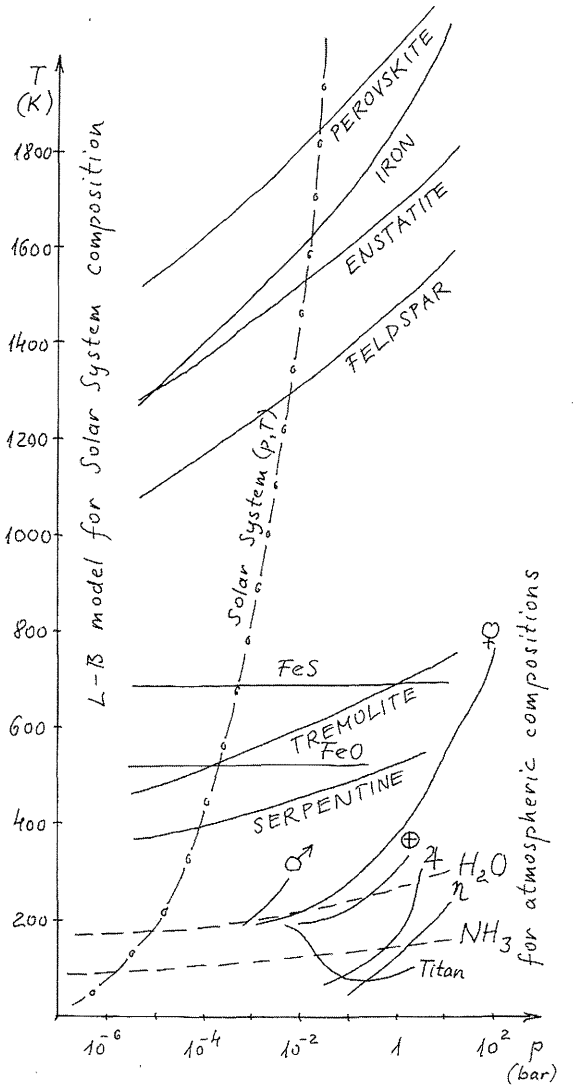

Fig. 1. Unified p,T map of the "Snowings in the Solar System". This projection helps understanding the unusual approach of the chemical condensation model for crystallization of the solar material [4,5].

Jupiter and Saturn are the most far away from the Sun amongst the planets mentioned so far. Their atmospheres are somewhat similar considering their composition and the condensations. On both of the planets there are three different condensation levels.

The cloud layer at the bottom consists of water ice. In the following layer's height the pressure and the temperature are lower, the clouds are made of ammonium hydrosulfide ice. The highest clouds, in even lower pressure and temperature conditions, are ammonia ice clouds.

It is also worth observing the clouds of Titan. According to the newest researches there are two separate types of condensation in the Titanian atmosphere at different latitudes and heights from the surface. In the polar areas ethane clouds were detected, while at lower latitudes methane clouds can be found.

Condensing materials in the protoplanetary disc (in atmosphere of the early Sun): In the protoplanetary disk that consists of gases and surrounds young protostars also occur condensations in several lines. Depending on the temperature that decreases with the increase of the distance from the Sun, minerals or other substances with different compositions condensate. Thus the condensation line means spatial sequence and also for a stated spatial point temporal sequence.

The Solar System condensation line can be devided into two parts. In the higher temperature zone, closer to the Sun, types of metals oxidize and therefore – together with silica - they compose silicates [1-3]. In the other regions, far from the Sun, the temperature is low enough for such compounds as water, ammonia and methane to become solid corpuscles. Within the protoplanetary disk the cooling possibility offers water to condense even closer to the Sun, so that it can infiltrate to the silicates condensed before, and composes hydrates with methane and ammonia [1].

Comparisons and conclusions: the whole system in one p,T space: Using the individual condensation patterns a comparison between the condensations in the planetary atmospheres and the atmosphere of the Sun can be sketched. The difference appears in the pressure and temperature conditions, the quality of the condensing substances and in the numbers of the condensation levels. However, it is important to note that several compositional differences also distinguish the condensates in special p,T regions of the p,T space. This comparison table helped students to overview the large and extended condensational sequence around Sun. An other application of the data of snowing may be its use in climate diagrams and maps [10, 11] that help visualizing climate conditions of other planets.

References: [1] Barshay S. S. & Lewis J. S. 1975: In: *The Dusty Universe*, eds. Field G. B. & Cameron A. G. W., Neale Watson Acad. Publ., New York; [2] Larimer J. W. 1967: *Geochim. Cosmochim. Acta* 31, 1215. [3] Grossmann L. 1972: *Geochim. Cosmochim. Acta* 36, 597., [4] Bérczi Sz., Lukács B. 1994: Alien Planetary Systems. in *Evolution of Extraterrestrial Materials and Structures*, KFKI-1994-22/C Report, 6-28.; [5] B. Lukács, Sz. Bérczi, A. Kereszturi (2002): Brown Dwarfs' Atmospheres: Possible Analogy for Condensation in the Solar Nebula. In LPSC XXXIII, #1472, LPI, Houston (CD-ROM); [6] Bérczi Sz. Hargitai H., Illés E., Kereszturi Á., Opitz A., Sik A., Weidinger T. (2002): *Kis Atlasz a Naprendszerről (4): Bolygólégkörök atlasza.* (Concise Atlas of the Solar System 4. Planetary Atmospheres.) ELTE TTK Kozmikus Anyagokat Vizsgáló Űrkutató Csoport, UNICONSTANT, Budapest-Püspökladány (ISBN 963 00 6314 XÖ, 963 204 061 9); [7] Kereszturi A. Éghajlatváltozás a Marson I., II. (2007), *Legkor* 52/2, p. 12-17., 52/3, p. 6-9. [8] Whiteway, J.; Komguem, L. Dickinson, C. Cook,C. Duck, T. Taylor, P. Davy, R. Seabrook, J. Fisher, D. Carswell, A. (2009): Phoenix Lidar Observations of Dust, Clouds, and Precipitation on Mars. LPSC XXXX, #2202. LPI, Houston; [9] Whiteway, J. A. et al (2009): Mars Water-Ice Clouds and Precipitation. Science, Volume 325, Issue 5936, pp. 68. [9] Mitchell, J. L. (2008): The drying of Titan's dunes: Titan's methane hydrology and its impact on atmospheric circulation. JGR, Vol. 113, E8, CiteID E08015 [10] Hargitai, H (2010): Mars climate zone map based on TES data. LPSC 41, *this volume.* [11] Hargitai, H, Sz. Bérczi, Sz. Nagy, A. Gucsik, Á. Kereszturi (2008): Mars Climate Diagram Database. LPSC XXXIX #1476. [12] Hargitai H., Bérczi Sz., Kereszturi Á., Opitz A., Sik A., Weidinger T., Tepliczky I., Bradák B. (2003): Outreach Activity of the Planetology Group of Eötvös University, Hungary: Experimental Programs and Experiments. In LPSC XXXIV, #1547, LPI, Houston (CD-ROM).

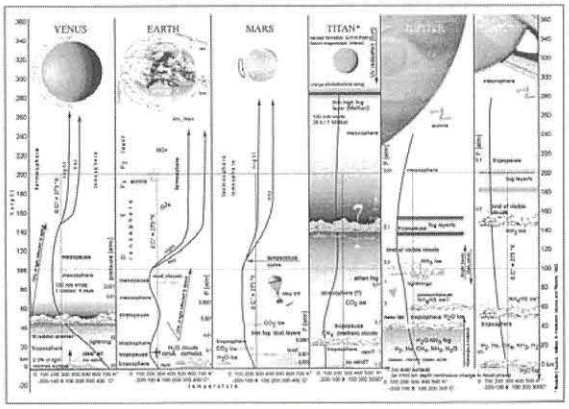

Fig. 2. Comparison of planetary atmospheres of Venus, Earth, Mars, Jupiter, Saturn and Titan in [6].

Gradual Extension of Dark Dune Spots in the Vicinity of Spiders at the Inca City Region on Mars

A. Horváth (1,2), Sz. Bérczi (1,3), A. Kereszturi (1,4), A. Sik (1,4), T. Pócs (1), E. Szathmáry (1,5);
(1) Collegium Budapest (Institute for Advanced Study), H-1014 Budapest, Szentháromság tér 2. Hungary, *(2)* Konkoly Observatory, H-1525 Budapest Pf. 67, Hungary, *(3)* Eötvös University, Inst. of Physics, Cosmic Mat. Sp. Res. Gr. H-1117 Budapest, Pázmány 1/a. Hungary, *(4)* Eötvös University, Dept. Physical Geography, H-1117 Budapest, Pázmány 1/c. Hungary, *(5)* Eötvös University, Dept. of Plant Taxonomy and Ecology, H-1117 Budapest, Pázmány 1/c. Hungary (szathmary@colbud.hu)

Introduction

The new HiRISE images by MRO space probe gave better time resolution of the surface processes than the earlier MGS and MEX images of the South Polar Region of Mars. In this work our studies were concentrated on the relation between Dark Dune Spots (DDSs) and spiders. We wanted to find evidences pro or contra concerning the phenomena connecting them. Sequence of the HiRISE images made at the Inca City Region of Mars revealed the defrosting phenomenon at springtime. In a selected region (81.45°S, 296.03°E) we studied how the initial DDS patches appear, gradually extend, coalesce and finally cease to be seen as dark spots, instead, they become visible as pale white cover on the dark surface and finally vanish. All the steps of the defrosting sequence occurred in the vicinity of well-developed spiders. However, no geyser-like outburst characteristic to the spider related gas and soil ejecting activity could be found at the same time.

Observational evidence

In late winter or at early spring growing grey splotches (we called them Dark Dune Spots) appear on dark dunes. The gradual extension of the defrosting phenomenon at springtime was in focus of our studies on the HiRISE images by MRO. In the Inca City region (81°S, 296°E) both DDS (Fig. 1., 3.) and spider phenomena occur. The relation between Dark Dune Spots and spiders may be found if they are exhibiting combined events at the same location.

Earlier the formations of spiders were interpreted by a dry, cold geyser model [1, 2, 3, 4], while the formation of the DDS was interpreted by a wet model [5, 6]. The wet character of the DDS formation was strengthened by observations that in great number of cases linear "seepage features" are moving downslope from some dark dune spots [5, 6, 7, 8].

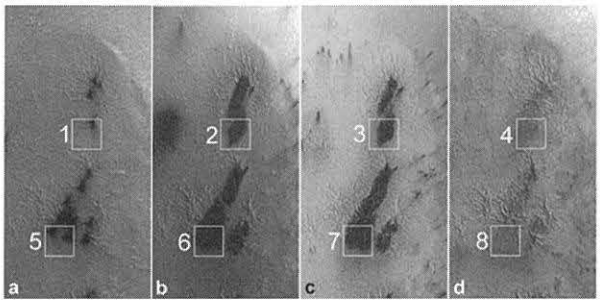

Fig. 1. Winter and spring defrosting sequence of a DDS-group at Inca City in 2007 (500x1000 m detailed frame of the MRO HiRISE images:
a) PSP_002380_0985, 01-28-2007, Ls=174.5°;
b) PSP_002868, 07-03-2007, Ls=196.2°;
c) PSP_003593, 03-05-2007, Ls=230.7°;
d) PSP_004714, 29-07-2007, Ls=289.8°).
Boxes see in Fig. 2.

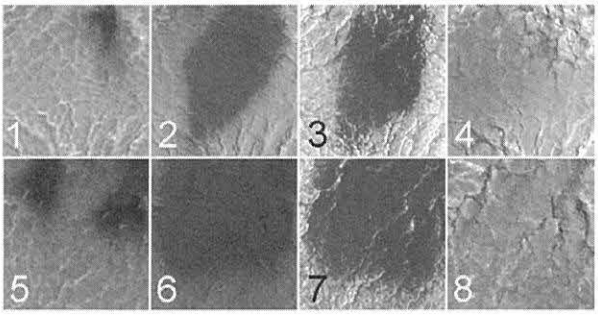

Fig. 2. 100x100 m frames of some DDS-regions from Fig. 1. in the Inca City are enlarged, where no spider centers are observed

Because the topmost layer of the frost in winter consists of CO_2, and the sublimation temperature of this CO_2, frost is lower than that of water ice, the defrosting of the frost layer begins with the CO_2, sublimation. However, the quick heating up of the CO_2, layer by the springtime solar insolation triggers prompt outburst of the CO_2, gas which produces geysers. If the defrosting of the two kinds of objects is interrelated, than a special combined effect at the springtime

defrosting process must be observed [4]. If the outburst happens earlier than the spot development, then it should show streaks and fans of dark material ejected from the spider's central portion or from parts of its "arms" and later dark spot activity should have been also connected to the spider regions. However, this is not the case and we observed a different sequence at the spots in the Inca City region: DDSs have developed also on a region where no spider center was observed (Fig. 2) [9].

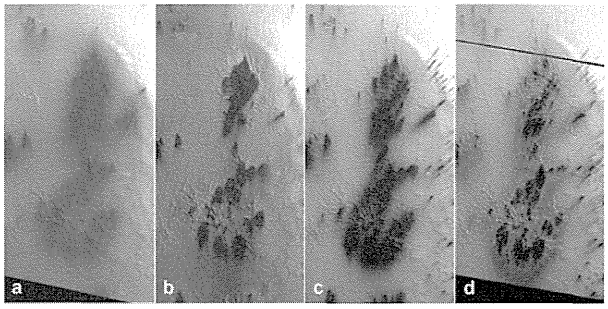

Fig. 3. Next winter and spring defrosting sequence of DDS-group at Inca City in 2009 (500x1000 m detailed frame of the MRO HiRISE images:
a) ESP_0011491_0985, 07-01-2009, Ls=187.5°;
b) ESP_011728, 26-01-2009, Ls=198.3°;
c) ESP_012256, 08-03-2009, Ls=223.3°;
d) ESP_012691, 11-04-2009, Ls=244.7°)

In our selected area we followed a DDS group during two seasonal defrosting sequences in two subsequent Martian years (2007, 2009). The spots began to appear on the white frosting territory as darker grey splotches with diffuse perimeter (Fig. 3a); later they became confined (Fig. 1a) of elongated (elliptical) or circular form (Fig. 3b) with sharper outline, but they occurred without development of diffuse fans. In a later spring period the spots enlarged and coalesced (Fig. 1b, Fig. 3c) [6]; after coalescence they extended further till they occupied a restricted territory; at the second half of springtime the spots began to disappear (Fig. 3d), but a pale grey (Fig. 1d) or white spot was visible on the surface as the remnant of the DDS activity. All the time the spots were apart from the spider centers (Fig. 2).

Conclusion: The spider activity might be a different process as compared to the DDS formation. DDS formation involves heating by insolation on places which contain remnants of another soil than the dark basaltic material: components of brines and the hypothetical Mars Surface Organism (MSO) components [5, 6], which causes the recurrence at the surface of the DDS defrosting pattern [7, 10]. Otherwise, on the near polar territory spiders in the basaltic material may be a good refuge for the putative Mars Surface Organisms [11].

References

[1] Kieffer, H.H. (2000) Annual punctuated CO_2 slab-ice and jets on Mars, *Int. Conf. Mars Polar Sci. Explor.* p. 93. [2] Ness, P.K., Orme, G.M. (2002) Spider–ravine models and plant-like features on Mars – Possible geophysical and biogeophysical modes of origin, *J. Br. Interplanet. Soc.* 55 (3–4), 85–108. [3] Piqueux, S., Byrbe, S., Richardson, M.I. (2003) Sublimation of Mars's southern seasonal CO2 ice cap and the formation of spiders, *J. Geophys. Res.* 108, 5084. [4] Christensen, P. R., Kieffer, H. H., Titus, T. N. (2005): Infrared and Visible Observations of South Polar Spots and Fans, *American Geophysical Union, Fall Meeting,* 2005, abstr. # P23C-04. [5] Horváth A., Gánti T., Gesztesi A., Bérczi Sz., Szathmáry E. (2001) Probable evidences of recent biological activity on Mars: appearance and growing of dark dune spots in the south polar region, 32nd *LPSC*#1543, poster, Houston. [6] T. Gánti, Horváth A., Sz. Bérczi, A. Gesztesi, E. Szathmáry (2003) Dark Dune Spots: Possible Biomarkers on Mars? *Origins of Life and Evolution of the Biosphere* 33: pp. 515-557, Kluwer Academic Publishers. [7] Kereszturi, A., Möhlmann, D., Bérczi, Sz., Gánti, T., Kuti, A., Sik, A., Horváth, A. (2009) Recent rheologic processes on dark polar dunes of Mars: Driven by interfacial water? *Icarus* 201, 492–503. [8] Horváth A., Kereszturi Á., Bérczi Sz., Sik A., Pócs T., Gánti T., and Szathmáry E. (2009) Analysis of Dark Albedo Features on a Southern Polar Dune Field of Mars, *Astrobiology* 9/1, pp. 90-103. [9] Horváth A., Bérczi, Sz., Sik, A., Kereszturi, A. (2009)"Inca City" DDS Test Region in Mars: New Comparisons by MRO Data, *European Planetary Science Congress* Abstracts, Vol. 4, EPSC2009-0294, 2009, Berlin, poster, CD-ROM. [10] Horváth, A. Kereszturi, A., Bérczi, Sz., Sik, A., Pócs, T., Gesztesi, A., Gánti, T. Szathmáry, E. (2005) Annual Change of Martian DDS-Seepages, 36th *LPSC*, #1128. poster, Houston. [11] Szathmáry E., Gánti T., Pócs T., Horváth A., Kereszturi Á., Bérczi Sz., Sik A. (2007) Life in the Dark Dune Spots of Mars: a testable hypothesis, Chapter 13. in: *Planetary Systems and the Origins of Life*. R. Pudritz, P. Higgs, J. Stone, Eds. Cambridge Astrobiology, Cambridge University Press, pp. 241-262.

Relict grains in seven unmelted micrometeorites and their common link to chondrules in carbonaceous chondrites. N. Imae[1], S. Taylor[2], and N. Iwata[3] [1]National Institute of Polar Research, 10-3, Midori-cho, Tachikawa, Tokyo 190-8518 (imae@nipr.ac.jp), [2]U.S. Army Cold Regions Research and Engineering Laboratory, Hanover, New Hampshire 03755-1290, and [3]Department of Earth and Environmental Sciences, Yamagata Univ., 1-4-12, Kojirakawa, Yamagata 990-8560, Japan.

Introduction:

The compositions of coarse-grained relict minerals in micrometeorites (MMs) have been compared to minerals in carbonaceous chondrites (CCs) [1-2] and in ordinary chondrites [3] where a relationship between relict bearing MMs and chondrules was found [4]. The relationship of micrometeorites (MMs) with chondrites is important for understanding of origins of MMs. Although CCs have been subdivided into at least 10 distinct groups based on their chemistry [5], MMs with affinities to CCs have not been linked to those groups.

We analyzed 103 MMs bearing coarse-grained relict olivines and low-Ca pyroxenes among 475 MMs from Tottuki icefield [6] and South Pole Water Well [7]. Here we focus on classifying 7 unmelted MMs of ~50-200 μm in diameter with coarse-grained relicts.

Experiments:

Polished sections of MMs and various kinds of unequilibrated chondrites (CM2, CR2, Tagish Lake, CO3.0, CO3.2, CV3, H3.2, LL3.0-3.3, L3.7, R) were analyzed by an electron microprobe analyzer (JEOL JXA-8200) and observed in the BSE images. Four kinds of plots of FeO-CaO, FeO-Al_2O_3, FeO-MnO, and FeO-Cr_2O_3 were used for comparisons of compositions of olivines and low-Ca pyroxenes between relicts in MMs and minerals.

Results:

MMs: The relict mineral assemblages and their major compositions of the 7 MMs are as follows (Fig. 1; Fig. 2a,d): (1) olivine ($Fa_{1.5}$, Fa_1, $Fa_{0.7}$, respectively) and Fe-Ni metal (kamacite) in TT001b141, SP00_93, and SP00_191, (2) low-Ca pyroxene ($En_{93}Fs_4Wo_3$) in 53D01, (3) olivine ($Fa_{1.8}$), low-Ca pyroxene ($En_{94}Fs_2Wo_4$), and Fe-Ni metal in SP00_190, (4) low-Ca pyroxene ($En_{94}Fs_2Wo_4$), high-Ca pyroxene, Fe-Ni metal, and plagioclase in 53D16, and (5) olivine (Fa_1), low-Ca pyroxene ($En_{98}Fs_1Wo_1$), and Fe-Ni metal in 53D18. Among these unmelted MMs, three MMs (53D16, 53D01, and SP00_190) have a ~10 μm thick melted rim, formed during the atmospheric entry heating. The remaining four MMs (TT001b141, SP00_93, SP00_191, and 53D18) did not have a distinct rim (Fig. 1).

53D16 (Fig. 1d), 53D01 (Fig. 1e), and SP00_190 (Fig. 1f) all have small (less than ~10 μm) Fe-Ni metal droplets, and some droplets are poikilitically enclosed in low-Ca pyroxenes (Fig. 1). Rounded olivines in SP00_190 (Fig. 1f) and 53D18 (Fig. 1g) are enclosed in low-Ca pyroxenes. SP00_191 has ~2 μm Fe-Ni metal droplets, smaller than those in SP00_190 and 53D18, enclosed in forsteritic olivines (Fig. 1). TT001b141 and SP00_93 show similar textures consisting of forsteritic olivine aggregates.

CCs: A common feature of forsteritic olivines in CCs is a negative correlation of CaO and Al_2O_3 content with FeO and a positive correlation of MnO and Cr_2O_3 content with FeO. Ca and Fe can also be used to distinguish between the CM2 and CR2 chondrites (Fig. 2b). The CaO contents (0.3-0.7 wt%) of low-Ca pyroxenes in the CM2 chondrite are higher than those in the CR2 chondrite (0.1-0.3 wt%) (Fig. 2b). The Al_2O_3 behaves similarly. A photo of a chondrule is shown in Fig. 1h.

UOCs: The compositions of olivines are more heteorogeneous (up to ~45 wt% of FeO) than those in CCs.

Discussion:

The poikilitic textures of Fe-Ni droplets observed in 4 MMs (Fig. 1) are common in CCs (Fig. 1h), but not in ordinary chondrites. Two MM showing sintered texture of forsteritic olivine aggregates are similar to granoblastic olivine aggregate chondrules observed in the Vigarano CV3 chondrite [8].

The seven MMs are similar to type I chondrules in CCs based on the detailed comparison of MMs with CCs. Among them, the chemical groups for the four unmelted MMs were determined using textures and compositions of olivines and low-Ca pyroxenes as (1) SP00_190 = CM2, (2) 53D01 and 53D16 = CO3.0, and (3) 53D18 = CR2 (Figs. 1-2). The diameter of 53D01 and 53D16 60-70 μm and 100 μm, respectively, and they represent from half to nearly whole chondrule because the mean diameter of the CO3 chondrite is 150 μm [9]. While SP00_190 (~110 μm in diameter) and 53D18 (~200 μm in diameter) are both less than half chondrule, since the mean diameter of CM2 is 300 μm and that of CR2 is 700 μm, respectively [9].

References:

[1] Steele I. M. (1992) *GCA*, 56, 2923-2929. [2] Beckering W. and Bichoff A. (1995) *Planet. Space Sci.*, 43, 435-449. [3] Genge M. J. (2008) *Geology*, 36, 687-690. [4] Genge M. J. (2005) *Meteorit. Planet. Sci.*, 40, 225-238. [5] Weisberg M. K. (2006) In Meteorites and the Early Solar Sytem II. [6] Iwata N. and Imae N. (2002) *AMR*, 15, 25-37. [7] Taylor S. et al. (1998) *Nature*, 392, 899-903. [8] Libourel G. and Krot A. N. (2007) *EPSL*, 254, 1-8. [9] Scott E. R. D. and Krot A. N. (2005) In Chondrules and the Protoplanetary Disk.

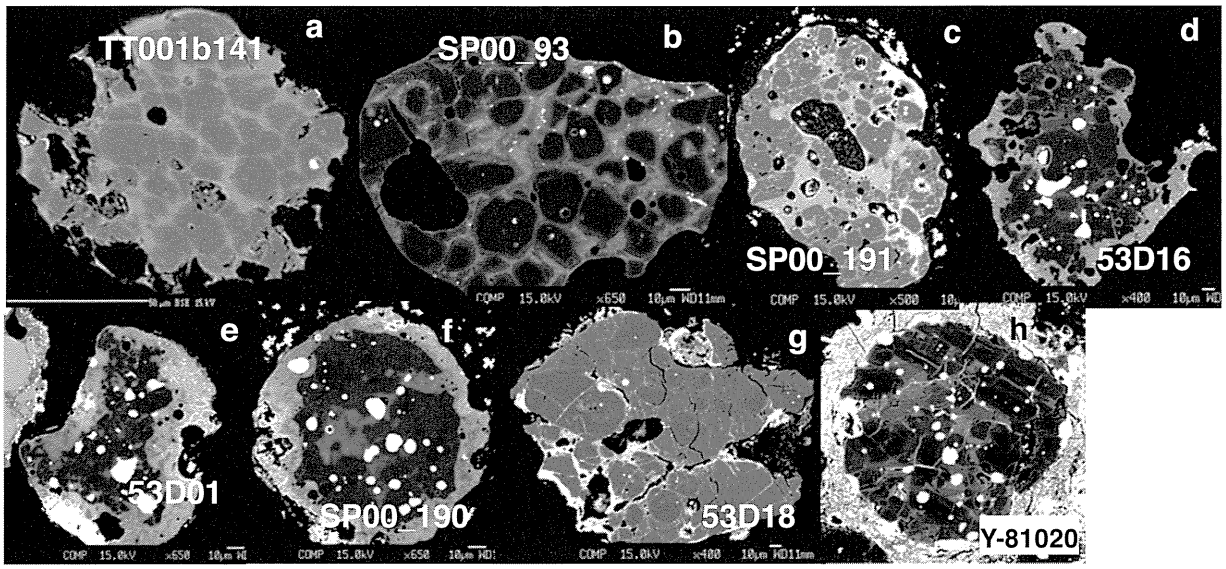

Fig.1. BSE images of studied unmelted MMs and a chondrule. (a) TT001b141 (Main relict=Ol). (b) SP00_93 (Ol). (c) SP00_191 (Ol). (d) 53D16 (LCP). (e) 53D01 (LCP). (f) SP00_190 (Ol+LCP). (g) 53D18 (Ol+LCP). (h) A chondrule (~120 μm in diameter) in Yamato 81020 CO3.0 (LCP).

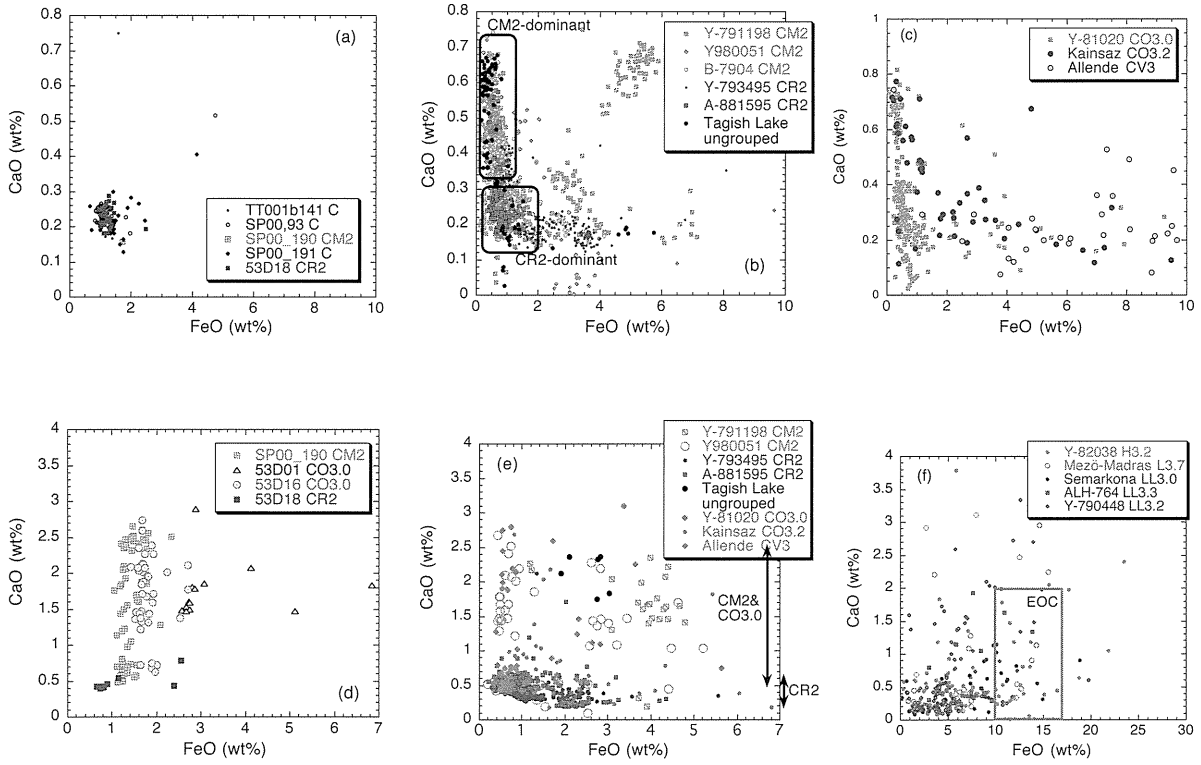

Fig. 2. FeO-CaO plots for olivines and low-Ca pyroxenes in unmelted MMs and unequilibrated chondrites. (a) Magnesian olivines in MMs. (b) Magnesian olivines in aqueously altered carbonaceous chondrites. (c) Magnesian olivines in anhydrous carbonaceous chondrites. (d) Low-Ca pyroxenes in MMs. (e) Low-Ca pyroxenes in CCs. (f) Low-Ca pyroxenes in UOCs.

Rare Earth Element Measurements and Mapping of Minerals in the Allende CAI, 7R19-1, by NanoSIMS. M. Ito[1,2] and S. Messenger[2]. [1]Lunar & Planetary Institute, 3600 Bay Area Blvd, Houston TX 77058, [2]ARES, NASA Johnson Space Center, 2101 NASA parkway, Houston TX 77058

Introduction: The rare earth elements (REEs) are concentrated in CAIs by ~20 times the chondritic average [e.g., 1]. The REEs in CAIs are important to understand processes of CAI formation including the role of volatilization, condensation, and fractional crystallization [1, 2].

The *in-situ* ion microprobe analyses of the REE in individual minerals within a petrographic context are a well-established tool for understanding the crystallization and metamorphic histories of igneous phases [e.g., 3]. However the spatial resolution of REE measurements by a conventional ion microprobe (~20 μm) is not adequate to resolve heterogeneous distributions of REEs among/within minerals. We have developed methods for measuring REE with the NanoSIMS 50L at smaller spatial scales.

In this study, we have established analytical procedures for accurate REE measurements of minerals in CAIs (0.01-10 ppm/0.1-100×CI chondrite) with the JSC NanoSIMS 50L. We present REEs patterns and their concentrations in minerals of an Allende Type-A CAI, 7R19-1, using three different methods; spot analysis, line profile and REE imaging. The purpose is to constrain formation processes of CAIs on the basis of REE distributions in CAI constituent minerals.

Experimental: We synthesized a series of diopside ($CaMgSi_2O_6$) glass standards doped with selected trace and REEs optimized for simultaneous measurement of 7 masses by NanoSIMS (Table 1). These standards were used to accurately determine relative sensitivity factors and oxide-to-element ratios, as well as finding target REE peaks.

Table 1. synthetic diopside glasses

	Wt %	REEs
GM1	500 ppm	La, Nd, Er, Lu
GM2	500 ppm	Ce, Eu, Tb, Ho
GM3	500 ppm	Gd, Tm
GM4	500 ppm	Sm, Yb
GM5	500 ppm	Sr, Ba, Pr, Dy
GM6	100 ppm	14 REEs + Ba

A focused O^- ion beam was rastered over 5×5 to 15×15 μm regions depending on REE concentrations. Secondary [REE^+] ions were measured in multidetection mode with 7 electron multipliers at a mass resolving power of ~3000. An energy offset of -60V was applied to reduce interferences from complex molecular ions in the mass range of REEs following previously established techniques [3]. Using 3 different trolley positions with fixed magnetic field we performed the REE measurements for CAI minerals according to the sequence shown in Table 2. The integration time for each measurement was typically ~2 hours. Data were corrected for EM dead time, and REE abundances were corrected for contributions from unresolved $REEO^+$ peaks.

Table 2. Trolley settings

	1	2	3
Trolley 1		^{28} or ^{29}Si	
Trolley 2	^{138}Ba	^{138}La	^{140}Ce
Trolley 3	^{141}Pr	^{144}Nd	^{147}Sm
Trolley 4	^{153}Eu	^{160}Gd	^{159}Tb
Trolley 5	^{163}Dy	^{165}Ho	^{167}Er
Trolley 6	^{169}Tm	^{174}Yb	^{175}Lu
Trolley 7		$^{165}Ho^{16}O$	

We have also developed a method to obtain quantitative images of selected REEs (La, Nd, Sm, Eu, Ho and Tm) within/among CAI minerals of spinel, melilite, fassaaite and pervskite with a spatial resolution of 1.6 μm. (5-1500×CI)

Oxide-to-element ratios and relative sensitivity factors: Contribution of monoxide ions to REE peaks (e.g., $^{139}La^{16}O^+$ to $^{155}Gd^+$) were corrected using oxide-to-element ratios, ($REEO^+/REE^+$). The ratios were determined by diopside glass standards doped with selective REEs (Table 1) such that they are free of oxide interferences from lower mass REEs with 60 V of energy offset (Fig. 1). Interference from monoxide ions was most severe for Gd and Tb, and the results for these REEs sometimes show large uncertainties.

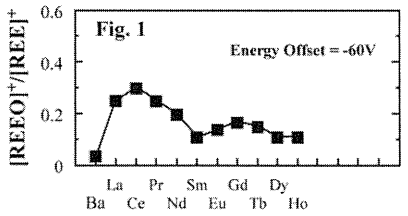

To convert ion intensities to absolute REE abundances, we need to know the relative sensitivity factors (RSFs) for each REE, defined by

the relation: $(REE/Si)_{conc.}/(REE^{+}/Si^{+})_{NanoSIMS}$. RSFs were determined by the diopside glass standards and applied to obtain REE abundances of the analysis spots. Our RSFs normalized to La are similar to those from two ion micro probe laboratories (Fig. 2) [4, 5]. REE abundance measurements yielded reproducibility and accuracy, 0.5-2.5 % and 5-25 %, respectively.

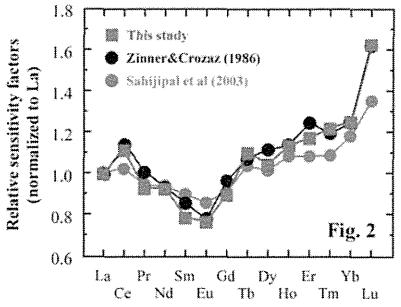

REE spot analyses for CAI 7R19-1: We determined abundances and spatial distributions of REEs in core and rim within single crystals of fassaite, and adjacent melilite with 5-10 μm spatial resolution. REE patterns and abundances for melilite and fassaite in this study (Fig. 3) are consistent with previous works for Type A CAIs [e.g., 6, 7].

The REE abundances in fassaite core and rim are 20-100 times CI abundance but show a large negative Eu anomaly, exhibiting a well-defined Group III pattern. This is consistent with previous work [8]. On the other hand, adjacent melilite shows a modified Group I pattern; Light REE enrichment and slightly positive anomalies of Eu and Yb. However, some melilites showed volatility or igneous derived REE patterns. REE abundances of melilite (2-10×CI) were lower than that of fassaite. These patterns suggest that fassaite crystallized first followed by a crystallization of melilite from the residual melt. REEs in the 7R19-1 were fractionated when the CAI crystallized from an original melt. The most volatile elements of Eu and Yb were lost by vaporization when the CAI melted. This suggests that melilite was melted and partially vaporized.

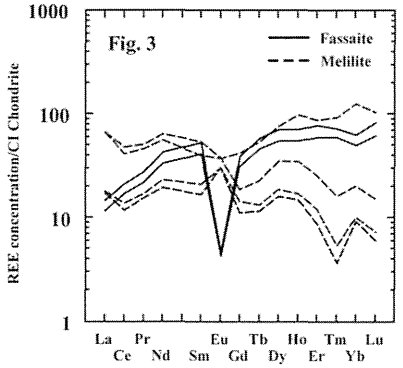

REE mapping of CAI minerals: The first attempt to observe REE distributions by mapping with a conventional SIMS was done for ureilite meteorites by [9]. They reported distributions of selected light REEs in C-rich matrix from ureilites but no quantitative information. Figure 4 shows REE images of La, Nd, Sm, Eu, Ho and Tm in CAI minerals measured by the JSC NanoSIMS 50L in order to study micro distributions of REEs in spinel, melilite, fassaite and perovskite. We found heterogeneous distributions of REEs in minerals of 14 - 67×CI, and hot spots in perovskites of 100 - 1500×CI (Fig. 4). REE abundances in these minerals are consistent with those determined by spot analyses in this study and previous works [10].

References: [1] Grossman L. 1980. *Ann. Rev. Earth. Planet. Sci.* **8**:559-608. [2] Boynton W.V. 1984. *In* Reviews in Mineralogy. Ed. Ribbe P.H. Vol. 21, 1-24. [3] Crozaz G. and Zinner E.K. 1985. *Earth Planet. Sci. Lett.* **72**:41-52. [4] Zinner E.K. and Crozaz G. 1986. *Int. J. Mass Spectrom. Ion Processes* **69**:17-38. [5] Sahijipal S. et al. 2003. *Proc. Indian Acad. Sci.* **112**:485-498 [6] Kennedy A.K. et al. 1997. *Geochim, Cosmochim. Acta.* **61**:1541-1561. [7] Simon S. et al. 1991. *Geochim, Cosmochim. Acta.* **55**:2635-2655. [8] Yurimoto H. et al. 1998. *Science* **282**:1874-1877. [9] Guan Y. and Crozaz G. 2000. *Meteorit. Planet. Sci.* 35:131-144. [10] Simon et al. 1999. *Geochim, Cosmochim. Acta.* **63**:1233-1248.

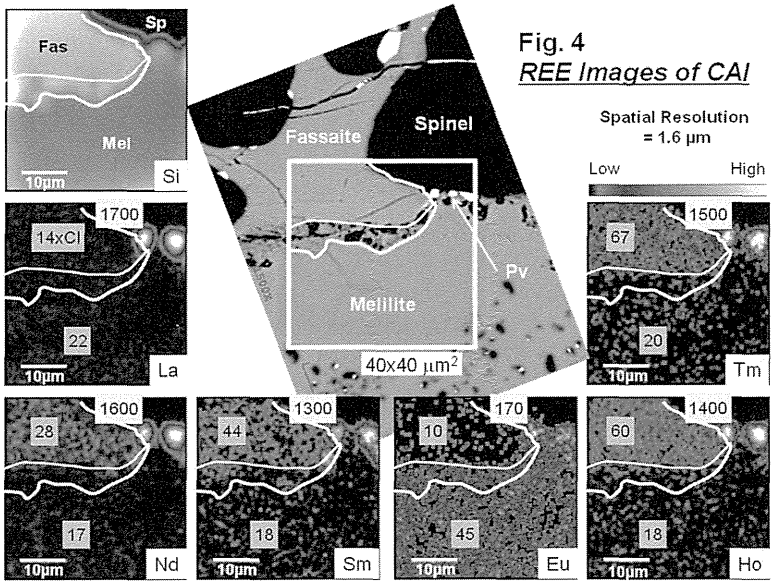

Petrographic study of Allan Hills 77257 (ureilite) and Allan Hills 78113 (aubrite) meteorites.

S. Józsa[1], I. Gyollai[2], Sz. Bérczi[2], Sz. Nagy[1], Gy. Szakmány[1], A. Gucsik[3], K. Ninagawa[4] & H. Nishido[5] [1]Eötvös University, Department of Petrology and Geochemistry, Pázmány Péter sétány 1/c., H-1117 Budapest, Hungary; [2]Eötvös University, Cosmic Materials Space Research Group, Pázmány Péter sétány 1/a., H-1117 Budapest, Hungary; [3]Max-Planck Institute for Chemistry, Becherweg 27, D-55128 Mainz, Germany; [4]Department of Applied Physics, Okayama University of Sciences, 1-1 Ridai-cho, Okayama, 700-0005, Japan; [5]Research Institute of Natural Sciences, Okayama University of Science, 1-1 Ridai-cho, 700-0005, Okayama, Japan.

Introduction

The first overview of petrological studies of NIPR Collection have been made by Yanai and Kojima [1]. According to Rubin et al. [2], the ureilites probably formed from carbonaceous chondritic material (CV-chondrites) by impact melting process. Nakamuta et al. [3] observed dendritic-like olivine, piroxene, graphite which were forming by igneous process, but the presence of diamond assuming a later impact event(s) in this material.

According to Bérczi et al. [4] the ureilite shows characteristic texture by carbon diffusion and iron reduction. On the other hand, Bérczi et al. assumed that protolite of the aubrite has had to be EH-chondrites [5].

Experimental Methods

The mineral assemblages and textures were characterized by a Nikon Eclipse LV100POL optical microscope at Eötvös Loránd University of Budapest, Hungary.

The measurements were performed on a Renishaw RM1000 confocal edge filter-based micro-Raman spectrometer. A 632.8 nm He-Ne served as excitation source, its 17 mW power was focused into surface of the samples. The laser operated with a thermoelectrically cooled charge-coupled device (CCD) array detector. A 1200 lines/mm grating monochromator provided the spectral resolution (apparatus function) of 3–4 cm^{-1}. The spectra were calibrated with the Rayleigh line and 520.5 cm^{-1} of Si-standard. The obtained spectra were compare with database of Renishaw and RRUFF-Arizona using Grams/32 software.

Results

Allan Hills 77257-ureilite: This sample has coarse grained texture and contains abundant carbon filled veins at the rim of host minerals and in its fractures. Some of these veins sometimes show worm-like texture, which could be contain diamond and graphite. The sample shows granular and poicilitic texture, mechanical twins. The exsolution lamellae are common in pyroxenes. The sample contains splashes of metal (iron-nickel) and troilite. Between those pyroxene grains which show mechanical twins, maskelynite can be observed.

Allan Hills 78113-aubrite: In spite of ureilite, the carbon phases occur not only at the rim of host minerals, but it could be observe such as round-like splashes in the grains. The rock-forming minerals have worm-like rim, which might be caused by the shock melting process. The OM-images which were taken by reflected light evidently show that carbon in aubrite contains more diamond than in ureilite. At rim of the carbon veins silicate melt can be observed. The melt pocket in carbon phase contains pyroxene. Both of aubrite and ureilite have high chromium content. Similarly to ureilite, the piroxene exhibit mechanical twins, exsolution lamellae, and high abundance of small fractures. However, some of pyroxenes show zonality. The OM-image in reflected light show that the rate of reflectance of minerals is less decreasing at the rim than in core region. The iron-nickel metal phase shows simplectitic intergrowth with smaller olivine grains.

Summary

Both of ureilite and aubrite show igneous texture (worm-like and dendritic-like) and shock metamorphic features (diamond). The presence of maskelynite is indicating S5 shock stage level on Stöffler scale. Both types of meteorite influenced by carbon diffusion and reduction.

Acknowledgements

We are grateful to the NIPR Antarctic Meteorite Research Center, Tokyo (to Prof. Kojima), for the loan of the Antarctic Meteorite Collection and to LRG (Eötvös University) and University of Vienna (to Professor Lein) for assistance with the analytical instruments. We are grateful to Professor Csaba Szabó and Professor C. Koeberl for advices in petrography. We are grateful to Prof. E. Libowitzky, Prof. L. Nasdala (University of Vienna), and to M.Veres (MTA-SZFKI) for assistance in micro-Raman investigation.

References

(1)Yanai K. and Kojima H. (*1987*): Photographic Catalog of the *Antarctic Meteorites*, NIPR.

(2) Rubin A. E. (1988): Meteoritics 23, 333-357

(3) Nakamuta et al (2005): LPSC XXXVI. 1089.pdf

(4)Bérczi Sz. et al.(1999): LPSC XXXI. 1199.pdf

(5)Bérczi Sz., S. Józsa, Zs. I. Kovács, B. Lukács, Gy. Szakmány (2004): Acta Mineralogica Petrographica, Szeged, XLV/2. 55-60.

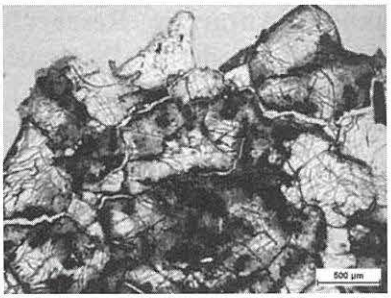

OM-image of aubrite. Picture width 3 mm (plane-polarised light)

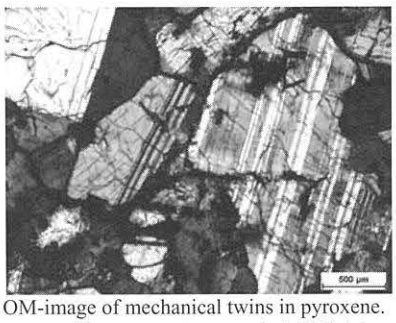

OM-image of mechanical twins in pyroxene. Picture width 3 mm (cross-polarised light).

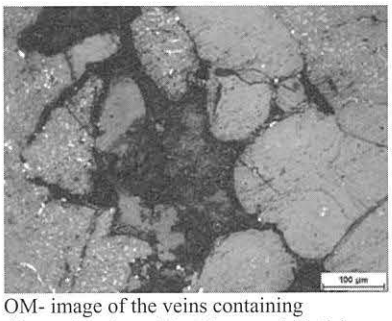

OM- image of the veins containing diamond and graphite. Picture width 0.6 mm (reflected light)

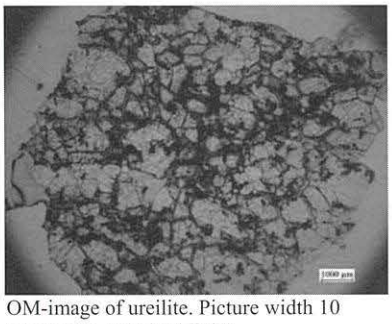

OM-image of ureilite. Picture width 10 mm (plane-polarised light)

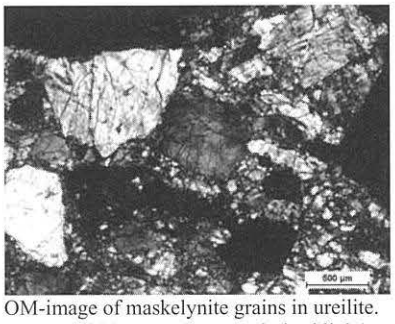

OM-image of maskelynite grains in ureilite. Picture width 3 mm (cross-polarised light)

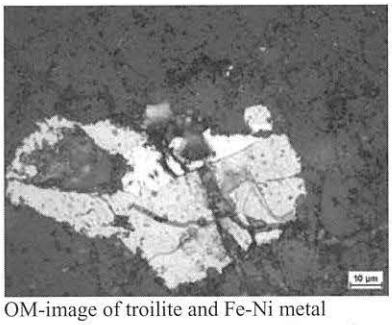

OM-image of troilite and Fe-Ni metal assemblages. The vein is rich in diamond. Picture width 0.1 mm (reflected light)

Fig. 1. Characteristic features in aubrite and ureilite thin sections.

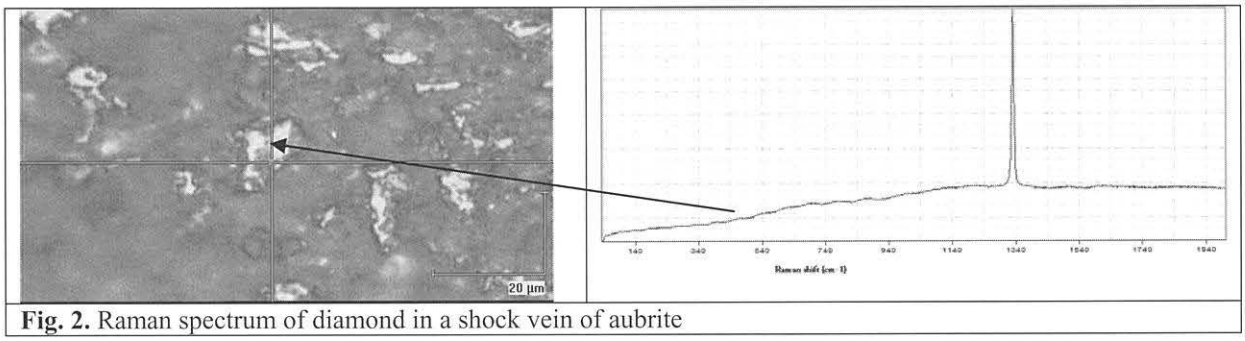

Fig. 2. Raman spectrum of diamond in a shock vein of aubrite

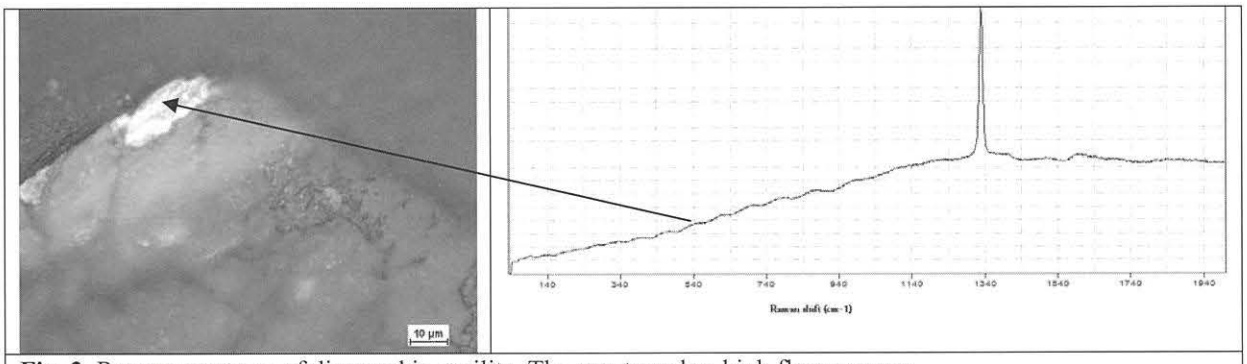

Fig. 3. Raman spectrum of diamond in ureilite. The spectrum has high fluorescence.

Collection of the Asuka 09 meteorites by the 51st Japanese Antarctic Research Expedition: A preliminary report. H. Kaiden[1,2], H. Kojima[1,2] and S. Goderis[3]. [1]National Institute of Polar Research, Tachikawa, Tokyo 190-8518, Japan (e-mail: kaiden@nipr.ac.jp). [2]The Graduate University for Advanced Studies, Tachikawa, Tokyo 190-8518, Japan. [3]Vrije Universiteit Brussel, Pleinlaan 2, B-1050 Brussels, Belgium.

Among the 16200 meteorite specimens that had been collected by the Japanese Antarctic Research Expedition (JARE) by the end of 2009, nearly 2000 specimens were found around the Sør Rondane Mountains (SRM) [1], which are located about 400 km west of the Yamato Mountains and 600 km southwest of the Syowa Station (69° 00.4′ S, 39° 35.4′ E), Queen Maud Land, East Antarctica (Fig. 1).

Three chondorites, later named Asuka-8601, Asuka-8602 and Asuka-8603, were accidentally found by a glaciological party of the 27th JARE (JARE-27) on the bare ice field near Mt. Balchen, the eastern end of the Sør Rondane Mountains, in the 1986–1987 field season [2]. Following the first finding of the Asuka meteorites, JARE-29 (1987–1989) and JARE-31 (1990–1991) performed systematic searches for meteorites around the SRM, and collected ~300 Asuka-87, ~1500 Asuka-88 and ~50 Asuka-90 meteorites [3, 4] (Table 1). Since the Asuka Station (71° 31.6′ S, 24° 08.3′ E), after which the meteorites found around the SRM were named, became unmanned, search for meteorites around the area had not been conducted.

A meteorite search team consisting of four Japanese and two Belgian of the JARE-51 performed the first search for meteorites around the SRM since November 1990. The team reached the Mt. Balchen area that is located at the eastern end of the SRM on January 2, 2010, and conducted systematic meteorite searches from January 4 to 24, 2010. They searched bare ice fields and moraines around Mt. Balchen for meteorites mainly by means of skidoos and successfully found 635 meteorite specimens in total (Table1, Fig. 2). Although most of the collected meteorites are ordinary chondorites, one iron and two ureilites were identified in the field. The ureilires are most likely fragments of one specimen. The meteorites collected by JARE-51 will be termed Asuka 09 meteorites.

There are two main areas that are prolific in meteorites around the SRM: Mt Balchen area and Nansen Icefield, which are located in the southern part of the SRM (Fig. 1). The total weight of the meteorites collected by JARE-51 around the Mt. Balchen is approximately 20 kg; the largest one is a ~5-kg ordinary chondrite. The average weight of the meteorite fragments is estimated to be a couple of dozen grams, which is consistent with the observation that there a is remarkable feature of the occurrence of the Asuka meteorites [5]: the specimens found especially on the upstream side of Nansen Icefield are mostly complete large stones with a fusion crust, whereas most specimens found near Mt. Balchen have been broken into fragments by weathering.

The meteorite search has been conducted as a joint Japanese-Belgian meteorite expedition with the support of the International Polar Foundation and the Belgian Federal Science Policy Office [6].

References: [1] Kojima H. et al. (2008) *Meteorit. Planet. Sci.*, *43*, A184. [2] Nishio et al. (1987) *Antarct. Meteorites*, *XII*, 1–2. [3] Yanai K. et al. (1993) *Proc. NIPR Symp. Antarct. Meteorites*, *6*, 137–147. [4] Yanai K. et al. (1994) *Proc. NIPR Symp. Antarct. Meteorites*, *7*, 1–8. [5] Kojima H. (2006) *The History of Meteoritics and Key Meteorite Collections: Fireballs, Falls and Finds (eds, McCall G. J. H. et al.), Geol. Soc. London, Spec. Pub.*, *256*, 291–303. [6] Claeys Ph. et al. (2010) *this volume*.

Table 1. Number of meteorites found around the Sør Rondane Mountains (Asuka meteorites)

Field season (Name)	JARE	Number of meteorites	Area
1986–1987 (Asuka-86)	JARE-27	3	Mt. Balchen
1987–1988 (Asuka-87)	JARE-29	~100 ~200	Mt. Balchen Nansen Icefield
1988–1989 (Asuka-88)	JARE-29	~1500	Nansen Icefield
1990–1991 (Asuka-90)	JARE-31	48	Mt. Balchen
2009–2010 (Asuka 09)	JARE-51	635	Mt. Balchen

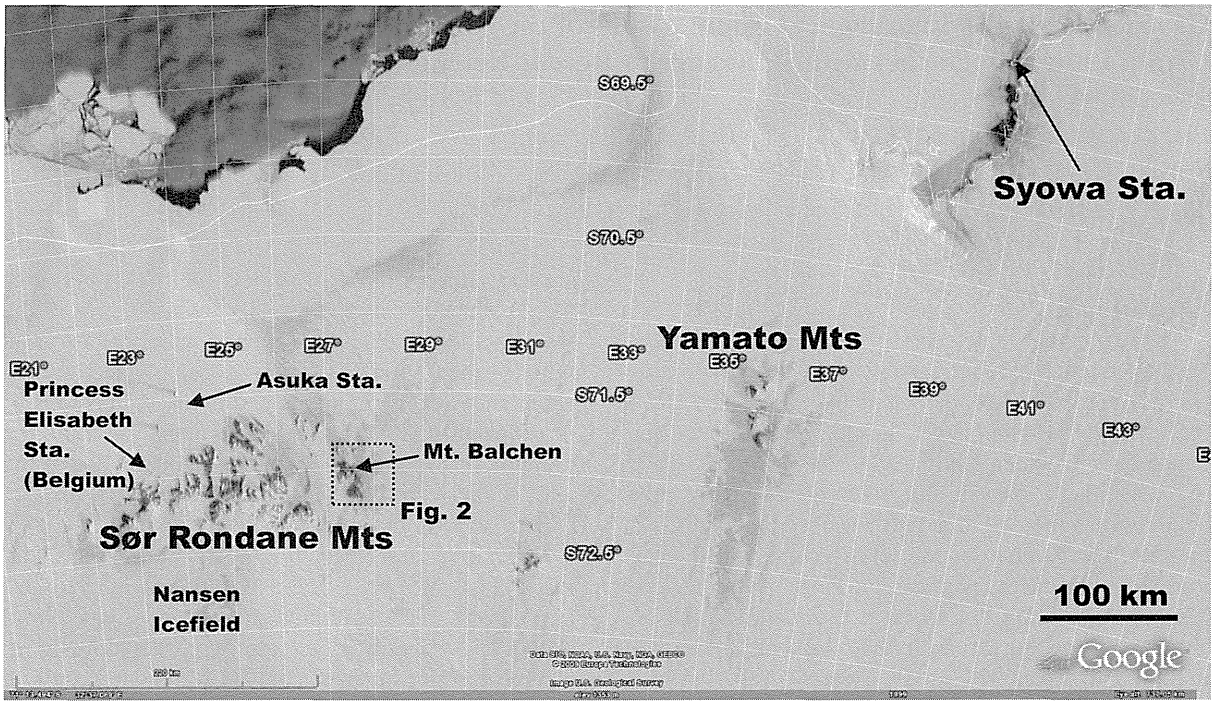

Fig. 1. Satellite image of ice fields around the Yamato Mountains and the Sør Rondane Mountains

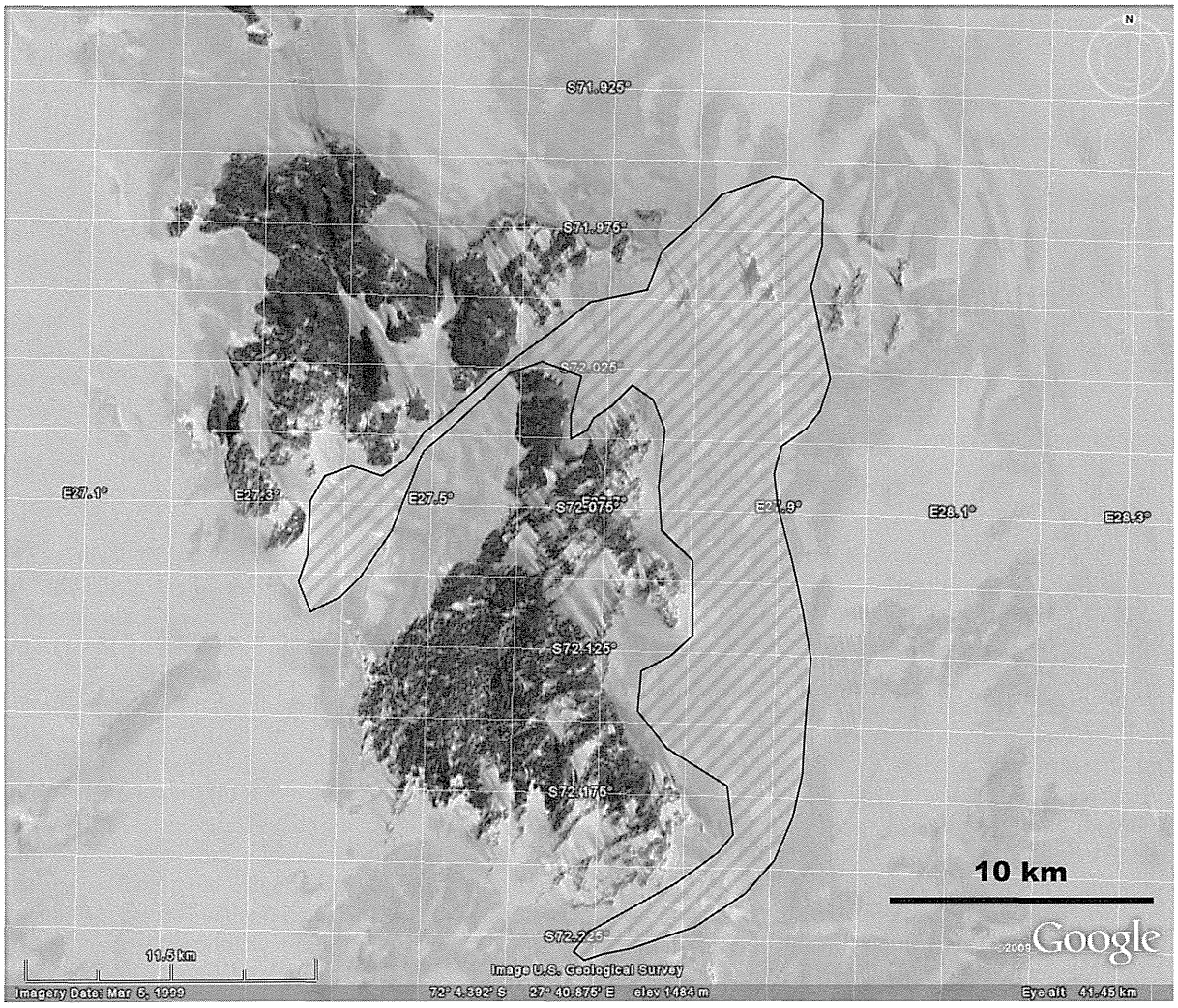

Fig. 2. Meteorite search area (shaded) around Mt. Balchen in the Sør Rondane Mountains

Geochemical and Mineralogical Comparisons of the Dhofar489 and Y-86032 Group Lunar Meteorites with Reference to Recent Remote Sensing Data. Y. Karouji[1], H. Takeda[2], A. Yamaguchi[3], L. Nyquist[4], D. Bogard[4], and M. Ebihara[5], [1]Res. Inst. for Sci. and Engin., Waseda Univ., [2]Dept. of Earth & Planet. Sci., Univ. of Tokyo, (Chiba Inst. of Tech., Forum Res.), [3]National Inst. of Polar Res., [4]ARES, Mail Code KR, NASA Johnson Space Center, [5]Graduate School of Sci., Tokyo Metro. Univ..

Introduction:

Two lunar meteorite groups that likely originated on the lunar farside have been reported [1-3]. Y-86032 was recovered by the 27*th* JARE Party [4]. The Dhofar 489 group [3] was found in Oman, and includes Dhofar 307, 309, 489, 908 etc. [5]. Although low Th and FeO concentrations are common features of the two groups, the types of mineral fragments and clasts are different. Pyroxene fragments similar to those of so-called Mg-suite rocks are dominant in the matrices of the Y-86032 group, but more olivine fragments are found in the matrices of the Dhofar 489 group. Anorthositic clasts are major clasts in both groups, but more magnesian anorthosites are dominant in the Dhofar 489 group. Because a full description of the Y-86032 clasts has been published recently [2], we report comparisons of the two groups with new data for Dhofar 307 and with reference to the Kaguya remote sensing data.

Samples and Experimental Methods:

The PTSs of Yamato (Y-) 86032 and one PTS of Dhofar 307 were examined by optical and scanning electron microscopes (SEM; JEOL JSM5900LV) equipped with an energy dispersive spectrometer (EDS; Oxford LINK ISIS) at the National Inst. of Polar Research, Tokyo (NIPR). Compositional data for mineral phases were obtained with EPMA; JEOL JXA8200M and 8900 at NIPR and at the Ocean Res. Inst., Univ. of Tokyo (ORI). Chemical compositions of minerals of Dhofar 307 were analysed by EPMA, at ORI.

Results:

Y-86032 [2] is composed of several types of feldspathic clasts, granulitic breccias, and minor basaltic clasts set in a clastic matrix. An97 anorthosite has An contents similar to those of nearside FANs, and Mg number (Mg' = molar Mg x100/(Mg+Fe)) values vary significantly from ca. 45 to ca. 80 covering the ranges of both nearside FANs and the Mg' gap between FANs and the Mg-suite. A light-gray feldspathic (LG) breccia mainly consists of fragments of anorthosites (An93 anorthosite) more sodic than nearside FANs. The LG lithology also contains an augite-plagioclase clast.

The Dhofar 307 PTS contains magnesian granulitic (GR) clasts similar to the spinel troctolite (ST) clast in Dhofar 489 in mineral chemistry. The grain sizes and mineral chemistry of the GR clasts are the same as those of impact melt (IM) clasts of the Dhofar 309 clasts. Rapid growth features of the IM clasts indicate that these clasts were formed in an impact melt pool. The range of the modal abundances of the minerals and their compositons of three clasts (ST, IM, and GR) obtained from the mineral distribution maps are practically the same and suggest that they were produced by impact events at the floor of a basin on the farside [6].

Among numerous fragments of minerals and lithic clasts of Y-86032, the Mg' values of pyroxene vary from 13.0-86.2, and those of olivine from 4.94-85.5. Broadly, there are two groups of Mg' in olivine compositions, a small Mg-poor group and a Mg-rich group. Pyroxene compositions are densely distributed from Mg' = ~82-55. It is to be noted that pyroxene fragments of Mg' in the range of the Mg-suite rocks are present in Y-86032, but are not common in Dhofar 307 and 489 [3]. The pyroxene fragments in the Dhofar 489 group are less abundant than those of Y-86032, and most of them distribute towards more Mg-rich compositions than Mg' 70. Olivine fragments are more abundant in the Dhofar 489 group, with the most abundant compositions being Mg' 75-76 (Mg An) and 80-85 (ST).

There are several fragments of inverted pigeonite found in the lithic clasts of Y-86032, but not in the Dho 489/307 group. These inverted pigeonites are found in a breccia clast, 31B0, and a clastic matrix in PTS ,83-1 (83P1, 0.27x0.29 mm) of Y-86032. These pyroxene fragments are inverted pigeonite with blebby augite inclusions ($Wo_{4.1\text{-}4.5}En_{72.9\text{-}73.2}$, $Wo_{39.4\text{-}42.3}En_{10.9\text{-}11.9}$, bulk composition: $Ca_{1.7}Mg_{72.2}$, Mg' = 76.7). Such textures have been known in some Mg-suite rocks such as 76255 [7] and also in 62236 [8].

Basaltic clasts in the dark-gray matrix are present in Y-86032, but are not found in the Dhofar 489 group. The crystallization of these basaltic clasts predates the lithification age of the clastic matrix at ca. 3.8 Ga [1].

One unique clast found in Y-86032 is an augite-plagioclase clast (35C1) in the LG lithology. The 35C1 clast (1.4 x 5 mm^2 in size) is moderately brecciated and displays a granular texture composed of augite (~57%) and plagioclase up to ~200 μm in size (~43%) with minor minerals such as ilmenite and chromite. The augite has closely spaced (~several μm) exsolution lamellae (several μm thick) of low-Ca pyroxene. The chemical compositions of the augite and low-Ca pyroxene are $Ca_{41.0}Mg_{35.5}$ and $Ca_{3.0}Mg_{38.4}$, respectively, and the bulk composition is

$Ca_{32.6}Mg_{31.7}$ (Mg' = 47.0). The 35C1 clast occurs in the LG lithology. Because the texture is fine-grained granular and the pyroxene is well equilibrated, the 35C1 clast is not an extrusive rock, but a plutonic rock. The relationship between Ti# (= molar Ti/(Ti+Cr)) and Fe# (= molar Fe/(Fe+Mg)) is similar to that for Low-Ti (LT) basalts (Fig. 7a in [2]), but the horizontal trend of the 35C1 clast can be interpreted as an extension of the LG lithology. The augite-plagioclase clast is more likely as the end product of the LG magma sea.

Discussion:

An estimate of the crystallization age of An97 anorthositic clast Y-86032,133 greater than 4.23 Ga was given in [1]. This clast also experienced severe Ar outgassing at ~3.81 Ga ago. Sm-Nd data for this clast reported in [2] give an imprecisely defined age of 4.26±0.27 Ga. If it was isotopically re-equilibrated with pyroxene from other An97 anorthosites, re-equilibration occurred at 4.31±0.06 Ga ago [2]. However, the whole rock data suggests its derivation from a source distinct from that of the majority of lunar ferroan anorthosites. The Ar-Ar age of Dhofar 489 is 4.23 Ga [3], which is similar to that of Y-86032,133. An97 clast Y-86032,116 has a more ancient Ar-Ar age of ~4.4 Ga [1]. These ancient ages for the meteorite clasts suggest that they may represent times of basin formation on the farside, considering that the meteorites originated from the farside because of low Th and FeO contents [1-3].

The proximity of the An93 anorthosite and 35C1 in Y-86032 suggests that they could have been products of a single local igneous body, with the An93 anorthosite having floated on the top of the magma chamber and with 35C1 having been a late product after fractional crystallization. The 35C1 clast is too Fe-rich to have equilibrated with the Mg-rich mafic minerals in LG, thus it would represent the most evolved end of the hypothetical fractionation sequence.

The mineralogical and geochemical differences between the Y-86032 and Dho 489 groups have been attributed to the locations of the ejection sites. The Y-86032 group sites are much closer to the nearside, because of their higher Th and FAN components. Dhofar 489 may have originated from one of the farside basins in the earliest crust of the Moon with the lowest Th concentration. Likely candidates are old basins with heavily cratered floors.

The low K contents of plagioclase in both the anorthositic and basaltic clasts and generally low incompatible element abundances in all the lithologies in Y-86032 and Dho 489/307 indicate that KREEP was not involved during the formation of the precursor lithologies. All these facts support the idea that both Y-86032 and Dho 489/307 were derived from a region far distant from the PKT. The presence of basaltic clasts, pyroxene fragments similar to Mg-suite rocks without KREEP elements, and more FAN-like anorthosites suggest that Y-86032 may have been derived from a region closer to the nearside than was Dho 489.

The Th map made by the Kaguya GRS group showed the lowest Th zone surrounding SPA, including regions distributed north of the farside equator [9]. This region of the FHT with the lowest Th may represent the earliest anorthositic crust of the Moon, from where the Dhofar 489 group lunar meteorites might have been derived. Among large basins within the region of the lowest Th concentrations of the farside, we found that the Derichlet-Jackson basin is one of the candidates for the ejection site, with abundant craters on its floor, showing that it is one of the oldest craters. Korolev and Mendeleev have flat floors.

The lunar magma ocean (LMO) model initially proposed by Warren and Wasson [10] emphasizes that FANs have very little trapped liquid. Loper and Werner [11] proposed that lunar crustal asymmetries are the result of convective processes acting early in the Moon's history, during the LMO phase, and after synchronous rotation was established. Buoyant anorthositic crystals were transported to the farside by a large-scale circulation, called tilted convection. Crustal thickening near the equator resulted from the modification of tilted convection by the Coriolis force. The selective transport may have resulted in a nearside excess of incompatible elements, leading to the formation of the PKT. The tilt convection model explains also the enrichment of the KREEP incompatible elements in the nearside magma ocean. This hypothesis [6] is consistent with the lowest concentration of Th in a region from north of the Dirichlet-Jackson basin, to Hertzsprung, and to the West of the Orientale basin, measured by the Kaguya GRS [9]

References:

[1] Nyquist L. et al. (2006) *GCA,* 70, 5990-6015. [2] Yamaguchi A. et al. (2010) *GCA, in press*. [3] Takeda H. et al. (2006) *Earth Planet. Sci. Lett.* 247, 171-184. [4] Nishio F. et al. (1987) 12*th* Symp. Antarctic Meteorites, 1-2, NIPR. [5] Korotev R. L. (2006) *GCA*, 70, 5935-5956.. [6] Takeda H. et al. (2010) *LPS* 41, #1572. [7] Takeda H. and Miyamoto M. (1977) *Proc. Lunar Sci. Conf.* **8,** 2617-2626. [8] Takeda H. et al. (1979) *Proc. 10th Lunar Planet. Sci. Conf.* 1095-1107 [9] Kobayasi S. et al. (2010) *LPS* 41, #1795. [10] Warren P. H. and Wasson J. T. (1980) *Proc. Lunar Highland Crust,* 81-99. [11] Loper D. E. and Werner C. L. (2002) *JGR*, 107, 13-1-7.

Quantitative Estimation of Shock Pressure on Martian meteorites of Yamato 000593 and Yamato 000749 Using Cathodoluminescence Spectroscopy.

M. Kayama[1], H. Nishido[1], T. Sekine[2], T. Nakazato[1], A. Gucsik[3, 4] and K. Ninagawa[5], [1]Research Institute of Natural Sciences, Okayama University of Science, 1-1 Ridaicho, Kita-ku, Okayama 700-0005, Japan, [2]Department of Earth and Planetary Systems Science, Hiroshima University, Japan, [3]Max Planck Institute for Chemistry, Department of Geochemistry, Mainz, Germany, [4]Savaria University Center, University of West Hungary, Szombathely, Hungary, [5]Department of Applied Physics, Okayama University of Science, Japan.

Introduction:

Shock pressure induced on meteorites and impactites has been estimated to elucidate a meteorite ejection process based on refractive indices of plagioclase-maskelynite, which has been not available for weakly shocked materials below 15 GPa and micro-size samples. Cathodoluminescence (CL) spectroscopy provides useful information on the existence and distribution of defects and trace elements in micro-size minerals. This technique can be expected to clarify shock pressure effect on minerals in meteorites and impactites. A few CL studies on minerals, especially feldspar in meteorites, however, have been investigated as far. In this study, CL spectral analysis of experimentally shocked sanidine has been conducted to deduce shock pressure on alkali feldspar in the Antarctic meteorite of Yamato 000593 and Yamato 000749 assigned to a Martian origin, which has not been quantitatively estimated up to the present.

Samples and Methods:

Single crystal of sanidine ($Or_{87}Ab_{13}$) from Eifel, Germany was selected as a starting material for shock recovery experiments at 10 to 40 GPa by a propellant gun. Alkali feldspar ($Or_{70}Ab_{27}An_3$) in nakhlite of Yamato 000749 and Yamato 000593 were used for CL spectroscopy and microscopy. They occur as small grains with micro-meter size in the mesostasis. Diaplectic feldspar and glass in shergotty of Dhofar 019, Shergotty, Zagami and NWA 2975 were also employed as reference samples. CL spectra were obtained by a scanning electron microscopy-cathodoluminescence system (SEM-CL), which is comprised of SEM (JEOL: JSM-5410) combined with a grating monochromator (OXFORD: Mono CL2).

Result and Discussion:

Color CL images of unshocked and experimentally shocked sanidine at 10.0 GPa show a red-violet emission similar to alkali feldspar in nakhlite of Yamato 000749 and Yamato 000593, whereas that of sanidine at 20.0 GPa consists of blue CL with vein-shaped texture on red-violet luminescent background. Shocked sanidine at 31.7 and 40.1 GPa, however, exhibit a blue emission in color CL images. Alkali feldspar in shergottite of Dhofar 019, Shergotty, Zagami and NWA 2975 have a blue CL emission with homogeneous distribution of the intensity.

CL spectra of unshocked sanidine, and alkali feldspar in Yamato 000749 and Yamato 000593 consist of emission bands at 420 nm and at 730 nm. Shocked sanidine at 20.0 GPa, however, have blue and red CL emissions at 400 nm and 710 nm, respectively. CL spectra of shocked sanidine above 31.7 GPa show emission bands at 330 and 380 nm which were found in alkali feldspar in the shergottite . The Raman spectroscopy reveals that shock pressure above 31.7 GPa causes partly breaking of the framework structure with dependence on the pressure induced on the sanidine, resulting in a transition from sanidine to diaplectic glass. Emission bands at 380 and 330 nm, therefore, can be identified as a characteristic of CL signals from diaplectic glass. Intensities of these emission bands increase with an increase in shock pressure induced on the sanidine. Shock metamorphism might produces luminescence centers related to these UV-blue CL emissions.

The deconvolution of CL spectra obtained from unshocked and experimentally shocked sanidine, and alkali feldspar in the Martian meteorites can successfully separate the emission bands in UV-blue region into four Gaussian components at 2.82, 2.95, 3.26 and 3.88 eV. The component at 2.95 eV can be detected in all the shocked sanidine, and found in alkali feldspar in the Martian meteorites. Integral intensities of the component at 2.95 eV assigned to shock-induced defect center positively correlate with shock pressure induced on the sanidine, resulting in estimated shock pressures at 7.4 GPa for Yamato 000749 and Yamato 000593, at 26.1 GPa for Dhofar 019, at 31.3 GPa for Shergotty, at 25.5 GPa for Zagami, at 34.4 GPa for NWA 2975.

This CL spectral deconvolution method may allow us to quantitatively estimate shock pressures down to as weak as 5 GPa for micron-size alkali feldspar.

Acknowledgements:

The samples of Yamato 000749 and Yamato 000593 were kindly allocated to this study by NIPR.

Metamorphic and nebular reaction histories of enstatite chondrites: Implications from silicates and sulfides. M. Komatsu[1], T. Fagan[1], H. Watanuki[1], K. Norose[1], K. Matsui[1], and H. Wakai[1], [1]Department of Earth Sciences, Waseda University, Tokyo, Japan 169-8050. (mutsumi@um.u-tokyo.ac.jp)

Introduction:

Enstatite chondrites (ECs) are highly reduced meteorites that mainly consist of Mg-pyroxene (enstatite), metal (kamacite), and Fe-sulfide (troilite). The enstatite contains only very low concentrations of FeO, and the metal phase exhibits relatively high Si abundances. Both characteristics are a consequence of very low O_2 fugacities during condensation and accretion of the EC parent bodies [1].

Minor element variations in silicates in ordinary chondrites have revealed subtle variations in metamorphic grade and some details of element transfers during metamorphism [2]. In contrast, although a general sense for metamorphic grade in enstatite chondrites has been determined [3-7], a detailed understanding of metamorphic petrogenesis remains elusive. Yet, under the low $f(O_2)$ conditions characteristic of ECs, metamorphic reactions are bound to differ from those in other chondrite groups [8].

In this study, we collect multiple analyses of olivine, pyroxene and troilite from a set of ECs to assess variations in composition and approach to equilibrium (uniform compositions) during metamorphism.

Methods:

We investigated 6 polished thin sections of 3 EH3 (ALHA81189, ALH 84170, Sahara 97096), two EH5 (St. Marks, LEW 88180), and one E6 (NWA 974) chondrites. NWA 974 might not come from the EH parent body, thus should not be linked with the EH chondrites to evaluate compositional trends during metamorphism; however, it still can be used for comparison of extent of equilibration in troilite and pyroxene. Elemental maps collected by electron microprobe (JEOL JXA-8900 at Waseda University) were combined with petrographic microscope observations. Elemental X-ray maps were combined as false-color images and used as "base maps" for quantitative electron microprobe analyses of olivine (type 3 only), and pyroxene and troilite (all samples) on grid patterns. On the order of 90 to 200 analyses of each mineral were collected from each sample. Electron backscatter diffraction (EBSD) analysis data were obtained with Oxford EBSD system equipped with S-3400 SEM using HKL Channel5 software (at Waseda University). EBSD data were collected to determine sub-grain boundaries in troilite and compare grain boundaries with variations in minor element composition.

Results and Discussion:

All meteorites studied consist mainly of enstatite with silica, plagioclase, kamacite, troilite, and (Mg,Mn,Fe)S. Olivine is present in ALHA81189, ALH84170, and Sahara 97096 EH3s, but not in the higher petrologic types. Daubreelite, niningerite, oldhamite are present in complex nodules with troilite and/or kamacite in the EH3s; sulfides are more dispersed in St.Marks, LEW88180, and NWA974. Textures show a distinct contrast, with the type 3 chondrites having well-defined chondrules, and the type 5 and 6 chondrites having diffuse chondrule boundaries.

Enstatite is the dominant phase in ECs. The average Fs content in pyroxene decreases with increasing petrologic type (Fig.1). The range of composition becomes smaller in type 5 and 6 than E3s, indicating equilibration during metamorphism.

Troilite in the ECs generally has minor but detectable concentrations of Mn, Cr and Ti compared to the troilite from ordinary chondrites, reflecting low $f(O_2)$ conditions (detection limits: Mn, 0.04; Cr, 0.03; Ti, 0.02 wt%). Chromium ranges up to 4 wt% in individual troilite grains, but Mn and Ti concentrations are below 1 wt%. Nonetheless, concentrations of these elements are systematically higher than in ordinary chondrites and reflect the low $f(O_2)$ formation conditions of ECs. Although wide ranges in composition make it difficult to ascertain whether troilite compositions vary systematically with petrologic type, it is likely the enrichment of Ti has occurred during metamorphism (Fig. 2). Furthermore, troilites from the type 5 and 6 chondrites typically do not have more uniform compositions than in the type 3 chondrites.

Based on detailed X-ray mapping, the ranges in composition of troilite in EH3s may be due to variations between grains of homogeneous composition. In contrast, troilite from St. Marks shows wide variations in composition within grains (Fig.3). EBSD data from St. Marks show that enrichments in Cr and Ti tend to coincide with grain or sub-grain boundaries. Thus, Cr and Ti of troilite in EHs may be roughly analogous with Cr in ferrous olivine of ordinary chondrites [2].

As discussed in many papers [e.g., 3], the reactions which seem to be occurring in enstatite chondrite during metamorphism are as follows;

(1) $2(Fe,Mg)_2SiO_4 \rightarrow 2MgSiO_3 + 2Fe_{metal} + O_2$
(2) $FeSiO_3 + 3C \rightarrow Fe_{metal} + Si_{metal} + 3CO$
(3) $Ni_3P_{shreib} + 3Fe_{metal} \rightarrow Fe_3P_{shreib} + 3Ni_{metal}$
(4) $Fe_{metal} + H_2S \rightarrow FeS_{cubic\ sulfide} + H_2$

The loss of Fe from pyroxene would reflect the reaction (2). Our previous study shows the presence of high-FeO silicates which looks opaque in transmitted light. They contain tiny inclusions of Fe metal (Fig.4). Evidence for the increase of Ti-content in troilite is less straight-forward, and the

subject of ongoing study.

In any case, even though EC pyroxene and troilite experienced similar metamorphic thermal histories, approaches to equilibrium compositions in these mineral groups do not match. Uniformity of Fs-content in pyroxene probably represents a near-peak metamorphic temperature condition, whereas variations in minor elements (Mn, Cr, Ti) in troilite in type 5 and 6 E chondrites reflect post-peak partial re-equilibration. In contrast, wide ranges in minor element composition of troilite of type 3 ECs reflect variations in $f(O_2)$ [and $f(S_2)$?] in different regions of the solar nebula where chondrites components formed (Fig.5).

References: [1] Brearly and Jones (1998), *Reviews in mineralogy* 36, 398 [2] Grossman J. and Brearly. A. J. (2005) *MaPS 40,* 87-122. [3] Zhang et al. (1995) *JGR* 100, 9417-9438. [4] Weisberg M.K. et al. (2009) *LPS* XL, #1886. [5] Hicks T. et al., (2000) *LPS* XXXI, #1491. [6] Kimura M. et al. (2005) *MaPS* 40, 855-868. [7] Bendersky C. et al., (2007) *LPS* XXXVIII #2077. [8] El Goresy A., et al. (1988) *Proc. NIPR Symp. Ant. Metorit.* 1, 65-101.

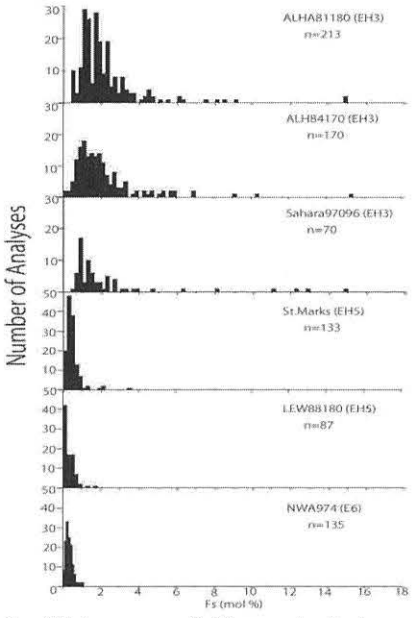

Fig.1. Histogram of Fs content in pyroxene in enstatite chondrites. NWA 974 may be part of a different metamorphic sequence .

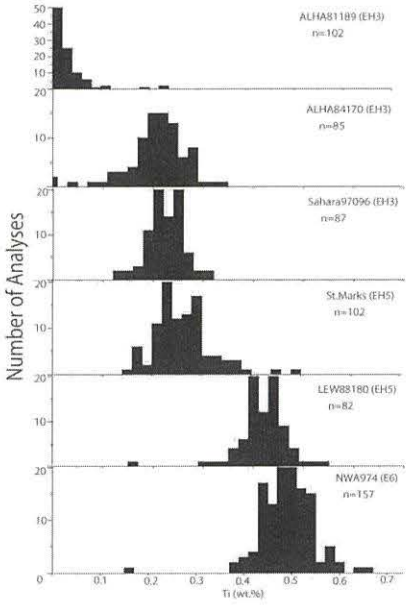

Fig.2. Histogram of Ti content in troilite in enstatite chondrites. NWA 974 may be part of a different metamorphic sequence.

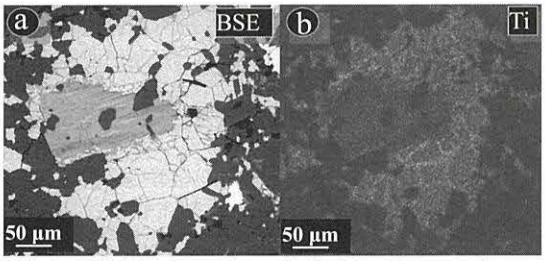

Fig.3. BSE image (a) and Cr-Kα elemental map of troilite grain #3 from St. Marks. Concentration of Ti (and Cr) along the cracks and grain boundaries are observed.

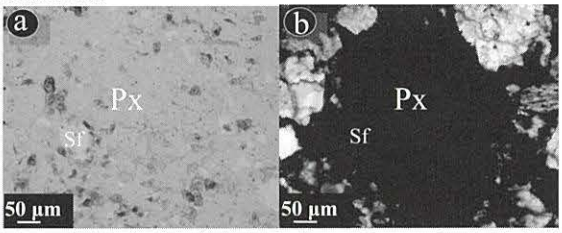

Fig.4. Photomicrobraphs of pyroxene from ALHA. Some FeO-rich silicates (a: reflected light) look opaque in transmitted light (b), implying they experienced reduction.

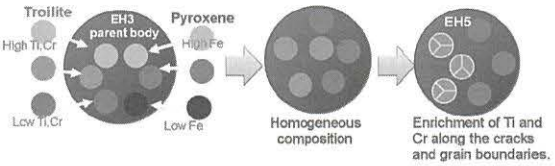

Fig.5. Schematic pictures of the EH parent body. Near peak metamorphism, troilite and pyroxene become homogeneous. Post-peak re-equilibration of troilite continued resulting in the enrichment of Ti and Cr along the cracks and grain boundaries.

Twenty-Eight Years of Lunar Meteorites. R. L. Korotev, Department of Earth & Planetary Sciences and McDonnell Center for the Space Sciences, C/B 1169, Washington University, Saint Louis, Missouri, USA (korotev@wustl.edu)

The first meteorite from the Moon was not recognized until 1982, nine years after the last Apollo lunar mission. Since then, a remarkable 66 more have been found and recognized (Fig. 1). Initially, lunar meteorites were found exclusively in Antarctica by organized expeditions sponsored by the Japanese and U.S. governments. Although the rate of discovery in Antarctica has remained relatively constant, about two meteorites every three years, new finds have been dominated by discoveries by private collectors in the deserts of northern Africa and Oman over the past 10 years (Fig. 1).

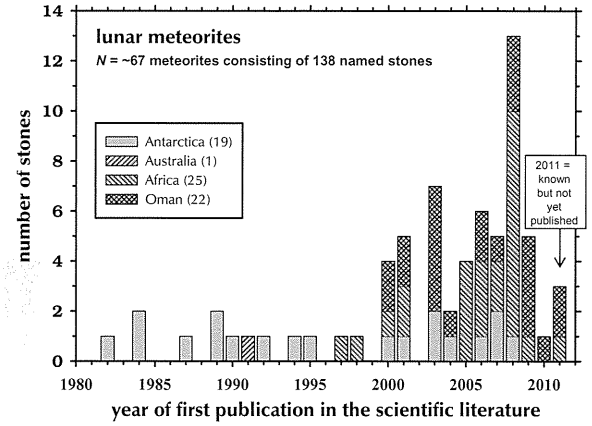

Figure 1. Lunar meteorite discovery as a function of time. Some paired stones were found in different years (e.g., Yamato 82192 and 86032); this plot indicates the year of announcement of the first stone.

Size. Lunar meteorites tend to be small compared, for example, to ordinary chondrites. Those from Antarctica are much smaller, on average, than those from hot deserts (Fig. 2). Because of differences in field conditions, it is expected that searches in Antarctica will recover a larger fraction of small stones that might be overlooked elsewhere. However, the five largest lunar meteorites, all >2 kg in mass, have been found in hot deserts whereas none this large have been found in Antarctica. The largest meteorite from Antarctica is LAP 02005 (1.23 kg) and 5 smaller paired stones (1.93 kg, total).

Pairings. Cases of terrestrial pairing are usually evident from field relationships and similarities in composition, mineralogy, and texture. There are some ambiguities among the meteorites from hot deserts, however, because find locations are not always reported. As more meteorites are found, likely launch-pairings are increasingly found. Among Antarctic meteorites, MIL 07006 and Y-791197 are compositionally and texturally similar [1] as are NWA 4884 and QUE 94281 [2]. No comparative petrographic work has been done on these meteorites, however. The largest basaltic lunar meteorite from the hot deserts, NWA 4734 (1.37 kg), is an apparent launch pair of the LAP 02005 [1].

Rock Types. Most lunar meteorites are brecias. Ten are mare basalts, but three of these are actually breccias with large clasts of basalt. Most brecciated lunar meteorites are regolith or fragmental breccias formed by shock-compression of fine-grained material. These meteorites are essentially sedimentary rocks. A few are impact-melt breccias (igneous) or granulitic breccias (metamorphic) [3].

Although lunar meteorite all are composed of the same few minerals, most lunar meteorites are, in detail, different from rocks of the Apollo collection. Some are strikingly different. The differences reflect the geologic complexity of the highly differentiated Moon, both laterally and with depth. They also reflect that the six Apollo landing sites were all in or near the high-Th geochemical anomaly known as the PKT (Procellarum KREEP Terrane) whereas the meteorites come from randomly distributed locations over the entire globe [2,3].

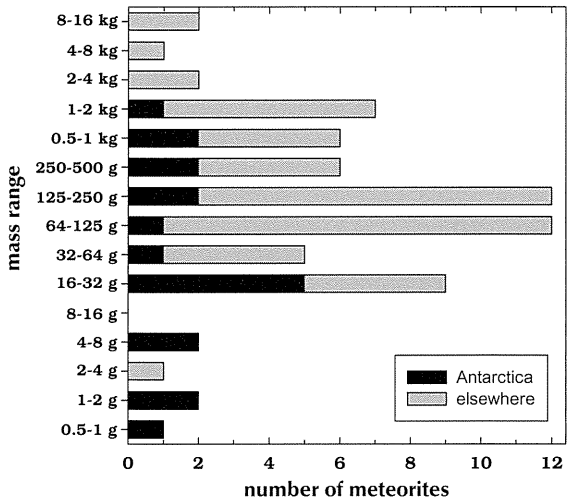

Figure 2. Mass distribution for lunar meteorites. The geometric mean mass is about 144 g (all known stones of pairs). For lunar meteorites from Antarctica, the geometric mean is only 42 g.

Bulk Composition. Compositional variation among lunar meteorites far exceeds that of meteorites from any other parent body. FeO concentrations range over a factor of 8 and Th concentrations over a factor of 400 (Fig. 3). Half the meteorites are highly feldspathic (3–7% FeO) and have low concentrations of incompatible elements like Th. These meteorites originate from the vast expanse of FHT (Feldspathic Highlands Terrane), most of which is on the farside. Remarkably, the whole-rock Mg' [mole % Mg/(Mg+Fe)] ranges from 57 to 80 and averages considerably greater than ferroan anorthosites of the Apollo collection (Fig. 4). The meteorites reveal that magnesian anorthosite prevails in some regions of the highlands [4–6].

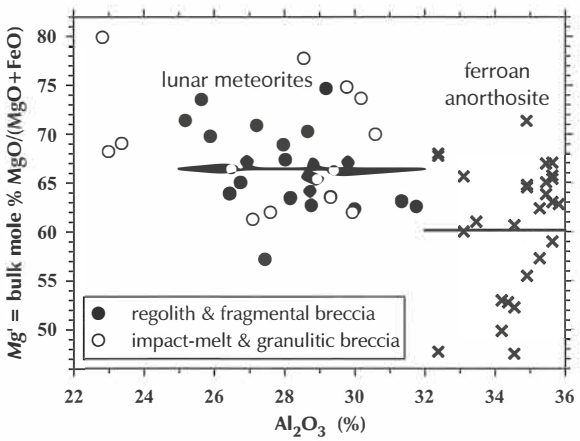

Figure 4. Comparison of *Mg´* between pristine ferroan anorthosite (×) [14] and feldspathic lunar meteorites (circle). Horizontal lines are means.

None of the basaltic lunar meteorites are, in detail, like any basalts of the Apollo collection, although LAP 02005 and NWA 4734 bear some resemblance to Apollo 12 and 15 basalts [7–9]. Some basaltic lunar meteorites are very different from any Apollo basalt, e.g., Asuka 881757, MIL 05035, Yamato 793169, and MET 01210 (all likely launch pairs [10]), Kalahari 009 [11], the NWA 773 clan [12], and NWA 4898 [13].

Four lunar meteorite have >3.5 ppm Th, consistent with derivation from the PKT: SaU 169, Dhofar 1442, NWA 4472/4485, and Calcalong Creek. Calcalong Creek, however, is one of seven meteorites having certain compositional characteristics (high Th/Sm, low Eu/Sm) that are inconsistent with any known FHT-PKT-basalt mixture. Some or all of these meteorites, which include Y-983885, may be from locations distant from the PKT, possibly the South Pole-Aitken basin, despite their elevated concentrations of Th [2].

The find rate of meteorites from hot deserts is decreasing so Antarctica will remain an important source of new lunar meteorites.

References: [1] Korotev R. L. et al. (2009) *LPS XL*, #1137. [2] Korotev R. L. et al. (2009) *M&PS 44,* 1287–1322. [3] Korotev R. L. (2005) *Chemie der Erde 65*, 297–346. [4] Korotev R. L. et al. (2003) *GCA 67,* 4895–4923. [5] Takeda H. et al. (2006) *Earth Planet. Sci. Lett. 247*, 171–184. [6] Kuehner S. M. et al. (2010) *LPS XLI*, #1552. [7] Anand M. et al. (2006) *GCA 70*, 246–264. [8] Day J. M. D. et al. (2006) *GCA 70*, 1581–1600. [9] Zeigler R. A. et al. (2005) *M&PS 40*, 1073–1102. [10] Arai T. (2010) *GCA 74*, 2231–2248. [11] Sokol A. et al. (2008) *GCA 72*, 4845–4873. [12] Zeigler R. A. (2007) *LPS XXXVIII*, #2109. [13] Greshake A. et al. (2008) *LPS XXXIX*, #1631. [14] Warren P. H. (1993) *Am. Mineral.* 78, 360–376.

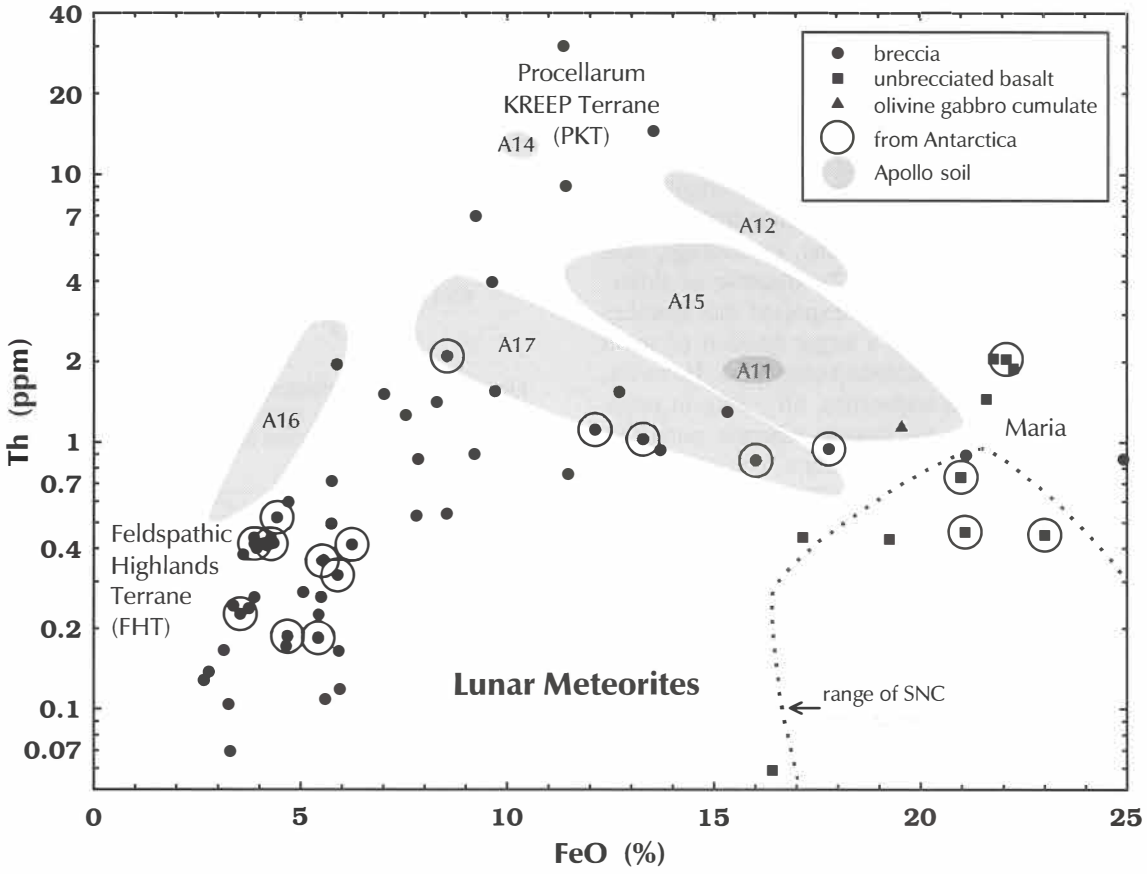

Figure 3. Lunar meteorites in FeO-Th space and comparison to Apollo soils and SNC meteorites (updated from [3,4]. Each point represents a meteorite (all stones of pairs) except that for dilithologic and trilithologic meteorites two or three points representing each lithology is plotted. A11 = range Apollo 11 soil, etc.

Trajectory and Speciality of Fireball-Meteorite "2010.02.28 Cassovia" from Security Cameras and from Reports of Local Inhabitants. Prof. DR. I. Kubovics[1], M.A. Turcsányi[2] and P.G. Vizi[3], [1]Department of Petrology and Geochemistry, Eötvös University, drkubovics@t-online.hu, [2]Kodolányi János University of Applied Sciences anastazia.maria@hotmail.co.jp, [3]M. Zrínyi National Defense University PhD Inst. in Mil. Technology vizip@rmki.kfki.hu

Preface:

We want to show our investigations about the 2010.02.28. 22:24:44 UTC fireball event which named last Cassovia Meteorite. We organized our own mission and expeditions to calculate and find the trajectory and pieces of this fireball-meteorite event.

The Event:

February 28, 2010 was a cloudy evening above Central-Europe and therefore original meteor cameras were turned off. At 22:24:44 UTC a fireball meteor arrived and was recorded only accidentally by security cameras.

"Meteor finder" security cameras:

In case of meteorite finder sky oriented cameras there are available a correct calibration. This situation is essential, because there was not any pre-calibration. On the internet became available two free and researchable records. [1][2] We have one additional reserved video from one of our colleague's cousin.

Getting data from security cameras:

If we want to use those available records, security cameras must be calibrated after event to get and to reveal the trajectory and orbit. First we looked after the position of cameras on the Internet and pinpointed on the Google Earth and only after this action we travelled to the available cameras and we measured the position by GPS. We repeated the measuring several times and calculated the average. We chose some special object in the field of original security pictures – for example lamp posts, churches, valleys between hills – and measured and pinpointed its position in Google Earth.

During this method we tried to make some additional long exposure pictures near from cameras during starry nights. After that we identified some stars and signed them in a planetarium program namely in Starry Night Backyard. We collected all of positions, stars, objects, etc.

Properties of cameras:

On the other hand we tried to collect data of cameras like type and from there we found technical data on the Internet. If we know the size of the CCD, focus distance and the angle from those data we can calculate back the projecting lines start back from the focus point of cameras. We have the serials of positions of the image-points of the fireball-meteor on the screen. In addition we have them in different times frame by frame, see later.

Two points set one line and two lines set a plain. We have minimum two well positioned cameras (and one additional to check the result).

Intersection of two planes is a straight line. In our event this is the estimated orbit of our fireball-meteor. [3]

The end of those lines pinpoints nearly the end position of the meteor where we can find the possible

pieces of the meteorite. The meteorite was drag slowed at the end of the orbit and pieces were fallen near perpendicularly. This position was near to

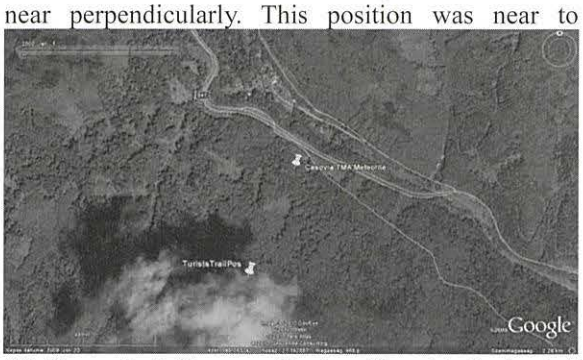

[3] Cassovia (Kassa – Kosice, Slovakia) about 5 kilometers from the border of this town at the North-West direction.

Determination of the correct time:

In case of a simple security camera system there isn't available much better timing. After the event we can use a radio synchronized clock or a GPS to measure the actual time difference between the real time and the system's time. This value of the time is not enough to find the correct time of the event. We must decide whether to hasten or slow the systems clock (first derivative) mainly and if it is necessary we need to know the acceleration of this (second derivative). In case of modern security systems one additional time measuring is mainly enough to calculate the acceptable time. If there is any suspicious hasten or slow then must make a third measuring and to use it during time calculations.

When we have correct timing then we can put scheduling into lines projecting from focus of the [1] camera and we get not only the orbit with serials of explosions but we can get them exactly with times of positions.

Checking and correcting the trajectory of meteor by reports of local inhabitants:

When we got an estimated trajectory we started to collect more information and to collect some pieces of the expected meteorites. During this expedition we collect some significant unusual observations.

We make several (near 40 and from those 20 recorded) interviews for example in Kuntapolca / Kunová Teplica, Slovakia, at Mayor's Office and there told us "I heard a noise as if something had been fallen in hot water for 10 minutes with hissing sound."

Special ice formations:

In this village we found a small lake with special ice formations on its surface. We know the dendrite-like features in the ice are common place in frozen ponds; they may be related to gas bubbling

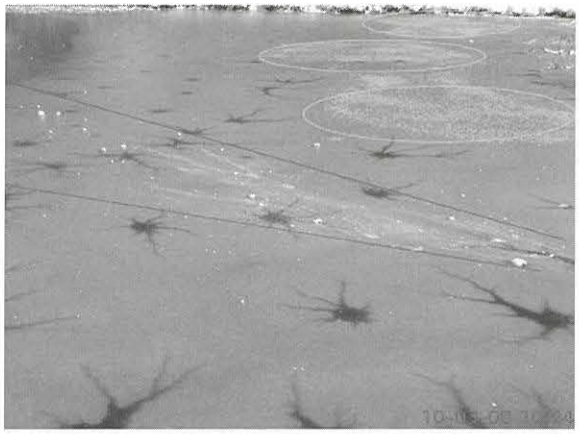

out of sediment. But local inhabitants and personally the Mayor never saw similar formations before.

According to our opinion those are only coincident events or features but maybe significant observations.

The meteorit piece:

During our missions we collected several suspicious rocks. One of them was a meteorite according to inspection of Prof. DR. Imre KUBOVICS. He identified the type of the meteorite. According to picture this is a H5 meteorite.

Picture left was made with one Nikol, right with

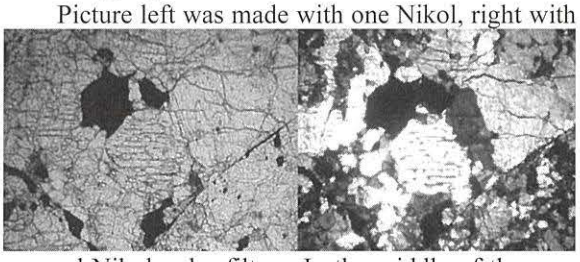

crossed Nikol polar filters. In the middle of the area you can see a barred chondrule, somewhat blurred edges.

We gave a temporary attached name for this piece from the initials (Hungarian initials order) of the finder: 2010 Cassovia 'TMA'

Conclusion:

We hope that our investigation was mainly successful. We want to expand our mission to find other pieces.

We can tell, the origin of 2010.02.28 Cassovia 'TMA' meteorite according to the microscopic observation is estimated from the asteroid belt.

References:

[1] RTL Klub (2010) Meteor Strike over Hungary 02/28/ 2010 http://www.youtube.com/watch?v=tPPDjLYMh1M&NR=1

[2] D.Fazzi and G. Vass (2010) Meteor Örkényről http://www.youtube.com/watch?v=mvJkhiUUAT8

[3] Google Earth (2010) earth.google.com

The Production Rate for ^{26}Al estimated by Major Elemental Compositions in Meteorites.

H. Kusuno[1], T. Fukuoka[1], H Kojima[2] and H. Matsuzaki[3], [1]Graduate school of Geo-environmental Science, Rissho University, Kumagaya 360-0194, Japan (H. Kusuno: 089w00002@ris.ac.jp). [2]Antarctic Meteorites Research Center, National Institute of Polar Research, Tachikawa, Tokyo 190-8518, Japan. [3]Department of Nuclear Engineering and Management, School of Engineering, the University of Tokyo, Hongo, Tokyo 113-0032, Japan.

Introduction:

The terrestrial ages of Antarctic meteorites can be applied to studies such as the frequency of meteorite fall, mechanism of accumulation of meteorites and the age of ice, the oldest age of which is 800 kyr. ^{26}Al ($T_{1/2}$ = 7.05 x 10^5 y) is a useful tool for dating of terrestrial ages of meteorites.

We need the production rates of cosmogenic nuclides (^{10}Be, ^{14}C, ^{26}Al and so on) in meteorites in space to determine the terrestrial ages of meteorites. The production rates of cosmogenic nuclides in meteorites were estimated by major elemental compositions of meteorites [1, 2] or cosmic-ray interactions by particle models [3, 4]. However the ^{26}Al values of falls howardite and eucrite samples estimated by those references [1, 2, 3, 4] are higher than measured values of those samples.

Here we present a new production rate of ^{26}Al that is applicable for not only chondrites but also howardites and eucrites. We estimated production rate of ^{26}Al by major elemental compositions in meteorites based on the correlation between ^{26}Al contents and elemental compositions in nineteen meteorite samples fallen recently (one howardite, six eucrites, four diogenites and eight chondrites).

Measurements of ^{26}Al contents and elemental compositions in meteorites:

^{26}Al contents in meteorite samples are measured by AMS (accelerator mass spectrometry) analysis. The sample preparation of meteorite samples for AMS analysis is described in [6]. AMS measurements were carried out at MALT (Micro Analysis Laboratory, the University of Tokyo). Major elemental compositions of meteorite samples were measured by INAA (instrumental nuclear activation analysis) for Na, Mg, Al, Ca, Ti and Mn and by atomic absorption spectrometry for Fe. The neutron irradiation for INAA was carried out at JAEA (Japan Atomic Energy Agency). Si contents in those samples were calculated as SiO_2 % = 100 - (Na_2O, MgO, Al_2O_3, CaO, TiO_2, MnO, FeO).

Correlation between ^{26}Al contents and major elemental compositions in meteorites:

We checked the correlation between ^{26}Al contents and major elemental compositions in nineteen meteorite samples fallen recently, and we found that there were good correlation between ^{26}Al contents and sum of Si, Al and Ca contents (Fig. 1). The ^{26}Al, Si, Al and Ca contents and sum of Si, Al and Ca of those samples are as follows; the howardite sample, 71 dpm/kg ^{26}Al, 24 % Si, 4.25 % Al, 4.8 % Ca and (Si + Al + Ca) = 33; the six eucrite samples, 80 - 96 dpm/kg ^{26}Al, 24 – 25 % Si, 5.53 – 6.74 % Al, 6.4 – 7.8 % Ca and (Si + Al + Ca) = 36 - 39; the four diogenite samples, 70 to 78 dpm/kg ^{26}Al, 25 – 27 % Si, 0.38 – 2.23 % Al, 0.6 – 1.3 % Ca and (Si + Al + Ca) = 27 - 30; the eleven chondrites samples, 51 - 71 dpm/kg ^{26}Al, 16 -26 % Si, 0.91 – 2.10 % Al, 1.2 – 2.1 % Ca and (Si + Al + Ca) = 19 – 29 (Table 1). ^{26}Al contents in those samples tended to increase in proportion to the Al and Si contents. This tendency agrees with what Al and Si are main target for production of ^{26}Al through the nuclear reaction with cosmic-ray in space [4, 5].

The correlation between ^{26}Al contents and Si, Al and Ca in the nineteen meteorite samples fallen recently were expressed by the following equation; ^{26}Al dpm/kg = 1.8 Si % + 1.8 Al % + 1.8 Ca % +21 (1). The amount of ^{26}Al produced from Si and Al estimated by (1) was smaller than that estimated by [1], [2] and [4]. Although the amount of ^{26}Al produced from Ca is ten times smaller than that from Al and Si [5], the production rate of ^{26}Al from Ca in (1) is same as that of Al and Si.

Estimating production rates of ^{26}Al:

We estimated ^{26}Al values for the twelve recently fallen HED meteorite samples (one howardite, two eucrites and eight diogenites) using equation of (1) in this work and production rates of three references [1, 2, 4]. The elemental compositions of those samples were from [7] and [8]. The measured ^{26}Al contents were from [2], [8], [9] and [10]. ^{26}Al values were estimated by production rates of (1) in this work, [1], [2] and [4] and those values agreed with measured values of ^{26}Al within 1 – 25% (average 12 %), (1); 2 – 46 % (average 29 %), [1]; 3 – 58 % (average 26 %), [2]; and 4 – 25 % (average 16 %), [4], respectively.

Our estimated values of ^{26}Al showed best agreement with measured ^{26}Al values. We can use the equation (1) to estimate the ^{26}Al values for both HEDs and chondrites. The estimated values of ^{26}Al produced from Ca by the equation (1) may be reconsidered to be smaller than Al and Si. Because there is a significant difference in mass between ^{26}Al and Ca to produce ^{26}Al from Ca.

References:

[1] Cressy P. J. Jr. et al. (1971) *GCA,* 35, 1283–1296. [2] Hampel W. et al. (1980) *GCA,* 44, 539–547. [3] Masarik J. and Reedy R. C. (1994) *GCA,* 58, 5307–5317. [4] Leya I. and Masarik J. (2009) *MAPS,* 44, 1061–1086. [5] Leya I. et al. (2000) *MAPS,* 35, 259–286. [6] Kusuno H. et al. (2007) *31st Antarct. Meteorit.,* abstract, 43-44. [7] Fukuoka T. et al. (1977) *Proc. LSC 8th,* 187–210. [8] Welten K. C. et al. (1997) *MAPS,* 32, 891–902. [9] Cressy P. J. Jr. (1976) *NASA TN D-8241,* 1–28. [10] Muntean R. A. (1979) *Ph. D. Thesis. Univ. Tennessee.*

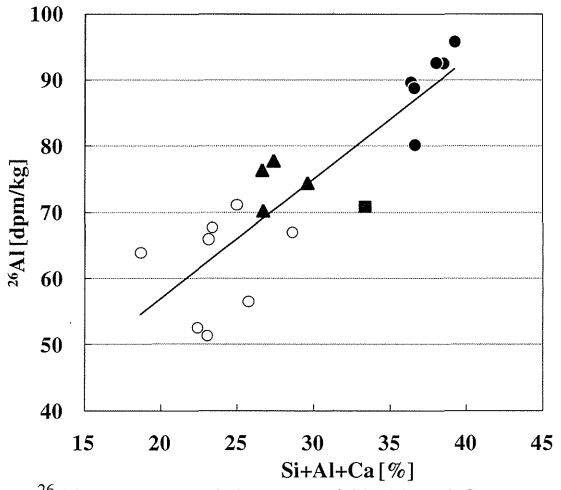

Fig. 1. The correlation between ^{26}Al contents and the sum of Si, Al and Ca contents in nineteen meteorites fallen recently (eleven HEDs and eight chondrites). The horizontal axis is sum of Si, Al and Ca contents in each meteorite samples. Si, Al and Ca contents were measured by INAA. The vertical axis is ^{26}Al contents measured by AMS analysis. The black square shows a fall howardite, the black circles show six recently fallen eucrites, the black triangles show four recently fallen diogenites and the white circles show eight chondrites. The ^{26}Al contents in nineteen meteorites fallen recently showed good correlation with sum of Si, Al and Ca contents. The line on the graph was calculated by least square method. The line is expressed by the following equation: $^{26}Al = 1.8\ (Si + Al + Ca) + 21$ with correlation coefficient $R^2 = 0.75$.

Table 1. The ^{26}Al, Si, Al and Ca contents and sum of Si, Al and Ca contents in nineteen meteorite samples fallen recently (one howardite, six eucrites, four diogenites and eight chondrites).

	^{26}Al dpm/kg	Si %	Al %	Ca %	Si + Al + Ca
howardite	71	24	4.25	4.8	33
eucrite	80 - 96	24 - 25	5.53 - 6.74	6.4 - 7.8	36 - 39
diogenite	70 - 78	25 - 27	0.38 - 2.23	0.6 - 1.3	27 - 30
chondrite	51 - 71	16 - 26	0.91 - 2.10	1.2 - 2.1	19 - 29

Table 2. The equations to estimate ^{26}Al production rates by major elemental compositions.

reference	the equations
This work	$^{26}Al = 1.8Al + 1.8\ Si + 1.8Ca + 21$
Cressy (1971)	$^{26}Al = 11.3Al + 2.4\ Si + 0.28Mg + 0.24Ca + 1.33S + 0.022(Fe + Ni)$
Hampel (1980)	$^{26}Al = 4.92Al + 2.74Si + 0.42Mg + 0.24Ca + 1.33S + 0.03Fe$
Leya (2009)	$^{26}Al = 5.46Al + 3.20Si + 0.037Fe$

Genesis of the Primary Metallic and Secondary Olivine Matrix of Chondrites.

A. A. Marakushev[1], N. G. Zinovieva[2], and L. B. Granovsky[2], [1]Institute of Experimental Mineralogy, Russian Academy of Sciences, ul. Institutskaya 4, Chernogolovka, Moscow oblast, 142432 Russia (belova@iem.ac.ru), [2]Department of Petrology, Geological Faculty, Moscow State University, Leninskie Gory, Moscow 119992, Russia (zinov@geol.msu.ru).

Chondrites are known to originate from the Asteroid Belt, which consists of fragments of chondritic (unlayered) iron-stony planets [1]. Similar to layered terrestrial planets, they were formed and evolved as the liquid iron-silicate cores of nearsolar giant planets analogous to Jupiter, but in contrast to the latter, they have lost their vast fluid envelopes under the effect of the Sun, so that their cores were transformed into individual chondritic planets. These planets have eventually explosively broke up and gave rise to asteroids. Evidence of this planetary evolutionary stage is provided by chondrites. The beginning of their evolution was marked by differentiation into enstatite and forsterite chondrules and Ni-Fe matrix due to the onset of liquid immiscibility under the pressure of the fluid envelopes of the giant parent planets.

Traces of this pressure are tiny (<10 nm) diamond grains in association with moissanite (SiC) in the metallic matrix of chondrites. The diamond abounds in fluid inclusions and has a ratio of the 136/134 xenon isotopes of 1.04, i.e., analogous to this ratio in the Jupiter atmosphere [2]. The correlation of the average compositions of chondrites, primary chondrules, and metallic matrix defines the major types of chondrites (figure), with which the evolution of chondritic magmatism started. This "initial" state is preserved only in unequilibrated chondrites, which were produced when their parent planets rapidly lost their fluid envelopes, and hence, their early protoplanetary and final planetary evolutionary phases were combined. An example is provided by the Hammadah al Hamra 237 chondrite [3], whose magnesian chondrules are submerged in a metallic matrix. The porphyritic texture of the latter is defined by zonal Ni-Fe grains (5-10 wt % Ni) in a kamacite groundmass. All enstatite chondrites were formed under similar conditions, and their chondrules underwent only autobrecciation due to the explosive separation of fluids from the metallic matrix. A more common situation was, however, the slow outgassing of the parent planets of chondrites with the decrease in both the total fluid pressure and the H_2/H_2O ratio in fluids because of preferable hydrogen loss. This stimulated chondrule-matrix oxidation reactions, as in enstatite chondrite types: $MgSiO_3 + Fe + H_2O = MgFeSiO_4 + H_2$. With progress of the reaction (shift to its right-hand side), the metal matrix in the series of ordinary chondrites was replaced by an olivine matrix, and enstatite chondrules gave way to olivine. The main types of ordinary chondrites are originated in order of their increasing Fe mole fraction Fe·× 100/(Mg+Fe) (numerals in parentheses): HH(10)- H(20)- L(25)- LL(30), according to the reaction $0.75Mg_{1.6}Fe_{0.4}SiO_4 + 0.25Mg_{0.8}Fe_{0.2}SiO_3 + 0.35Fe_{0.93}Ni_{0.07} + 0.25H_2O = Mg_{1.4}Fe_{0.6}SiO_4 + 0.35Fe_{0.75}Ni_{0.25} + 0.25H_2$. This reaction corresponds to the well-

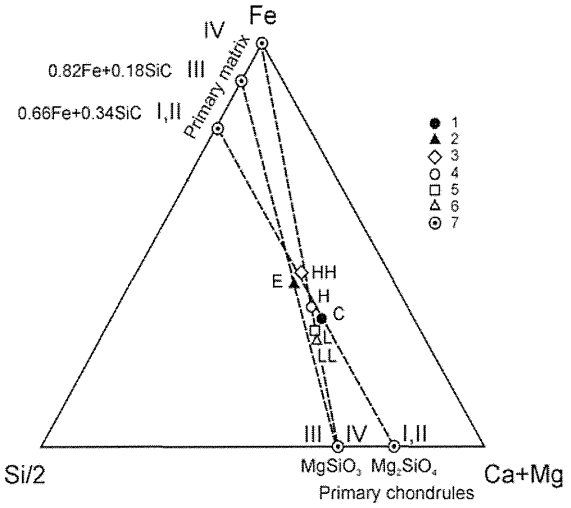

Figure. Genetic types of chondrites (I-IV) determined by the correlation of their average compositions. 1-6 – chondrites: 1 – carbonaceous C, 2 – enstatite E, 3-6 – ordinary (3 - HH, 4 - H, 5 - L, 6 - LL), 7 – their metallic matrix and primary chondrules

known Pryor rule. The composition of chondrules in predominant equilibrium

chondrites is correlated with the composition of olivine in the metallic matrix. In contrast to them, the metallic matrix of unequilibrated chondrites is replaced by a ferrous olivine matrix at the reservation of primary forsterite chondrules. The primary chondrules of carbonaceous chondrites consist of forsterite in equilibrium with metallic matrix rich in Si (figure). Such relations were reached in very large parent planets under an extremely high hydrogen pressure, which destabilized enstatite chondrules: $2MgSiO_3 + Fe + 2H_2 = Mg_2SiO_4 + (Fe + Si) + 2H_2O$ or $2MgSiO_3 + Fe + 3H_2 + CO = Mg_2SiO_4 + (Fe + SiC) + 3H_2O$. The chondrules thus generated had an extremely light oxygen isotopic composition (rich in ^{16}O). Fragments of calcic-aluminous chondrules are referred to as refractory inclusions.

The oxygen isotopic composition of carbonaceous chondrites became heavier ($^{16}O \rightarrow {}^{17}O + {}^{18}O$) as their parent planets lost fluid envelopes according to development of the hydration reactions like $Mg_2SiO_4 + (2Fe + SiC) + 4H_2O = 2MgFeSiO_4 + C + 4H_2$. Their shift to the right-hand sides was associated, first of all, with the replacement of their primary metallic matrix by an olivine one. If the latter contained preserved primary forsterite chondrules and their fragments, forsterite-olivine chondrites were formed; if the primary forsterite chondrules were replaced practically completely, olivine chondrites were generated. These olivine chondrites were found in normal forsterite-olivine chondrites in the form of so-called dark inclusions, which sometimes have angular (clastic) morphologies. According to [4], they have an heavy oxygen isotopic composition (numerals in parentheses), for example Allende, whose $\delta^{17}O$=-2.73‰ (1.08) and $\delta^{18}O$=1.51 ‰ (5.75), providing an example of isotopic shift toward the oxygen isotopic composition of carbonaceous chondrite water ($\delta^{17}O$=9.2‰, $\delta^{18}O$=15.9‰).

Hence, olivine chondrites are the highest evolutionary phase of chondritic magmatism, which corresponded to the extreme shift of the reaction discussed above toward its right-hand side. These chondrites were produced in the peripheral parts of chondritic planets that were affected by fluids for a much longer time than the internal portions of the planets, whose evolution terminated at the forsterite-olivine evolutionary phase. During the final phase, olivine chondrites formed the consolidated crusts of planets. The latter were intruded and trapped in the form of dark inclusions by forsterite-olivine chondritic melts coming from the inner parts of the planets. Evidence of the liquid state of their olivine matrix is provided by its chill textures, which are clearly seen, for example, in the Allende meteorite. Its secondary matrix consists of tiny platy (with elongated cross-sections) laths of olivine. Petrographically, it is analogous to spinifex textures typical of chill textures in ultramafic magmas. Their liquid state is retained in the presence of abundant volatiles, whose loss brings about chill textures. The chill texture of the Allende meteorite was caused by the transition from the protoplanetary to planetary evolution phases of the chondritic planets.

Acknowledgments: This work was supported by the Program "Support of Scientific Schools, grant 5367.2008.05".

References: [1] Marakushev A. A. et al. (2003) *Kosmicheskaya Petrologiya,* M: Nauka-press, p. 387.
[2] Manuel O. and Katragada A. (2003) *Proc. ACM 2002*, 787-790.
[3] Krot A. N. et al. (2001) *Science, 291*, 1776-1779.
[4] Clayton R. N. and Mayeda T. K. (1999) *GCA, 63,* 2089–2104.

Detection of Primordial Argon-rich Noble Gas in the Parnallee LL 3.6 Chondrite by Laser Microprobe Ablation Method. S. Matsuda[1], D. Nakashima[2], and K. Nagao[1], [1]Geochemical Research Center, Graduate School of Science, University of Tokyo, Bunkyo-ku, Tokyo 113-0033, Japan. E-mail: matsuda@eqchem.s.u-tokyo.ac.jp. [2]Department of Geoscience, University of Wisconsin-Madison, USA.

Introduction:

Trapped noble gases in primitive meteorites are expected to constrain the formation process of planetesimals in the early solar system. In the pristine solar nebular, the most abundant and widespread primordial component is Q-gas, which is contained in the carbonaceous phase Q [1]. In addition to the Q-gas, there are many minor components of primordial noble gases such as Ar-rich gas. This component was discovered for the first time in enstatite chondrites classified as petrologic types of 4 to 6 [2, 3]. $^{36}Ar/^{132}Xe$ and $^{84}Kr/^{132}Xe$ ratios of Ar-rich gas are variable between those of Q ($^{36}Ar/^{132}Xe$ = 76, $^{84}Kr/^{132}Xe$ = 0.81 [4]) and the solar wind ($^{36}Ar/^{132}Xe$ = 25000, $^{84}Kr/^{132}Xe$ = 10 [5]), which is in some cases called as subsolar component. Then, subsolar gas was found in chondrules of Yamato-79179 enstatite chondrite [6] and fine-grained dark inclusion of Ningqiang carbonaceous chondrite [7]. The clarification of the relationship between Q-gas and Ar-rich gas in meteorites contributes to understand the accretion and evolution processes of those parent bodies.

We performed laser microprobe noble gas analysis on chondrules and matrix of the Parnallee LL 3.6 chondrite. Trapped noble gases in matrix are mixture of Q-gas and Ar-rich gas. We discuss about the formation history of the parent body of the Parnallee chondrite.

Laser microprobe noble gas analysis:

A thick section with polished surface (~ 200 μm thick) was made from a chip of the Parnallee chondrite. The surface was observed with a scanning electron microscope (SEM - EDS) so as to examine chondrule texture and major element compositions. Noble gases were extracted by heating a small portion with a Nd-YAG laser (50 μm in beam diameter) from five chondrules (named as Ch1 - Ch5) and the matrix. Noble gases released from 5 – 9 laser pits produced in narrow area were measured as one analysis site. Weights of fused material for the one analysis are estimated to be 6 - 11μg by assuming the densities of chondrule and matrix as 3.2 and 2.8 g/cm^3, respectively. Extracted noble gases were analyzed with a modified VG5400 (MS-II) mass spectrometer at the University of Tokyo. We analyzed 2 - 5 sites within individual chondrule depending on their sizes. Extraction and isotopic analysis of noble gases in the matrix were conducted in 10 sites.

Results and discussion:

Types of chondrules measured in this work consist of two ferroan porphyritic (Ch2 and Ch3), two barred pyroxene (magnesian and ferroan chondrules, Ch1 and Ch5, respectively), and ferroan barred olivine chondrules (Ch4). The ferroan porphyritic chondrule (Ch2) includes Fe-Mg zoning olivine. Isotopic ratios of He in five chondrules are explained as a mixture of cosmogenic component and radiogenic ^4He. The concentrations of radiogenic ^4He in the ferroan porphyritic chondrule (Ch2) are variable from 0.6 to 5 × 10^{-5} cm^{3}STP/g. This variation would indicate a heterogeneity of U content in Ch2. Ne three-isotope plot shows that Ne in five chondrules is cosmogenic.

Concentrations of radiogenic ^{40}Ar in the five chondrules are variable among them and also within individual chondrule. The average concentrations of radiogenic ^{40}Ar in each chondrule are 1.0 - 2.5 × 10^{-5} cm^{3}STP/g. The variation of the radiogenic ^{40}Ar concentrations within individual chondrite is pronouncedly shown in Ch2 (0.3 - 3.8 × 10^{-5} cm^{3}STP/g). Those variations suggest the different contents of K among five chondrules and within each chondrule. Isotopic ratios of Ar, Kr, and Xe are compromised by the blank correction, resulted in large uncertainties for concentrations of ^{84}Kr and ^{132}Xe. The depletion of heavy noble gases indicates that the five chondrules in Parnallee are almost free from trapped components due to complete degassing during the chondrules formation.

In case of the matrix, isotopic ratios of He and Ne are also explained by cosmogenic component and radiogenic ^4He. $^{20}Ne/^{22}Ne$ and $^{21}Ne/^{20}Ne$ values (0.57 ± 0.18 and 0.62 ± 0.08, respectively) observed in a site of matrices indicate a contribution of Na-spallation ($^{20}Ne/^{22}Ne$ = 0.35, $^{21}Ne/^{20}Ne$ = 0.49 [8]) produced in sodium-rich phase by galactic cosmic ray. On the other hand, high concentrations and isotopic ratios of Ar, Kr, and Xe show the presence of primitive noble gases. The concentrations of trapped ^{36}Ar are 0.9 - 7.4 × 10^{-7} cm^{3}STP/g and those of ^{132}Xe are 0.3 - 3.5 × 10^{-9} cm^{3}STP/g. The values of $^{38}Ar/^{36}Ar$ in matrices are 0.18 - 0.23. Xe and Kr isotope compositions of matrices are similar to those of Q-gas [4]. Matrices also contain high concentrations of excess-^{129}Xe (0.4 - 2.3 × 10^{-9} cm^{3}STP/g) derived from a decay of ^{129}I. However, the elemental compositions of heavy noble gases in the Parnallee differ from those of Q-gas (Fig. 1). Trapped noble gases show higher $^{36}Ar/^{132}Xe$ (140 - 410) and $^{84}Kr/^{132}Xe$ (1.0 - 2.2) than those of Q-gas.

Those high elemental ratios suggest the contribution of subsolar component.

Cosmogenic He and Ne: Extracted ^{3}He and ^{21}Ne can be assumed as cosmogenic ^{3}He ($^{3}He_c$) and ^{21}Ne ($^{21}Ne_c$), because He and Ne in chondrules and matrix are dominated by cosmogenic component. Cosmic-ray exposure ages are calculated from the concentrations of $^{3}He_c$ and $^{21}Ne_c$. Production rates of $^{3}He_c$ and $^{21}Ne_c$ (P_3 and P_{21}) were obtained using the formulae by Eugster (1988) [9]. We assumed the average shielding parameter $(^{22}Ne/^{21}Ne)_c = 1.11$. The average exposure ages of each chondrule and matrices are given Table 1. The shorter exposure ages calculated from $^{3}He_c$ than those from $^{21}Ne_c$ are explained by diffusive loss of $^{3}He_c$ probably due to solar heating. Exposure ages calculated from $^{21}Ne_c$ in five chondrules have a variation (6.8 - 10 Ma). The difference of chemical composition among five chondrules possibly affects the production of cosmogenic ^{21}Ne. Exposure ages calculated from $^{3}He_c$ in matrices show relatively constant, because P_3 is hardly influenced by the chemical composition. Additionally, exposure ages of five chondrules are longer than those of matrices despite using $^{3}He_c$ or $^{21}Ne_c$. The excesses of cosmogenic noble gases in chondrules suggest pre-irradiation by galactic cosmic rays before the chondrules were incorporated into the parent body.

Trapped components in matrix: $^{36}Ar_{-trap}/^{132}Xe$ ratios and $^{84}Kr/^{132}Xe$ ratios (Fig. 1) fall in range between those of Q and subsolar component (South Oman [2]). If observed data represent fractionated subsolar gas only, the ratios of $^{36}Ar/^{132}Xe$ and $^{84}Kr/^{132}Xe$ are supposed to drop as the concentration of trapped noble gas decreases. However, elemental compositions neither correlate with the concentrations of trapped ^{36}Ar nor ^{132}Xe. Accordingly, trapped noble gases in matrices are mixture of subsolar and Q-gas components. The coexistence of the subsolar and Q-gas is generally found in enstatite chondrites classified as petrologic types of 4 to 6 [2, 3], but rare in ordinary chondrites. The host phase of subsolar gas is possibly enstatite [2] or amorphous material around enstatite grains [7]. On the contrary, Q-gas is generally contained in the carbonaceous phase-Q. The accumulation and intermixing mechanism of two different kinds of host phases on the Parnallee parent body reflects the formation process of ordinary chondrite parent body. To clarify relationship between the two primordial components, we will conduct the stepwise heating analysis for noble gases in the Parnallee meteorite.

References:

[1] Lewis R. S. et al. (1975) *Science*, *190*, 1251-1262. [2] Crabb J. and Anders E. (1981) *Geochim. Cosmochim. Acta*, *45*, 2443-2464. [3] Patzer A. and Schultz L. (2002) *Meteorit. Planet. Sci.*, *37*, 601-612. [4] Busemann H. et al. (2000) *Meteorit. Planet. Sci.*, *35*, 949-973. [5] Marti K. et al. (1972) *Astrophys. J.*, *173*, 445-450. [6] Okazaki R. et al. (2001) *Nature*, *412*, 795-798. [7] Nakamura T. et al. (2003) *Meteorit. Planet. Sci.*, *38*, 243-250. [8] Vogel N. et al. (2004) *Meteorit. Planet. Sci.*, *39*, 767-778. [9] Eugster O. (1988) *Geochim. Cosmochim. Acta*, *52*, 1649-1662.

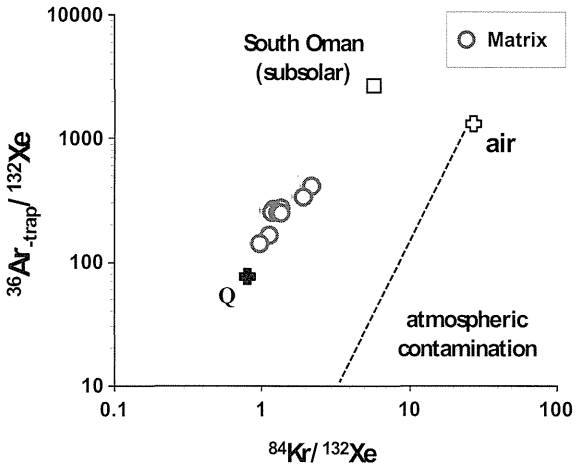

Fig. 1. Elemental ratios of trapped noble gases in matrices of the Parnallee meteorite. Dotted line indicates the fractionated terrestrial atmosphere. The elemental ratios of Q-gas and South Oman are from Busemann et al. (2000) [4] and Crabb and Anders (1981) [2], respectively.

Table 1. Concentrations of cosmogenic ^{3}He and ^{21}Ne, production rates, and cosmic ray exposure ages of Parnallee LL3.6 chondrite.

	$^{3}He_c$ (ave.)	P_3	T_3	T_3 (ave.)	$^{21}Ne_c$ (ave.)	P_{21}	T_{21}	T_{21} (ave.)
	10^{-8} cm^{3}STP/g	10^{-8} cm^{3}STP/g/Ma	Ma	Ma	10^{-8} cm^{3}STP/g	10^{-8} cm^{3}STP/g/Ma	Ma	Ma
Ch1	7.13		4.4		2.50		7.6	
Ch2	8.65		5.4		2.65		8.0	
Ch3	7.89	1.61	4.9	5.1	2.25	0.33	6.8	8.1
Ch4	8.60		5.3		3.33		10	
Ch5	9.17		5.7		2.69		8.1	
matrix	5.44	1.61	3.4		1.96	0.33	5.9	

THERMOLUMINESCENCE STUDY OF JAPANESE ANTARCTIC METEORITES XI

H. Matsui[1], K. Ninagawa[1], N. Imae[2], and H. Kojima[2]

[1]Okayama University of Science, [2]National Institute of Polar Research

Natural TL (thermoluminescence), the luminescence of a sample that has received no irradiation in the laboratory, reflects the thermal history of the meteorite in space and on Earth. Natural TL data thus provide insights into such topics as the orbits of meteoroids, the effects of shock heating, and the terrestrial history of meteorites. Induced TL, the response of a luminescent phosphor to a laboratory dose of radiation, reflects the mineralogy and structure of the phosphor, and provides valuable information on the metamorphic and thermal history of meteorites. The sensitivity of the induced TL is used to determine petrologic type of type 3 ordinary chondrites.

As reliable pairing approach, TL properties within large chondrites were analyzed, taking advantage of the fact that serial samples from these meteorites is known to be paired [1]. Then a set of TL pairing criteria: 1) the natural TL peak height ratios, LT/HT, should be within 20%; 2) that ratios of raw natural TL signal to induced TL signal should be within 50%; 3) the TL peak temperatures should be within 20℃ and peak widths within 10℃ was proposed. This set of TL pairing criteria is less restrictive than previously used [1].

We have measured TLs of 92 Yamato and 136 Asuka unequilibrated ordinary chondrites so far [1-5]. This time we measured TL of additional 42 Yamato 98 chondrites for determining 1) subtype and 2) pairing.

The TL data of them are listed in Table1. The petrologic subtype was determined from their TL sensitivity. Three chondrites, Y983183 (LL3.0), Y983278 (LL3.3-3.4), Y980324 (LL3.2-3.4) were revealed to be a primitive ordinary chondrites below petrologic subtype 3.4 as shown in Fig. 1.

Natural and induced TL properties were also applied to find paired fragments, and we found 24 TL potential paired fragments, satisfying TL pairing criteria [1]. We found five groups satisfying above TL pairing criteria as shown in Fig.2 A group of H3 comprises a chain of 7 potentially paired fragments, Y980052, Y980053, Y980054, Y980072, Y980074, Y980075, and Y980078. They were sampled at the same position, 35.336°E 72.152°S. They all could be paired. Sampling positions of another potentially paired fragments, Y980143 and Y980129, were close to each other. They also cloud be paired. However the other three groups of potentially paired fragments were away over 40 km from each other. Then they were not pair.

References: [1] Ninagawa et al. (1998): Antarctic Meteorite Res., 11, 1-17. [2] Ninagawa et al. (2000): Antarctic Meteorite Res., 13, 112-120. [3] Ninagawa et al. (2002): Antarctic Meteorite Res., 15, 114-121. [4] Ninagawa et al. (2005): Antarctic Meteorite Res., 18, 1-16. [5] Ninagawa et al. (2006): 30th Symp. Antarctic Meteorites, Tokyo, p.85-86 [6] Ninagawa et al. 2007. 31th symp. Antarctic Meteorites, Tokyo, p.75-76.

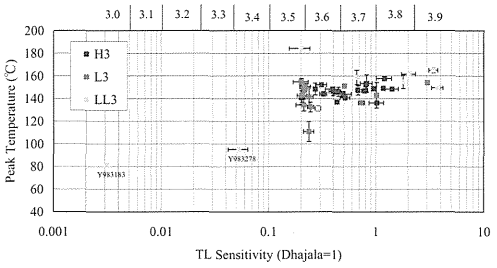

Fig.1. Correlation between TL sensitivity and peak temperature of forty-two Yamato chondrites.

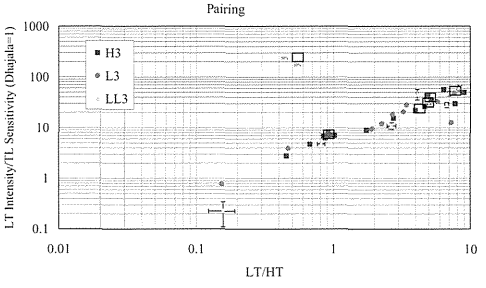

Fig.2 Ratio of LT to TL Sensitivity vs. LT/HT ratio to search fragments satisfying the pairing criteria 1) and 2).

Table 1 Thermoluminescence data of unequilibrated Japanese ordinary chondrites

Meteorite	Class	Natural TL				Induced TL				LT /TL Sens. ($x10^3$)	Low Ca-Py Heterogenity (C.V.)†	Ol Heterogenity (C.V.)‡	Ol Subtype	Sampling Location	
		LT/HT	LT (10^3 counts)	LT Peak Temp. (℃)	HT Peak Temp (℃)	TL Sensitivity (Dhajala=1)	Peak Temp. (℃)	Width (℃)	TL Subtype						
Y980006	L3	2.71 ± 0.04	9.4 ± 0.8	217 ± 1	337 ± 1	0.51 ± 0.00	151 ± 2	149 ± 0	3.7	18 ± 2	6%	3%		35.813 E	71.777 S
Y980016	H3	8.99 ± 0.41	13.5 ± 1.0	195 ± 3	372 ± 1	0.27 ± 0.01	149 ± 5	121 ± 2	3.6	50 ± 4	10%	10%	3.9	35.888 E	71.757 S
Y980049	H3	1.74 ± 0.07	9.2 ± 0.2	224 ± 5	331 ± 6	1.02 ± 0.16	136 ± 0	129 ± 21	3.7-3.8	9 ± 1	12%	3%		35.367 E	72.039 S
Y980052	H3	0.87 ± 0.02	5.0 ± 0.1	219 ± 2	338 ± 5	0.79 ± 0.05	147 ± 1	122 ± 8	3.7	6 ± 0	32%	11%	3.8	35.336 E	72.152 S
Y980053	H3	0.85 ± 0.02	6.6 ± 0.3	217 ± 2	338 ± 1	0.96 ± 0.03	149 ± 2	120 ± 10	3.7-3.8	7 ± 0	14%	7%	3.9	35.336 E	72.152 S
Y980054	H3	0.92 ± 0.03	3.3 ± 0.8	220 ± 9	345 ± 11	0.40 ± 0.03	147 ± 4	123 ± 1	3.6-3.7	8 ± 2	13%	8%	3.9	35.336 E	72.152 S
Y980072	H3	0.92 ± 0.03	3.3 ± 0.1	218 ± 3	339 ± 0	0.49 ± 0.10	144 ± 2	120 ± 6	3.6-3.7	7 ± 1	11%	15%	3.8	35.336 E	72.153 S
Y980073	H3	0.46 ± 0.01	1.9 ± 0.0	242 ± 1	347 ± 2	0.68 ± 0.01	147 ± 4	124 ± 3	3.7	3 ± 0	14%	9%	3.9	35.336 E	72.153 S
Y980074	H3	0.97 ± 0.04	5.9 ± 0.0	213 ± 5	338 ± 2	0.82 ± 0.10	153 ± 8	126 ± 2	3.7-3.8	7 ± 1	28%	23%	3.7	35.336 E	72.153 S
Y980075	H3	1.03 ± 0.02	5.7 ± 0.4	213 ± 2	337 ± 2	0.81 ± 0.03	152 ± 3	129 ± 3	3.7	7 ± 1	31%	15%	3.8	35.336 E	72.153 S
Y980078	H3	0.94 ± 0.02	8.6 ± 0.3	213 ± 1	333 ± 1	1.17 ± 0.04	149 ± 0	127 ± 3	3.8	7 ± 0	23%	4%		35.336 E	72.153 S
Y980129	H3	5.18 ± 0.04	42.8 ± 6.9	200 ± 5	337 ± 12	1.21 ± 0.20	158 ± 1	132 ± 2	3.7-3.8	35 ± 8	30%	2%		35.170 E	72.432 S
Y980139	LL3	7.00 ± 0.11	163.3 ± 8.6	189 ± 3	329 ± 12	3.56 ± 0.53	156 ± 6	140 ± 4	3.9	46 ± 7	14%	2%		35.370 E	72.537 S
Y980143	H3	5.13 ± 0.32	18.6 ± 4.0	201 ± 2	329 ± 6	0.47 ± 0.10	146 ± 3	131 ± 3	3.6-3.7	40 ± 12	32%	3%		35.259 E	72.388 S
Y980169	LL3	4.11 ± 0.06	9.2 ± 0.8	217 ± 0	311 ± 0	0.20 ± 0.04	184 ± 0	124 ± 9	3.3-3.4	46 ± 11	7%	4%		35.305 E	72.388 S
Y980178	H3				333 ± 3	1.42 ± 0.20	148 ± 1	128 ± 0	3.8		9%	5%	3.9	35.340 E	72.483 S
Y980181	L3	0.47 ± 0.03	12.0 ± 0.0	233 ± 1	336 ± 0	3.04 ± 0.09	154 ± 1	118 ± 5	3.9	4 ± 0	30%	3%		35.341 E	72.648 S
Y980209	LL3	0.82 ± 0.05	8.6 ± 0.2	236 ± 0	315 ± 4	1.80 ± 0.02	155 ± 6	123 ± 1	3.8	5 ± 0	9%	1%		35.368 E	72.292 S
Y980324	L3	5.61 ± 1.19	1.8 ± 0.7	188 ± 1	371 ± 4	0.03 ± 0.00	141 ± 7	129 ± 5	3.2-3.3	73 ± 33	21%	28%	3.7	35.303 E	72.285 S
Y980387	L3	10.12 ± 0.60	11.5 ± 0.8	189 ± 2	321 ± 3	0.20 ± 0.02	143 ± 6	130 ± 4	3.5-3.6	56 ± 7	28%	5%	3.9	35.129 E	72.068 S
Y980388	L3	2.25 ± 0.09	2.8 ± 0.3	211 ± 4	329 ± 7	0.24 ± 0.02	142 ± 9	124 ± 3	3.5-3.6	12 ± 2	41%	5%	3.9	35.127 E	72.067 S
Y980429	L3	3.44 ± 0.37	6.1 ± 1.2	205 ± 1	324 ± 7	0.22 ± 0.02	150 ± 3	170 ± 9	3.5-3.6	28 ± 6	31%	8%	3.9	35.122 E	72.067 S
Y980449	L3	3.25 ± 0.26	4.4 ± 0.3	201 ± 2	323 ± 5	0.21 ± 0.03	134 ± 5	136 ± 2	3.5-3.6	21 ± 3	37%	5%	3.9	35.133 E	72.070 S
Y980453	L3	5.76 ± 0.75	8.1 ± 0.3	191 ± 2	318 ± 1	0.24 ± 0.02	133 ± 4	134 ± 2	3.6	33 ± 3	37%	5%	3.9	35.121 E	72.069 S
Y980560	LL3	6.72 ± 0.20	105.8 ± 4.0	190 ± 0	321 ± 2	3.76 ± 0.44	149 ± 1	118 ± 1	3.9-4	28 ± 3	18%	3%		34.953 E	72.048 S
Y980585	LL3	8.39 ± 0.09	42.1 ± 3.6	193 ± 0	316 ± 3	0.67 ± 0.01	159 ± 6	136 ± 4	3.7	63 ± 6	44%	5%	3.9	35.124 E	72.071 S
Y980586	LL3	5.03 ± 0.01	7.9 ± 0.0	202 ± 2	317 ± 3	0.29 ± 0.02	131 ± 2	132 ± 2	3.6	27 ± 2	38%	8%	3.9	35.122 E	72.063 S
Y980593	L3	8.20 ± 0.00	11.4 ± 0.4	191 ± 4	312 ± 4	0.20 ± 0.03	155 ± 3	134 ± 0	3.5-3.6	57 ± 9	43%	5%	3.9	35.124 E	72.071 S
Y980595	L3	2.60 ± 0.06	2.1 ± 0.3	199 ± 1	333 ± 8	0.22 ± 0.01	147 ± 2	137 ± 1	3.5-3.6	10 ± 1	29%	9%	3.9	35.127 E	72.069 S
Y980660	H3	3.99 ± 0.27	11.3 ± 0.8	193 ± 1	338 ± 1	0.52 ± 0.06	141 ± 2	120 ± 0	3.6-3.7	22 ± 3	29%	43%	3.5	35.246 E	72.082 S
Y980847	L3	1.91 ± 0.02	2.0 ± 0.1	219 ± 1	315 ± 5	0.21 ± 0.01	144 ± 4	134 ± 2	3.5-3.6	10 ± 1	25%	9%	3.9	35.125 E	72.059 S
Y981736	LL3	2.67 ± 0.21	22.3 ± 0.7	213 ± 1	351 ± 2	2.05 ± 0.31	162 ± 0	165 ± 7	3.8-3.9	11 ± 2	18%	7%	3.9	35.091 E	72.137 S
Y982376	L3	0.15 ± 0.01	0.8 ± 0.0	199 ± 1	329 ± 0	1.02 ± 0.02	143 ± 11	131 ± 2	3.8	1 ± 0	7%	3%		35.276 E	71.961 S
Y982399	L3	7.62 ± 0.28	11.5 ± 0.3	195 ± 2	330 ± 1	0.24 ± 0.03	111 ± 9	141 ± 6	3.5-3.6	49 ± 5	25%	7%	3.9	35.150 E	72.075 S
Y982965	H3	7.72 ± 0.03	9.3 ± 0.2	209 ± 1	352 ± 0	0.31 ± 0.04	152 ± 0	132 ± 0	3.6	30 ± 3	18%	4%		35.063 E	71.768 S
Y983183	LL3		0.023 ± 0.001	204 ± 4		0.0032 ± 0.0001	81 ± 1	±	3.0	7 ± 0	61%	59%	<3.4	36.032 E	71.662 S
Y983276	H3	0.68 ± 0.03	2.1 ± 0.5	235 ± 0	338 ± 0	0.45 ± 0.02	146 ± 4	132 ± 2	3.6.-3.7	5 ± 1	31%	3%		36.043 E	71.660 S
Y983278	LL3	0.16 ± 0.03	0.0 ± 0.0	202 ± 5	363 ± 3	0.05 ± 0.01	95 ± 1	85 ± 1	3.3-3.4	0 ± 0	76%	47%	3.5	36.021 E	71.664 S
Y983289	L3	7.22 ± 0.21	9.3 ± 0.1	202 ± 1	367 ± 1	0.74 ± 0.05	136 ± 1	115 ± 3	3.7	13 ± 1	14%	3%		35.907 E	71.693 S
Y983405	H3	6.42 ± 0.26	11.4 ± 0.1	200 ± 1	325 ± 10	0.20 ± 0.00	141 ± 6	153 ± 3	3.5	57 ± 0	70%	26%	3.7	35.959 E	71.641 S
Y983420	H3	4.69 ± 0.11	8.4 ± 0.2	209 ± 8	342 ± 6	0.32 ± 0.03	144 ± 2	127 ± 1	3.6	26 ± 2	36%	5%	3.9	35.942 E	71.654 S
Y983535	H3	2.75 ± 0.00	6.7 ± 0.8	211 ± 1	336 ± 0	0.43 ± 0.00	137 ± 1	135 ± 4	3.6	15 ± 2	35%	3%		35.939 E	71.658 S

Calcium silico-phosphates in angrites and experimentally-heated eucrite: Implication for their crystal chemistry and crystallization. T. Mikouchi[1], A. Yamaguchi[2], K. Sugiyama[3], and Y. Kato[3], [1]Department of Earth and Planetary Science, University of Tokyo, Hongo, Bunkyo-ku, Tokyo 113-0033, Japan (mikouchi@eps.s.u-tokyo.ac.jp), [2]National Institute of Polar Research, Midori-cho, Tachikawa, Tokyo 190-8518, Japan, [3]Institute for Materials Research, Tohoku University, Aoba-ku, Sendai, Miyagi 980-8577, Japan.

Introduction:

An unknown calcium silico-phosphate (CSP) was first reported from the Asuka-881371 angrite as tiny euhedral or lathy grains at the Fe-rich rim of Al-Ti-rich clinopyroxene ("fassaite") [1,2]. They were also found from additionally discovered angrites as a similar occurrence [3]. Their detailed mineralogy has not been fully understood yet due to their small size and low abundance. In our previous studies, we have analyzed its crystallographic properties by Raman spectroscopy and SEM-EBSD analysis, and then revealed that it has a graserite structure and may be nagelschmidtite [4]. The graserite structure is hexagonal with the space group of $P6_3/m$. In this structure, cations and anions are arranged in two types of columns in a hexagonal arrangement [e.g., 5]. Similar CSP was then found in experimentally-heated Hammadah al Hamra 262 (HaH262) eucrite [6], but it has not been well characterized either. In this abstract, we report further mineralogical analysis of CSP in these samples and discuss their crystal chemistry and crystallization from P-rich evolved silicate melt.

Analytical Methods:

The chemical compositions of CSPs in "quenched" angrites (Asuka-881371, Sahara 99555, and D'Orbigny) and experimentally-heated HaH262 (1070 °C for 24 hours at logfO_2=IW-1) were determined by electron microprobe (JEOL JXA-8900L) after their distributions were detected by X-ray mapping. They were then carefully analyzed by FEG-SEM (Hitachi S-4500) equipped with Kevex EDS and ThermoNoran Phase ID EBSD detectors. The EBSD analysis followed the method described in [7]. Raman spectroscopy was performed by JASCO NRS-1000.

Results:

In Asuka-881371, Sahara 99555 and D'Orbigny, CSP usually occurs as a cluster of tiny euhedral or lathy grains associated with other late-stage crystallization phases such as troilite, ulvöspinel, and Fe, Ca-rich olivine. [1-4]. Each grain is mostly up to several tens of μm in size, but those in Sahara 99555 are smaller than those in others. Their chemical compositions show slight scatters from one grain to another (Fig. 1), but they appear fairly homogeneous in each grain. Their representative compositions are shown in Table 1. We found that CSP in angrites has a close chemical composition to synthetic silicocarnotite ($Ca_5(SiO_4)(PO_4)_2$), but different from nagelschmidtite ($Ca_7(SiO_4)_2(PO_4)_2$) (Table 1 and Fig. 1) [4].

CSP in experimentally-heated HaH262 is a rare irregular small grain up to 20 μm in size coexisted with augite or/and plagioclase (Fig. 2). The grain boundary between other grains is partly ambiguous, and the grain appears amorphous (Fig. 2). Unlike CSP in angrites, the chemical composition is heterogeneous even in each grain, ranging from Si-poor Ca phosphate to P-poor silicate (Fig. 1).

The Raman spectroscopy of these phases shows generally similar spectra that are characterized by a strong peak at around 960 cm^{-1} [4]. Surprisingly, CSP in experimentally-heated HaH262 is crystalline in spite of its amorphous-like appearance and heterogeneous composition.

The EBSD analysis of CSP in angrites shows that the obtained Kikuchi bands can be indexed by the graserite structure such as apatite [4]. It can be also indexed by the nagelschmidtite structure ($P6_1$, a=10.82 Å, c=21.46 Å) that was determined by our recent work using a synthetic phase [4] although its chemical composition is closer to silicocarnotite. We also analyzed CSP in experimentally-heated HaH262 by EBSD and could obtain Kikuchi bands although it was not successful before. In a single grain, the obtained Kikuchi bands show the same pattern in spite of different P and Si contents. Even if the Si content is as much as P, its EBSD pattern was identical to that of Si-free merrillite. Thus, these EBSD patterns could not be indexed by either nagelschmidtite or silicocarnotite, but could be indexed by the merrillite structure (Fig. 3).

Discussion and Conclusion:

In our previous study [4], we could produce both silicocarnotite and nagelschmidtite by synthetic experiments in the system of $2CaO \cdot SiO_2$-$3CaO \cdot P_2O_5$ [e.g., 8]. The crystal structure of possible nagelschmidtite ($P6_1$, a=10.82 Å, c=21.46 Å) was turned out to be unique in comparison with α-Ca_2SiO_4 ($P6_3/mmc$, a=5.42 Å, c=7.03 Å) because it showed a superstructure with $2a$ and $3c$ axial lengths. The nagelschmidtite structure can be explained by the substitution of one of SiO_4 tetrahedra and Ca sites of α-Ca_2SiO_4 by vacancy and PO_4 tetrahedron, respectively by the reaction: $2SiO_4 + Ca \rightarrow 2PO_4 + \square Ca$ [4]. As demonstrated by the EBSD analysis, CSP in angrites has a graserite structure. However, it is not clear whether it is nagelschmidtite or not. Its chemical composition is rather closer to silicocarnotite although EBSD

analysis ruled out that it is silicocarnotite. CSP phases have wide compositional ranges because of the presence of abundant Fe, and thus the chemical composition is not conclusive to identify the mineral species. Unlike CSP in angrites, CSP in experimentally-heated HaH262 has a merrillite structure, suggesting that merrillite can contain large amount of silica without structural changes. Since such a phase is not known in the system of $2CaO \cdot SiO_2$-$3CaO \cdot P_2O_5$, this system probably contains more complex phase relations than previously considered and further study is required.

Why is the occurrence of CSP so rare in natural system? One possibility is that we are just not aware of their presence because of their small size and low abundance. However, we consider that they are really rare products that crystallize only from Fe-rich (Mg-free) basaltic melt enriched in Ca and P. Among achondritic meteorites, nearly Mg-free late-stage melt in angrites produces such a composition. Lunar mare basalt and Martian meteorites sometimes show Fe enrichment reaching atomic Fe/(Fe+Mg)=1, but CSP is not found. This is probably because their Ca contents are not sufficient compared to angrites. Experimentally-heated HaH262 at 1070 °C could produce melt enriched in Ca, Si and P probably similar to late-stage melt of angrites by partial melting of Ca phosphates, ilmenite and silica (plus minor pyroxene and plagioclase), thus leading crystallization of CSP. In experimentally-heated HaH262, CSP was found only in the run product heated at 1070 °C, and not found in experimental charges at either 1100 °C or 1050 °C. In this series of experiment, Ca phosphate was completely melted at 1100 °C, but was not at 1050 °C [6]. Therefore, 1070 °C was the critical temperature that crystallized CSP in this system. However, CSP in experimentally-heated HaH262 is different from that in angrites, which makes their nature still enigmatic.

Table 1. Chemical compositions of CSP in angrites, heated HaH262 and synthetic experiments.

	1	2	3	4	5	6
SiO_2	11.9	12.5	12.2	18.1	18.1	10.9
Al_2O_3	0.2	1.5	0.2	1.5	-	-
TiO_2	1.6	0.8	1.6	0.3	-	-
FeO	4.7	9.2	4.9	7.0	0.96	0.44
MnO	0.1	0.1	0.1	0.21	-	-
CaO	49.8	41.1	48.6	42.0	58.3	57.5
P_2O_5	29.0	33.8	30.5	29.0	18.9	29.2
Total	97.3	99.0	98.1	98.1	96.3	98.0

1: Angrite Asuka-881371. 2: Angrite Sahara 99555. 3: Angrite D'Orbigny.
4: Heated HaH262 (1070 °C).
5: Synthetic nagelschmidtite. 6: Synthetic silicocarnotite.

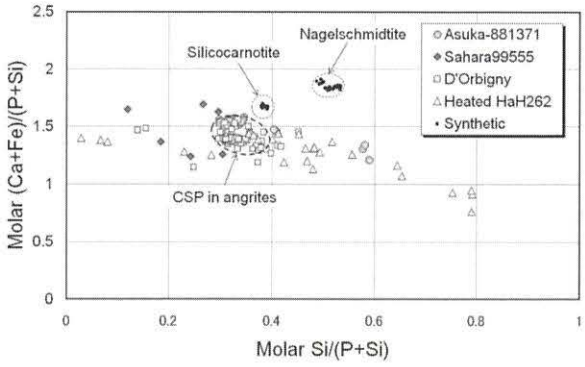

Fig. 1. Molar Si/(P+Si) vs. (Ca+Fe)/(P+Si) in CSP from angrites, heated HsH262 and synthetic phases. CSP in angrites is close to the silicocarnotite composition. The stoichiometric silicocarnotite is molar Si/(P+Si)=0.33 and (Ca+Fe)/(P+Si)=1.67, respectively. The stoichiometric nagelschmidtite is molar Si/(P+Si)=0.50 and (Ca+Fe)/(P+Si)=1.75, respectively. Both compositions are close to synthetic phases, respectively.

References:

[1] Prinz M. and Weisberg M. K. (1995) *Antract. Meteorites*, *XX*, 207-210. [2] Warren P. H. and Davis A. M. (1995) *Antarct. Meteorites*, *XX*, 257-260. [3] Kaneda K. et al. (2001) *LPS XXXII*, Abstract #2127. [4] Mikouchi T. et al. (2010) *LPS XLI*, Abstract #2343. [5] Mathew M. and Takagi S. (2001) *Jour. Res. National Inst. Stand. Tech., 106*, 1035-1044. [6] Yamaguchi A. and Mikouchi T. (2005) *LPS XXXVI*, Abstract #1574. [7] Mikouchi T. et al. (2009) *Amer. Mineral., 93*, 746-750. [8] Fix W. et al. (1969) *Jour. Amer. Ceram. Soc., 52*, 346-347.

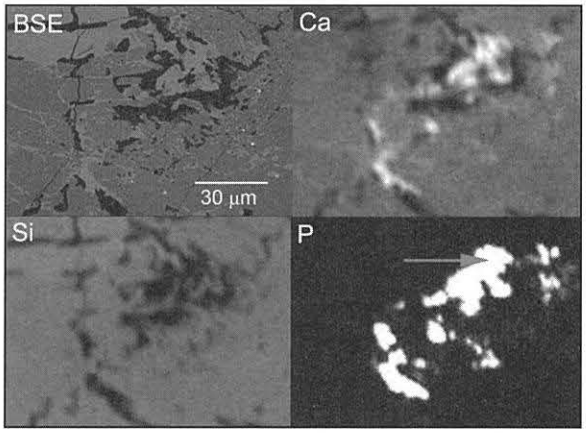

Fig. 2. Back-scattered electron image and X-ray (Ca, Si and P) maps of experimentally heated HaH262 showing irregularly-shaped CSP. The arrow in the P map shows the point analyzed by EBSD (Fig. 3). The chemical composition of this point is shown in Table 1.

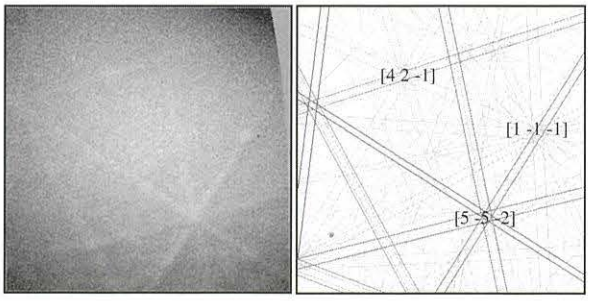

Fig. 3. Observed and calculated EBSD patterns of CSP in experimentally heated HaH262. The observed pattern (left) can be indexed by the merrillite structure (right).

Accretion rate of micrometeorites in ice chips shaved while ice core drilling from 1700 m in depth at Dome Fuji.

A. Miura[1], T. Fukuoka[1] and Y. Tazawa[1], [1]Graduate School of Geo-environmental Science, Rissho University, Kumagaya 360-0194, Japan (A. Miura's E-mail: 098w00004@ris.ac.jp).

Introduction:

The accretion rate of micrometeorite to the Earth has been reported, e.g., 2700 t/y [1], 5300~16000 t/y [2] etc. Goal of this study is that we estimate secular variation of the accretion rate of micrometeorites.

The Antarctic regions, because inputting terrestrial matter from surrounding continent is very low, we can recover micrometeorites from ice sheet. And we can get the age information from the depth of ice core, because snow precipitate horizontally at the Dome Fuji [3]. But ice core keeps a lot of paleo-environmental records, we cannot use large amount of ice core. Instead of ice core, we used ice chips shaved while drilling ice core at 1700 m in depth at Dome Fuji. The age and weight of which are approximately 120 Kyr ago and 40 kg, respectively.

The accretion rate of micrometeorite with 100–150 μm in size is approximately 20 particles $y^{-1}m^{-2}$ in blue ice around Yamato Mts. [2]. If the accretion rates of micrometeorites at Antarctica were constant without regard to area and age, micrometeorites with the same size range should be contained about 10^3 particles in Dome Fuji ice chips mentioned above.

Experimentals:

Firstly ice chips were melted and filtrated by Nuclepore filters (with diameter of 47 mm, pore size of 8.0 μm). Then we tried to pick up micrometeorites of the size range over 8.0 μm under a stereomicroscope. But we could not find micrometeorites over 8.0 μm in size. Probable reasons are, 1) the micrometeorites did not fall on Antarctica ca 120 Kyr ago, 2) those were crushed by compaction of the ice sheet, 3) those accreted approximately 120 Kyr ago were too small in size(<8.0 μm). If it is the case 2) or 3), micrometeorites filtrated with pore size less than 8.0 μm, could remain onto the filters as residues. However it is hard to handpick and analyze particles less than 8.0 μm in size, individually.

Siderophile element is very rare in Earth's crust, while rich in the extraterrestrial matters such as chondrites. Criteria for extraterrestrials or terrestrials are a certain amount of Au and/or Ir in filters, or not. However Au was contained as contamination in Zn plate with which steel wire coated, and by which a deep ice core drill was tied. There were large amount of Zn plating fragments onto filters. Au is inconvenient for the criterion. Finally in this study, and we analyzed Ir contents in the residues on the filters. We report the accretion rate of micrometeorites estimated by Ir contents of those collected on filters.

After first filtration mentioned above, the filtrate was filtered with pore size of 0.8 μm and 0.2 μm. The residues on the filters were weighed and analyzed by instrumental neutron activation analysis (INAA).

Results and Discussion:

The result of this study is shown in table.1, together with that on Greenland Ice Sheet Project 2 (GISP2) ice core [4], and that on blue ice around Yamato Mts. in Antarctica [2]. We estimate the accretion rate of micrometeorites are $(0.12 \pm 0.03) \times 10^9$ g·yr^{-1} in size range 0.2–8.0 μm. If there were not micrometeorites greater than 8.0 μm, the gross weight of micrometeorites less than 8.0 μm would be the accretion rate in depth 1700 m. Then compare with the present accretion rate [1, 2], the result of this study (accretion rate of 120 Kyr ago) is low about three order of magnitude. But the accretion rate of small size range (~20–0.45 μm) micrometeorites at GISP2 was reported $(0.32 \pm 0.21) \times 10^9$ g·yr^{-1} [4], that corresponds our result with in a order of magnitude. In this case, if there were large micrometeorites in 120 Kyr, those could flow out electively in ice sheet.

References: [1] S. Taylor et al. (1998) *Nature* **392**, 899–903. [2] T. Yada et al.(2004) *Earth Planets Space* **56**, 67–79. [3] T. Hondoh et al.(2004) *Polar Meteorol. Glaciol.* **18**, 1–18. [4] D.B. Karner et al.(2003) *GCA* **67**, 751–763

Table 1. Accretion rate estimates for Earth.

Study Area	Mesurement element	Depth (m)	Core length (cm)	Age (kyr)	Sample area (cm^2)	ice mass (kg)	Dust size range (μm)	Dust Weight ($\times 10^{-3}$g)	Ir content ($\times 10^{-15}$g)	±	Accretion rate* ($\times 10^9$ g·yr^{-1})	±
Dome Fuji ice chip (This study)	Ir	1700	400	120	113	40	0.2-8.0	28.3	1.18	0.29	0.12	0.03
Greenland ice[4]	Ir	1131-1135	400	6	3.85	1.4	~20 >0.45	0.171	8.2	2.4	0.32	0.21
Antarctic bule ice[2]	^{20}Ne	~1	-	30	70600	910	40-238	0.657	-	-	16	9.3

*area Earth 5.1×10^{18}cm^2

Material Indicator of Sea-Water Impact: Halite and Calcite Carbonates in Composition.

Yas. Miura, Yamaguchi University, Yoshida 1677-1, Yamaguchi, 753-8512, Japan. dfb30@yamaguchi-u.ac.jp

Introduction:

Main material indicators of impact-related mineral material with optical microscopic observation are studied on impacts on dry lands as remained samples of Earth, Moon, Asteroids and Mars. Almost all impact materials (including meteorites) on sea-water are considered to be broken to melt away on the water-planet Earth. The present main purpose is to elucidate any microscopic evidences of sea-water impacts, which are not original impact materials but solidified to other combined materials with supplied elements during impact process [1-5].

Samples of impacts on dry rocks and sea-water:

Remained impact materials which are previously studied so much, are mainly metamorphic solids of dry target-rocks as silica-rich rocks (silicates or oxides) and carbon-rich rocks (limestone or carbonates), together with meteoroids projectile as iron-rich oxides etc., which can be found so far on Earth, the Moon, Asteroids and Mars.

However, meteoroids (asteroids) collided to sea-water (ca.70 vol.% of Earth's surface) are almost broken and melted away in water condition after impact event. Therefore, previous material evidences on sea-water impact are summarized as follows:

a) "dark-brownish thin-layer of geological boundary" (the KTB or PTB) with iron-rich oxides or sulfides etc. [1].
b) "bulk elemental concentration" of Pt-group elements (including Ir) after concentration during formation of geological boundaries.
c) remained metamorphic materials of spherule glasses and minerals of graphite- diamond carbon, shocked quartz, shocked calcite or zircon etc. which are mainly based on target rocks of sea-bottom if it is large impact.

The above-mentioned impact-related materials are not direct information of sea-water impact, because these are based on re-formed materials of meteoritic or dry target rocks. There are few evidences of sea-water composition or sea-bottom rocks by impact.

Impact glasses and breccias on sea-water impact:

After sea-water impact which almost all fragments are broken immediately in the water, only remained materials of sea-water impact are impact glasses and/or breccias formed as quenched process during impact as follows [3-5]:

a) Sample: direct impact glassed and/or breccias.
b) Size: nano-grains (as 100nm aggregates).
c) Composition: halite (solidified from sea-water), or carbonates of calcite etc. (from shallow sea-bottom rocks).

Chlorine-bearing materials in impact glasses:

Significant amounts of chlorine are found from solidified materials of fine halite from salty sea-water from shallow to deep impacts (Fig.1). This is mainly because chlorine-bearing minerals by direct collision by meteoroids (in air or target rocks) are akaganeite in composition by contribution from meteoritic projectiles [3-5].

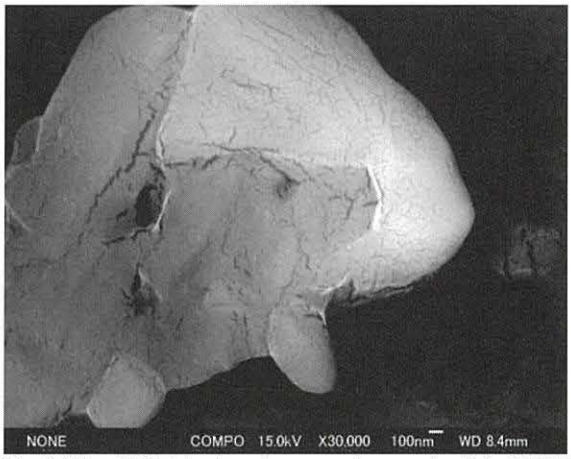

Fig.1. The ASEM in-situ electron-micrograph of the LDSG tektite sample with C, Mg, Al, K, Cr and Fe (back) [4], together with Na and Cl (white grains). Impact halites are aggregates of nano-particles (10nm in size). The scale bar is 100nm.

Carbon-bearing materials by impacts:

Significant amounts of carbon (C) are found in the following materials with different C contents:

a) glasses quenched during impact with low C content,
b) new quenched deposits of carbon-bearing fine particles with medium C content, and
c) carbon solids formed by dynamic impact reaction with high C contents [3-5].

Fine particles with carbon-bearing materials show the following characteristics:

a) irregular shapes and nanometer sizes, and
b) various aggregates with micrometer to 100nm in size.

The above characteristics indicate rapid cooling during impact from target rocks of carbonates from sea-bottom sediments.

Therefore, carbon-bearing particles with nano-particles with irregular shape are considered to be formed by sea-water impact, together with chlorine-rich halite with fine nano-particles by quenching in sea-water (Fig.2).

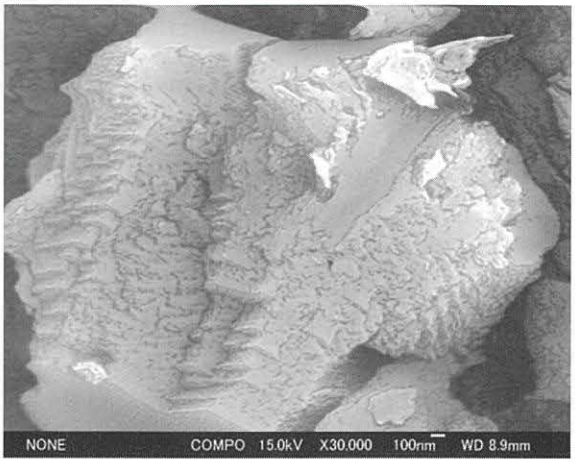

Fig.2. The ASEM in-situ electron-micrograph of the LDSG tektite sample of fine Ca-carbonates (calcite) in composition (white) [4]. Impact calcite carbonate in sea-water impact are aggregates of nano-particles (10nm in size) in quenching in sea-water. The scale bar is 100nm.

Impact carbon- and chlorine-bearing particles:

Fine carbon- and chlorine-bearing particles are founds in samples of sea-impacts of the drilled core and glasses as followed (see Table 1):

a) Takamatsu (Kagawa, Japan) in drilled grains as shown in Fig.3,
b) the Akiyoshi (Yamaguchi, Japan) in drilled core,
c) Libyan desert silica glasses LDSG (Libya, Africa) in cavity or vein, and
d) Congo diamond (Africa) in vein and cavity,
e) the KT and PT geological boundary samples (Spain, and Meishan China) [3-5].

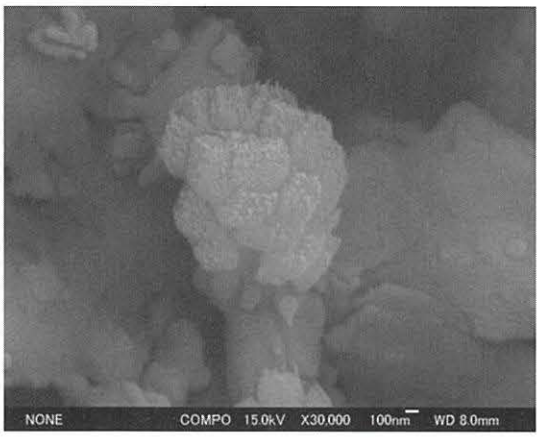

Fig.3. High-resolution (FE-SEM) electron micrographs of fine carbon-bearing particles on the Takamatsu drilled breccias sample of 950m in depth formed by impact on sea-carbonates. Previous results on impact on granitic rocks have few calcite or carbon-bearing rocks, though there are different sea-bottom rocks with carbon. Bar is 100nm in scale [5].

Table 1. Origins of carbon & chlorine in sea-water impacts [3-5].

Carbon:	Shallow origin from carbonate rocks (calcite etc.). Deep origin from sea-water (carbonate ions etc.).
Chlorine:	Sea-water origin to solidified halite. (cf. Meteoritic origin to solidified akaganeite-like materials).

Summary:

The present study is summarized as follows:

1) Material evidences of sea-water impact are obtained as carbon-bearing fine-particles with irregular shapes from carbonate rocks (with calcite) or deep sea-water, together with fine halite-particles from chlorine-bearing sea-water, though chlorine-bearing meteoritic source is found as akaganeite minerals in composition.
2) Typical examples of fine carbon- and chlorine-bearing particles are found in the Takamatsu (Japan), the Akiyoshi (Japan), the Libyan glasses (Libya, Africa), Congo diamonds, and the KT and PT geological samples (Europe and China), almost which are related with sea-water impact (including shallow crust explosion in liquid states in the Congo diamonds).

Acknowledgements:

Author thanks for Drs. T. Kato and T. Tanosaki for this discussion.

References:

[1] Miura et al. (1995): Meteoritics (USA), 30(5), 552.
[2] Miura Y. (2009): LPI Contribution No.1515 (LEAG2009, USA). 44, CD#2042, 2043.
[3] Miura Y. (2009): LPI Contribution No. 1468 (LPSC40, USA), CD#2565 (pp.2)
[4] Miura Y. (2009): Antarctic Meteorites XXXII (NIPR), 32, 39-40.
[5] Miura Y. Tanosaki and Udagawa M. (2010): Shock Waves in Japan (Saitama Univ.), 117-118.

Shock induced high-pressure phases in the shock veins of NWA 5011 L6 chondrite. Sz. Nagy[1] (ringwoodite@gmail.com), S. Józsa[1], Sz. Bérczi[1], A. Gucsik[2,3], M. Koós[4], M. Veres[4]
[1]Eötvös Loránd University of Budapest, Pázmány Péter sétány 1/c, H-1117 Budapest, Hungary; [2]Max Planck Institute for Chemistry, Becherweg 27, D-55128 Mainz, Germany; [3]Savaria University Center, University of West Hungary, Károlyi Gáspár tér 4., H-9700 Szombathely, Hungary; [4]Research Institute for Solid State Physics and Optics of the Hungarian Academy of Sciences, PO Box 49. H-1525 Budapest, Hungary.

Introduction: High-pressure minerals are common in highly shocked (S6) L6 chondrites. These minerals provide evidence of very high pressure and temperature conditions during impact events [1]. The NWA 5011 meteorite contains few microns to several millimeter wide shock veins, which show complex mineralogy. The abundant high-pressure phases and intensive melting features exhibit high porosity of the bulk rock, and significant shearing mechanism during impact. $MgSiO_3$-ilmenite, and $NaAlSi_3O_8$-hollandite show that crystallization pressure slightly exceeds above 20 GPa, but does not reach 23 GPa, since decomposition products of ringwoodite and majorite were not observed.

Sample and Experimental Procedure: Two polished thin sections have been made for optical and instrumental investigations, respectively. One of the thin sections has 25-30 μm, and the other one 40 μm thickness. The mineral assemblages and texture were characterized with a Nikon Eclipse LV100POL optical microscope. The phase identification and Raman spectra were recorded with a Renishaw RM-2000 Raman spectrometer attached to a Leica DM/LM microscope. A 785 nm diode laser served as excitation source, its 8 mW power was focused into a spot having diameter of 1 μm. Backscattered electron (BSE) images and mineral analysis were obtained using Jeol 733 microanalyser at Eötvös University of Budapest.

The NWA 5011 meteorite was found in Morocco, in 2005. The date of fall is unknown. The NWA 5011 is an L6-type chondrite containing abundant shock veins having sizes between few microns and several millimeters (Fig. 1). The main modal components are as follows: olivine, orthopyroxene, feldspar (generally in form of maskelynite), troilite. Minor components include ilmenite and chromite.

Results: The NWA 5011 consists of shock-induced melt veins and nest-like melt pockets. The shock veins show abundant high-pressure mineral polymorphs of olivine, pyroxene, and feldspar. These phases related to in or adjacent of the shock veins. No phase transitions can be observed outside the shock veins, which suggests, that the mechanism of transition process needs high temperatures rather than high pressures [2].

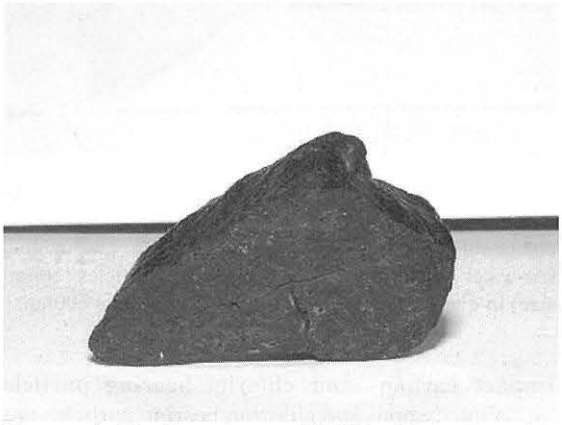

Figure 1. Handspecimen of NWA 5011 meteorite. The abundant shock veins network is clearly seen.

In previous studies, it was assumed that during impact events these L6-chondrites have high porosity, which could produce shock veins by heat accumulation, or shearing process [2]. We observed nest-like melt pockets in NWA 5011, and these melt pockets were attached each other by very thin veins.

The ringwoodite is the most spectacle high-pressure polymorph in shock veins of NWA 5011 exhibiting various colors from deep blue to colorless (Fig. 2). The source of colorization is poorly understood but it may be related to cation substitutions in the crystal structure [3]. However, micro-Raman spectroscopic investigations didn't show any structural difference between deep blue and colorless ringwoodites. The Si-atom has sixfold coordination in inverse spinel structure (in normal spinel it has fourfold coordination) therefore the structural differences should be observed in micro-Raman spectra. If the inverse ringwoodite is present, its formation requires significantly higher temperatures, than normal spinel [4]. The ringwoodite grains have similar chemical compositions to olivine grains of the chondritic part ($(Mg_{1.44}\ Fe_{0.56})\ Si_{1.00}O_4$); ($Fo_{72}$-$Fa_{28}$). The Mg# are between 0.67 and 0.75. The value of 0.67 was obtained in ringwoodite lamellae which are reach in Fe. In the Raman spectra the spinel structure shows peaks at 795 and 840 cm^{-1}. An additional peak appears at around 875 cm^{-1}, which wasn't observed in ringwoodite spectrum before. The peak was detected in well crystallized ringwoodite grains, which excludes glassy material as its origin. According to Prof. Paul McMillan (in personal

communication) it could be related to a defect induced vibrational mode, or a new Ca-orthosilicate phase [5]. However, the Ca-orthosilicate origin can be excluded, because the CaO content of ringwoodite is below 0.1 wt% (for Ca-orthosilicate it should be above 30 wt%). It is worth to note that Raman spectra were recorded in the central part of a 200 μm long and 150 μm wide ringwoodite grain, and not in the vicinity of the grain boundaries. The presence of this peak in the spectrum will be confirmed by using another excitation energy.

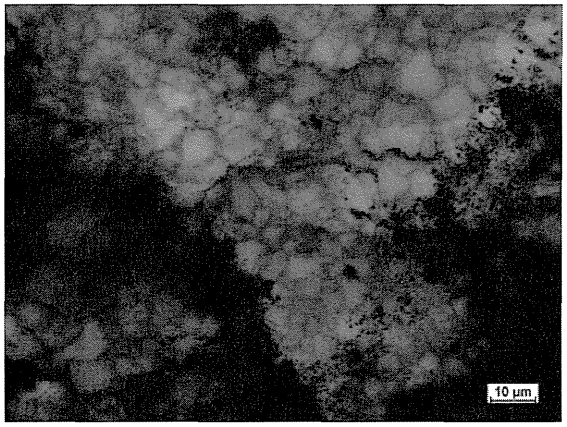

Figure 2. Polycrystalline ringwoodite assemblages in the shock vein of NWA 5011. The dark blue thin lines are related to grain boundaries.

The vein matrix consists of majorite-pyrope solid solution. The mineral analysis showed increased contents of Al and Na, which evidences the crystallization from a high-pressure melt. The larger fragments with low Al and Na-contents are majorite which transformed from low-Ca pyroxenes by solid-state transformation during the shock. The majorite chemical composition is similar to low-Ca pyroxene, present in the chondritic part (En_{75} Fs_{23} Wo_2). In edge region of the vein, where the cooling process was significantly faster than in the internal parts of shock veins, the pyroxene transformed to $MgSiO_3$-ilmenite (akimotoite) (Fig. 3).

The high-pressure polymorph of plagioclase was found in shock veins of NWA 5011. The chemistry of lingunite was similar to maskelynite grains (Ab_{80} An_{16} Or_4) (Fig. 4). The Raman spectrum shows the following peaks: 765 and 625 cm^{-1}, and a broadened band around 480 cm^{-1}, which is related to albite glass. The 922 and 594 cm^{-1} peaks are related to majorite vibrational modes (Fig. 4).

Conclusion: The pressure and temperature regimes in the shock veins of NWA 5011 meteorite were estimated based on the occurence of high-pressure phases. The presence of ilmenite structure pyroxene and Na-hollandite shows that crystallization pressure spike could reach slightly above 20 GPa. However, because of the lack of decomposition products the crystallization pressure probably not reached 23 GPa, where the ringwoodite, majorite and lingunite are getting instable. The crystallization temperature was around 1800°C [6]. No back-transformation of high-pressure phases took place, therefore the cooling rate has had to be between 8000-10000°C·s^{-1} [6]. This indicates that high-pressure phases were immediately frozen after pressure release.

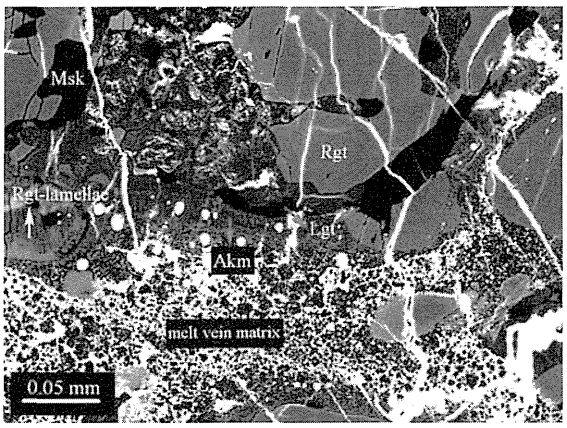

Figure 3. BSE-image of high-pressure phases along the shock vein.

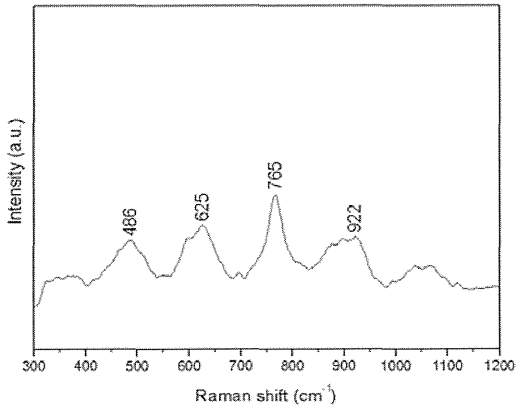

Figure 4. Raman spectrum of Na-hollandite from NWA 5011 (765 and 625 cm^{-1}). The 922 cm^{-1} peak is related to majorite, and the 486 cm^{-1} one to albite glass.

Acknowledgements: Authors are grateful to Prof. Paul F. McMillan (University of College London, UK.), and Prof. Bruno Reynard (Laboratoire de Sciences de la Terre, Lyon, France) for helpful suggestion concerning the work. Special thanks for Zsolt Bendő and Dr. Csaba Szabó (University of Loránd Eötvös, Budapest, Hungary) for the use of analytical instruments.

References: [1] Xie et al., (2001) LPSC XXXII, (abstract), #1805. [2] Sharp T.G. and DeCarli P.S. (2006) In Meteorites and Early Solar System II. [3] Taran et al., Phys. and Chem. of Minerals, 36, 4, 217-232. [4] Kiefer et al., (1999) Am. Mineral.., Vol. 84, 288-293. [5] Piriou B. and McMillan P. (1983) Am. Mineral.., Vol. 68, 426-443. [6] Chen et al., (1998) Science in China, Vol. 41, 522-528.

U–Pb Isotope Systematics of Baddeleyite: Implications for Crystallization Age of Shergottites.

T. Niihara[1], K. Misawa[1,2], H. Kaiden[1,2], T. Sekine[3*], and T. Mikouchi[4], [1]Dept. of Polar Sci., The Graduate Univ. for Advanced Studies, 10–3 Midori-cho, Tachikawa, Tokyo 190–8518, Japan (niihara@nipr.ac.jp), [2]Antarctic Meteorite Research Center, National Institute of Polar Research, 10–3 Midori-cho, Tachikawa, Tokyo 190–8518, Japan, [3]National Inst. for Materials Sci., Tsukuba, Ibaraki 305–0044, Japan. [4]Univ. of Tokyo, Hongo, Tokyo 113–0033, Japan. (*Present address: Hiroshima Univ., Higashi Hiroshima, Hiroshima 739–8526, Japan)

Introduction: Numerous isotope data from different isotope systems have been obtained from shergottites. Herd et al. [1, 2] and Misawa and Yamaguchi [3] obtained young U–Pb ages of <200 Ma from baddeleyite by in situ analyses using MC-ICP-MS and SHRIMP II, respectively. Bouvier et al. [4, 5] obtained old Pb–Pb ages of ~4.1 Ga and young Rb-Sr and Lu-Hf ages of ~200 Ma, and suggested that young ages of shergottites reflect resetting by aqueous alteration or by shock metamorphism. Nyquist et al. [6] determined Rb–Sr and Sm–Nd ages of a basaltic shergottite, NWA 1460, and concluded that the Rb–Sr and Sm–Nd ages were not reset by shock metamorphism.

Baddeleyite (ZrO_2) is an important phase in shergottites for U–Pb age determination. Zirconia (ZrO_2) crystallizes in monoclinic baddeleyite structure under pressure of ~4 GPa and temperature of ~1000 °C [7], and transforms to a tetragonal and then to a cubic fluorite structure at high temperatures. Baddeleyite is stable at ~4 GPa in the phase diagram, and, by compression, monoclinic baddeleyite shows sequential transition to two orthorhombic phases up to 70 GPa [7]. In order to investigate shock and heating effects on U–Pb isotope systematics of baddeleyite during shock metamorphism, we undertook shock recovery and heating experiments on baddeleyite.

Samples and Techniques: Shock-recovery experiments were performed using a single-stage 30 mm-bore propellant gun at the National Institute for Materials Science, Japan [8]. We used coarse-grained baddeleyites (200–250 μm in size) from Phalaborwa, South Africa, (2059.8 Ma) for starting materials. The baddeleyite is mixed with a coarse-grained terrestrial basalt sample, S690–7a, from North Kona, Hawaii [9] with a weight ratio of 1:2. The mixture was encapsulated in a cylindrical container made of SUS304 stainless steel and pressed at 29 MPa. We performed four experiments under different shock pressure conditions at 24, 34, 47, and 57 GPa. Porosity of the samples before the shock experiments was 26–30%. Heating experiments were performed using a vertical gas-mixing furnace at the Univ. of Tokyo. A sample experimentally shocked at 47 GPa was cut in a rectangle shape (5–8 × 2 × 2 mm in size and 17–40 mg in weight) and put on a Pt boat and heated at 1300 °C for 1 hr, and 1000 °C for 3 and 6 hrs under log fO_2 of IW +2.5 fixed with CO_2–H_2 mixture. Run products were quenched at room temperature.

Textures of the run products were examined by a scanning electron microscope (SEM; JEOL JSM–5900LV). Chemical compositions of constituent minerals were analyzed by an electron probe micro analyzer (EPMA; JEOL JXA–8200). In situ U–Th–Pb isotope analysis was carried out using a polished section with the SHRIMP II ion microprobe at NIPR [10]. An oxygen primary beam (O_2^-) of ~2 nA was focused on a spot with a diameter of ~10 μm. Standard baddeleyite samples, Phalaborwa and FC1 (1099.1 Ma) from Duluth Complex, Minnesota, and SL13 zircon were used for age and elemental concentration references, respectively.

Results:

SEM observation

A starting material, S690–7a [9], showed an intersertal texture with olivine phenocrysts (~400 μm in size; $Fa_{9–23}$) and finer-grained matrices of pyroxene ($Fs_{12–34}$), plagioclase ($An_{55–67}$) and glasses. Textures of the matrices of shocked samples at 24, 34, and 47 GPa did not change from those of the unshocked basalt. Olivine and baddeleyite grains in each shocked sample were irregularly fractured. The matrices were partly melted at the shock pressures of 34 and 47 GPa. Numerous vesicles (~10–40 μm in diameter) were observed in the 47 GPa sample. Matrices were totally melted at the pressure of 57 GPa.

In samples heated at 1000 °C for 3 and 6 hrs, olivine and baddeleyite grains were not melted. Numerous vesicles were observed in matrices of both of heated samples. Basalt was totally melted and baddeleyite was slightly melted at the rim of grain heated at 1300 °C. Fine-grained (~10–20 μm in size) euhedral zircon crystallized from melt, sometimes containing baddeleyite inclusions.

Chemical compositions of olivine

Olivine phenocrysts in S690–7a basalt sample (starting material) show heterogeneous compositions ($Fa_{8–22}$; PMD=14) with igneous FeO, MgO, and CaO zonings. Compositions of olivines shocked at 24, 34, 47 and 57 GPa were $Fa_{9–19}$ (PMD=18), $Fa_{9–30}$, (PMD=19), $Fa_{9–21}$ (PMD=19), and $Fa_{9–14}$ (PMD=2), respectively. Chemical zonings of olivines shocked at 24, 34, and 47 GPa were well preserved. In the 57 GPa sample, FeO, MgO and CaO zoning profiles of olivine were disappeared (Fig.1).

Olivine compositions of heated samples at 1000 °C for 3 and 6 hrs after shocked at 47 GPa are Fa_{8-14} (PMD=7) and Fa_{5-13} (PMD=14), respectively. Igneous zoning profiles of olivine were disturbed in the heated samples.

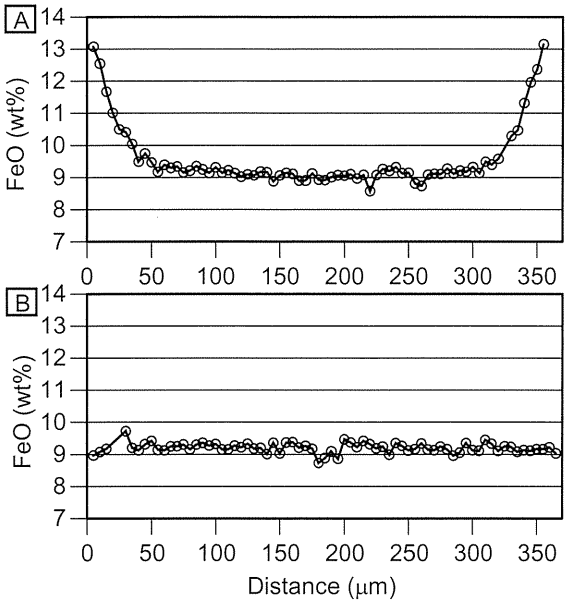

Fig.1. FeO zoning profiles of olivine phenocrysts. A: starting material (S690–7a). B: Experimentally shocked at 57 GPa.

U–Pb isotope systematics

There is no correlation between shock pressures and degrees of discordancy. Lead loss from baddeleyite was observed for none of the experimentally shocked samples, suggesting that the shock pressures up to 57 GPa do not measurably affect U–Pb isotope systems of baddeleyite [11, 12]. The U–Pb data of the heated baddeleyites are plotted on concordia diagrams (Fig. 2). The U–Pb isotope data for the samples heated at 1000 °C for 3 hrs and 1300 °C for 1 hr show slightly reverse discordant relative to the starting material (experimentally shocked at 47 GPa). This discordancy may have come from crystal orientation effects on baddeleyite during isotope measurements [13], and/or loss of U (or gain of Pb) during heating. On the other hand, Pb loss from baddeleyite was not observed for any heated samples.

Discussion: Young ^{238}U–^{206}Pb ages of ~200 Ma were presented for baddeleyite in Zagami and NWA 856 without the evidence on phase transition [2]. Jones discussed age significance of shergottites on the basis of petrology [14]. All major mineral phases, olivine and pyroxene, in shergottites yet preserve igneous zoning trends. There are several experimental data on internal Fe–Mg diffusion [15–17]. Miyamoto et al. [18] compared previously reported values and concluded that Misener [15] gives the best fit to the observed Fe–Mg zoning profiles. Data for Pb diffusion was reported for several radiogenic Pb-bearing minerals such as zircon, monazite, titanite, and rutile [e.g. 19]. The Fe–Mg internal diffusion

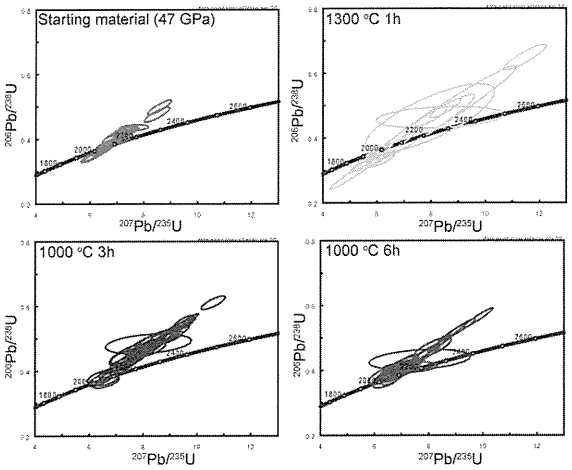

Fig.2. Concordia diagrams for experimentally heated samples.

rate is much faster than that of Pb.

The U–Pb and Pb–Pb ages of shocked and heated baddeleyites are indistinguishable from those of unshocked baddeleyite within errors except minor Pb-loss from the baddeleyite shocked at 57 GPa and heated for 1h at 1300 °C. Our experimental results indicate that it is hard to completely rest U–Pb isotope systematics of baddeleyite in Martian meteorite by shock events below ~60 GPa, although the duration of peak shock-pressure and grain size of baddeleyite in this study are different from the nature of basaltic shergottites.

Conclusion: The shock pressures up to 57 GPa and heating up to a partial-melting temperature (1300 °C) do not severely disturb U–Pb systems of baddeleyite, suggesting that U–Pb systematics of baddeleyite in shergottites give crystallization ages of Martian volcanic rocks. To understand the age significance of shergottites, it is necessary to analyze large baddeleyite grains (>10 μm) for in situ U–Th–Pb isotope analysis to avoid grain boundary contamination.

References: [1] Herd C. D. K. et al. (2007) *LPSC* **XXXVIII**, Abstract #1664. [2] Herd C. D. K. et al. (2010) *LPSC* **XXXXI,** Abstract #2280. [3] Misawa K. and Yamaguchi A. (2007) *MAPS* **42**, A108. [4] Bouvier A. et al. (2005) *EPSL* **240**, 221–233. [5] Bouvier A. et al. (2008) *EPSL* **266**, 105–124. [6] Nyquist L. E. et al. (2001) *Space Sci. Rev.* **96**, 105–164. [7] Ohtaka O. et al. (2001) *Phys. Rev. B* **63**, 174108-1–174108-8. [8] Sekine T. et al. (1987) *J. Material. Sci.* **22**, 3615–3619. [9] Yokose H. et al. (2005) *Marine Geol.* **219**, 173–193. [10] Misawa K. et al. (2005) *GCA* **69**, 5847–5861. [11] Niihara T. et al. (2009) *LPSC* **XXXIX**, Abstract #1562. [12] Niihara T. et al. (2009) *MAPS* **44**, A157. [13] Wingate M. T. D. and Compston W. (2000) *Chem. Geol.* **168**, 75–97. [14] Jones J. (1986) *GCA* **50** 969–977. [15] Misener D. J. (1974) *Carnegie Inst. Washington Publ.* **634**, 117–129. [16] Buening D. K. and Buseck P. R. (1973) *JGR* **78**, 6852–6862. [17] Chakraborty S. (1997) *JGR* **102**, 12,317–12,331. [18] Miyamoto M. et al. (2002) *AMR* **15**, 143–151. [19] Cherniak D. J. (2000) *Contrb. Mineral. Petrol.***139**, 198–207.

Implications for Lunar Crustal Evolution from Y-86032 and Dho 908. L. E. Nyquist [1,7], C.-Y. Shih[2], Y. D. Reese[3], J. Park[4,5], D. D. Bogard[1], D. H. Garrison[2], A. Yamaguchi[6], and K. H. Joy[4,7,8]. [1]KR/NASA Johnson Space Center, Houston, TX 77058. E-mail: laurence.e.nyquist @nasa.gov. [2]ESCG Jacobs-Sverdrup, Houston, TX 77058. [3]Mail Code JE-23, ESCG/Muniz Engineering, Houston, TX 77058. [4]Lunar and Planetary Institute, 3600 Bay Area Blvd. Houston, TX 77058, [5]NASA-MSFC, Huntsville, AL 35812 & Univ. Alabama @ Huntsville, 35805, [6]National Institute of Polar Research, Tachikawa, Tokyo, 190-8518, Japan. [7]Center for Lunar Science and Exploration, NASA Lunar Science Institute. [8]Mineralogy Department, The Natural History Museum London, Cromwell Road, London, SW7 5BD, UK.

Introduction:

We have studied anorthositic clasts in the Y-86032 and Dhofar 908 meteorites by the Rb-Sr, Sm-Nd, and ^{39}Ar-^{40}Ar techniques [1,2,3] combining isotopic studies with mineralogical/petrological studies of the same clasts. As a result of these studies, we conclude that the lunar crust is composed of a variety of anorthosites, at least some of which must have formed as plutons in the earliest formed ferroan anorthosite crust.

Sm-Nd data for lunar anorthosites:

Several of the anorthositic clasts that we have studied were too small to contain mafic minerals in sufficient abundance for determination of internal Sm-Nd or Rb-Sr isochrons. We combine bulk ("whole rock") Sm-Nd data with ^{39}Ar-^{40}Ar ages to estimate initial $^{143}Nd/^{144}Nd$ for them. It is widely assumed that ferroan anorthosites (FANs) formed as flotation cumulates on a global lunar magma ocean (LMO). A corollary is that all FANs are approximately contemporaneous and formed with the same initial $^{143}Nd/^{144}Nd$ ratio. Indeed, a whole rock isochron for selected FANs (and An93 anorthosite) [4] yields an isochron age of 4.42±0.13 Ga and initial $^{143}Nd/^{144}Nd$, expressed in ε-units, of $\varepsilon_{Nd,CHUR}$ = 0.3±0.3 relative to the CHondritic Uniform Reservoir [5] or $\varepsilon_{Nd,HEDPB}$ =-0.6±0.3 relative to the HED Parent Body [6]. These values are in good agreement with the age (T) = 4.47±0.07 Ga, and $\varepsilon_{Nd,HEDPB}$ =-0.6±0.5 for FAN 67075 [1,4]. The old Sm-Nd age and concordant Rb-Sr age [1] updated to 4.47±0.07 Ga make 67075 an outstanding candidate to have been a magma ocean flotation cumulate [3,4].

Fig. 1 compares the whole rock Sm-Nd data for anorthositic clasts from Y-86032 and Dho 908 to the ~4.42 Ga isochron (dotted line) and whole rock Sm-Nd data for 67075. An isochron (solid line) is drawn through the data for whole rock (WR), plagioclase (Plag), and pyroxene (Px) separates for FAN clast Y86032,133 [2] plus WR data for Dho908, which fits well with the Y86032,133 data. Together they give an age of 4.31±0.07 Ga and $\varepsilon_{Nd,HEDPB}$ =0.3±0.4. The isochron thus formed lies above the reference ~4.42 Ga isochron, and excludes the data for two bulk samples of 67075, and also the data for Y86032,44 FAN and Y86032,28 LG An93 anorthosite that has initial Nd- and Sr-isotopic systematics that are identical to those for FANs [1,4].

The age and initial Nd-isotopic parameters are shown more clearly with the aid of a (T, ε_{Nd}) diagram (Fig. 2). This diagram shows that although much of the Sm-Nd data are consistent with evolution from $\varepsilon_{Nd,HEDPB}$ =0 at the beginning of the solar system 4568 Ma ago with chondritic $^{147}Sm/^{144}Nd$ (μ) = 0.1967 (shown by the ε_{Nd} =0 line), other data require either higher or lower values of μ. A simplified scenario for those data is (a) evolution from initial values (T, ε_{Nd}) = (4568 Ma, 0) to the 67075 values (4470 Ma, -0.6) (period of lunar formation followed by the LMO) with μ ~0.12, (b) formation of sources for anorthositic plutons in the early lunar crust with μ in the range ~0.12 – 0.33. Such μ-values are plausible extreme values and are similar to values for plagioclase and pyroxene crystallized from 67075.

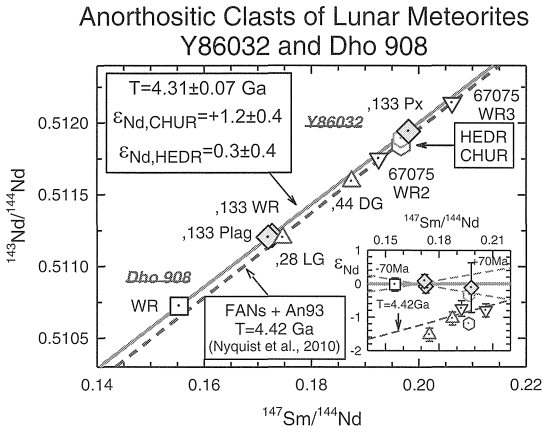

Fig. 1. Whole rock Sm-Nd data for anorthositic clasts in Y86032 and Dho 908 compared to those for FAN 67075.

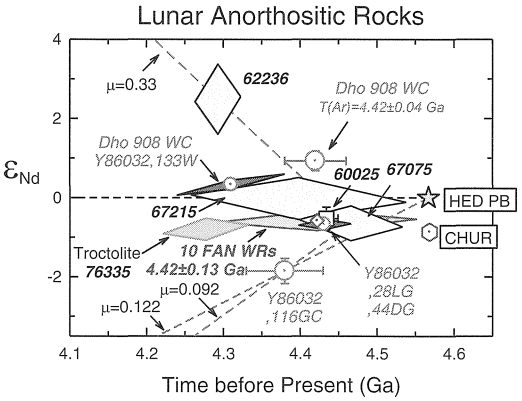

Fig. 2. (T, ε_{Nd}) diagram for lunar anorthosites, anorthositic clasts, and troctolite 76335.

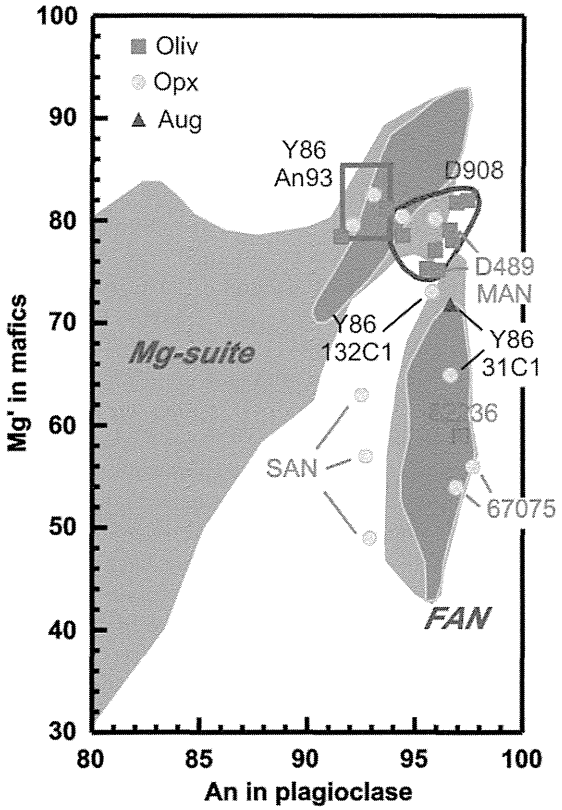

Fig. 3. Mg' vs. An for clasts in Y86032 and Dho 908. Adapted from [2]. Oval encloses new data for Dho 908, including a magnesian anorthosite, a troctolite (far left in oval), a spinel troctolite, and troctolitic anorthosites. K. Joy, analyst.

Mg' vs. An relationships for lunar anorthosites:

Fig. 3 illustrates that not only are the Nd-isotopic data for lunar anorthosites diverse, but their mineral compositions are diverse as well. It illustrates the composition of pristine FANs 67075 and 62236, pristine fragments of magnesian anorthosite [7] (MAN), the composition of some clasts in Y-86032 (labeled Y86NCn), sodic anorthosites [8] (SAN), and the reconstructed composition of An93 anorthosite [2] against the fields for lunar pristine rocks of the FAN and Mg-suites [2]. Also shown are new data for lithic clasts in PTSs P13288 and P13289 of Dho 908. These clasts range in size from ~100x120 μm to ~1.5x1.6 mm. They represent a suite of lunar crustal rocks including magnesian anorthosite (MAN), troctolitic anorthosites, a troctolite, and a spinel troctolite.

The Dho 908 White Clast (WC) analysed isotopically was metamorphosed, and Mg' could not be reliably obtained from sparse pyroxene inclusions within it which may be of metamorphic origin. The FeO contents of those pyroxenes suggest that the parent rock was a FAN, but that is uncertain. Among the small lithic clasts, none of the analysed mafics had Mg'<~75, characteristic of magnesian anorthosites (MAN, [7]). These data show that the lunar crust was quite magnesian where the Dho 908 meteorite came from. Its composition apparently

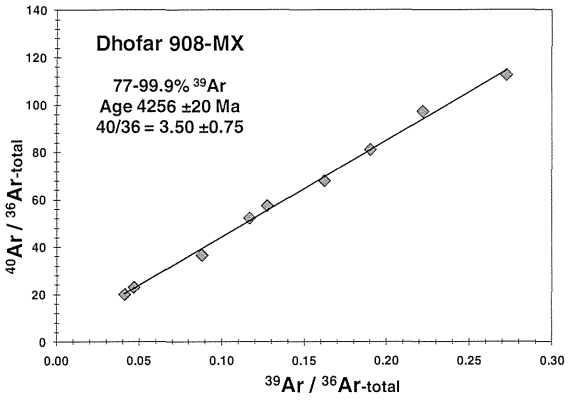

Fig. 4. ^{39}Ar-^{40}Ar isochron plot for Dho 908 matrix.

corresponded to Mg' values intermediate to those of FANS and plutonic Mg-suite rocks.

^{39}Ar-^{40}Ar age of Dho 908 matrix:

Fig. 4 shows an ^{39}Ar-^{40}Ar isochron plot for Dho 908 matrix. A precise age of 4256±20 Ma was obtained from the high-temperature extractions after correction for trapped solar wind Ar and lunar atmosphere ^{40}Ar with combined ^{40}Ar/^{36}Ar = 3.5±0.75. The presence of trapped Ar shows that the matrix had some exposure in the lunar regolith. The matrix is dominantly troctolitic, and the ^{39}Ar-^{40}Ar age obtained from it is typical of that of lunar troctolites (*cf.* 76335 in Fig. 2), further indication of a magnesian crustal composition.

Conclusions:

The crystallization ages and Nd isotopic compositions of the majority of FANs appear to be consistent with the LMO hypothesis if the lunar initial ^{143}Nd/^{144}Nd ratio was the same as for the parent body of the HED meteorites. However, our study of Y-86032 tells us that other anorthositic compositions satisfy this criterion as well, and having a FAN composition doesn't guarantee an LMO origin. Anorthositic plutons probably are present in the lunar crust. The earliest crust probably underwent complex petrogenetic processes. Further studies are needed to place the full array of lunar anorthosites into a comprehensive picture of lunar crustal evolution. Reliably determining the crystallization age and Nd-isotopic composition of magnesian anorthosites (MAN) could provide an important new constraint on lunar crustal evolution.

References: [1] Nyquist L. et al. (2006) *Geochim. Cosmochim. Acta, 70,* 5990-6015. [2] Yamaguchi A., et al. (2010) *Geochim. Cosmochim. Acta,* in press. [3] Nyquist L. E. et al. (2010) *41st Lunar and Planetary Science Conference, Houston, TX, Abstract #1383.* [4] Nyquist L. E. et al. (2010) Papers presented to the Global Lunar Conf., Beijing, May 31-June 3, 2010. [5] Jacobsen S. B. and Wasserburg G. J. (1984) *Earth Planet. Sci. Lett. 67,* 137-150. [6] Nyquist L. E. et al. (2004) *Antarct. Met.* **XXVIII,** 66-67. [7] Takeda H. et al. (2006) *Earth Planet. Sci. Lett. 247,* 171-184. [8] Norman M.D. and Taylor S.R. (1992) *Geochim. Cosmochim. Acta 56,* 1013-1024.

Al-Mg Dating of Anorthite Grain in Chondrules of CV3 Chondrite.

Y. Ota[1], Y. Sano[1], N. Takahata[1], N. Sugiura[2] and W. Fujiya[2].
[1]Atmosphere and Ocean Research Institute, The University of Tokyo, y_ohta@aori.u-tokyo.ac.jp. [2]Department of Earth and Planetary Sciences, The University of Tokyo.

Introduction

In order to study the formation interval between Ca-Al-rich inclusions (CAI) and chondrules in carbonaceous chondrites, extinct nuclides such as ^{26}Al, ^{41}Ca are useful. There are principally two analytical methods to detect their decay products such as ^{26}Mg, and ^{41}K. The first one is in situ analysis by using secondary ion mass spectrometry (SIMS) and the second is multi-collector inductively coupled plasma mass spectrometry (MC-ICP-MS) together with a successive procedures of micro-drilling, chemical digestion and separation. The former has an advantage of high spatial resolution down to 5 micro-meter but the analytical precision is not generally as good as that of thermal ionization mass spectrometry (TIMS). The latter shows a high precision equivalent with TIMS but the spatial resolution is significantly poor. Recently a NanoSIMS NS50 ion microprobe with a supreme lateral resolution has been developed by Cameca and applied to the field of cosmochemistry. It is well documented that a CAI of CV chondrite shows one of the oldest Pb-Pb ages (4567.2 Ma) [1], while there are still not enough data of chondrule ages [2]. Here we report ^{26}Ar-^{26}Mg dating of a single anorthite grain located in a chondrule of the Efremovka and Sahara98044 meteorite by using the NanoSIMS installed at Atmosphere and Ocean Research Institute, The University of Tokyo.

Experiment

Thin sections of Efremovka and Sahara 98044 were set in a sample holder together with standard anorthite (Miyake-jima) and olivine (San Carlos) and carbon coated to dissipate charge during analysis. The positions of anorthite grains in the chondrule are determined by using a scanning electron microprobe before SIMS analysis. Three grains of anorthite in one chondrule of Efremovka and two grains of anorthite in one chondrule of Sahara98044 were measured. The samples were evacuated in the air-lock system of NanoSIMS to reduce water absorbed on the mount. Using a critical illumination mode, a ~500 pA mass filtered O^- primary beam was used in the case of anorthite grains to sputter a 3~5 micron meter diameter crater and secondary positive beams were extracted for mass analysis using a Mattauch-Herzog geometry. Before the actual analysis, the sample surface was rastered for 3 min in order to reduce the surface contaminant elements. We detected $^{27}Al^{++}$ (a secondary electron multiplier detector called EM#1) at mass 13.5, $^{24}Mg^+$ (EM#2) at 24, $^{25}Mg^+$ (EM#3) at 25 and $^{26}Mg^+$ (EM#4) at 26 at the same time under a static magnetic field. A mass resolution of 7000 (Cameca definition) was attained for separating $^{24}Mg^+$ from $^{48}Ca^{++}$ with adequate flat topped peaks. The Mg sensitivity of 100 cps/1nA/ppm was obtained by an intensity of ^{24}Mg ion beam and abundance of Mg in the standard anorthite. In order to obtain accurate Mg isotopic ratios, we have also measured Mg isotopes (^{24}Mg, ^{25}Mg, ^{26}Mg) using a EM#3 detector by a magnet scanning mode. In the case of olivine samples, at first, we used a primary of 1 pA and detected Mg isotopes by the same multi-collection system. However we have observed undesirable isotope fractionations probably due to Quasi Simultaneous Arrival (QSA) effect [3]. In order to avoid the effect, we used a primary of 10 nA and detected Mg isotopes by a single Faraday cup with a magnetic scanning mode. Abundance of ^{27}Al in olivine samples was less than the detection limit of the Faraday cup.

Results and Discussion

The δ^{25}Mg values of Miyake-jima anorthite (^{25}Mg/^{24}Mg ratios in delta notation) ranged from -24‰ to -30‰, while the δ^{26}Mg values ranged from -48‰ to -60‰, suggesting a typical mass dependent fractionation with a slope 2. On the other hand, 5 spots in a single anorthite grain (about 25 x 10 micro meter) in an Efremovka chondrule showed apparent excess ^{26}Mg. The δ^{25}Mg values of San Carlos olivine and Efremovka chondrule olivine ranged from -3‰ to +8‰, though they are located on the mass dependent fractionation line in a three isotope plot. Thus there is no excess ^{26}Mg in both terrestrial and extraterrestrial olivine samples.

Apparent excess ^{26}Mg was observed in a relatively small anorthite grain (#1) of the Efremovka chondrule. There is a positive correlation between the Al/Mg ratio and the excess ^{26}Mg, leading to a typical ^{26}Al-^{26}Mg isochron with the initial ^{26}Al/^{27}Al ratio of $(3.4 \pm 1.1) \times 10^{-6}$. When we assume the initial ratio of $(4.63 \pm 0.44) \times 10^{-5}$ in the Efremovka CAI, the formation interval is calculated as $2.64^{+0.55}_{-0.36} \times 10^6$ year. On the other hand, excess ^{26}Mg in the larger anorthite grains (#2 and #3) are smaller and there is not a correlation between the Al/Mg ratio and excess ^{26}Mg. It has been well established that any anorthite in a single chondrule show the same origin. It is the basis that one may draw the ^{26}Al-^{26}Mg isochron based on the spot analysis of different grains in the same chondrule by using SIMS. However we show that there is a substantial difference between the initial ^{26}Al/^{27}Al ratios of grain by grain.

We report also ^{26}Al-^{26}Mg age of a single anorthite grain in Sahara98044. We have measured two anorthite grains in one chondrule of Sahara98044. Eight spots were measured in grain#1 and seven spots were measured in grain#2. In addition we have measured the data of pyroxene. Both grains show that there is an apparent positive correlation between the Al/Mg ratio and the excess ^{26}Mg, leading to a typical ^{26}Al-^{26}Mg isochron with the initial ^{26}Al/^{27}Al ratio of $(4.1 \pm 2.2) \times 10^{-6}$(grain#1), $(8.3 \pm 3.5) \times 10^{-6}$ (grain#2). When we assume the initial ^{26}Al/^{27}Al ratio of $(5.3 \pm 0.1) \times 10^{-5}$ in Sahara98044 CAI, the formation interval are calculated $2.12^{+0.44}_{-0.80} \times 10^{6}$ year(grain#1), $2.64^{+0.36}_{-0.57} \times 10^{6}$ year (grain#2). In this analysis these two ages are consistent within the error bar. There is some possibility that these two grains are formed at the same time.

References:

[1] Amerin Y. et al. (2002) Science, 297, 1678-1683. [2] Hutcheon I.D. et al. (2009) GCA, 73, 5080-5099. [3] Slodzian G. et al. (2004) ASS, 231-232, 874-877.

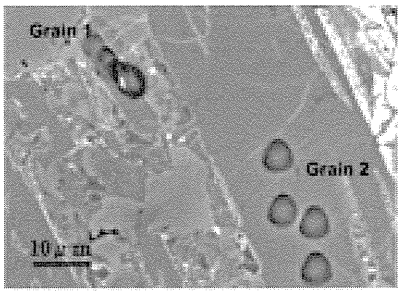

The photo of Efremovka grain#1,2

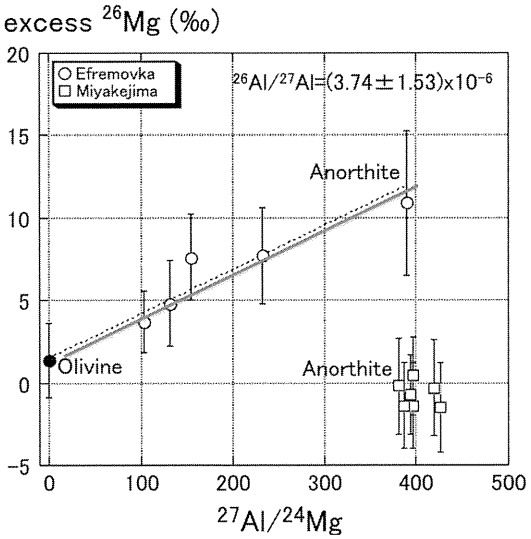

The isochron of Efremovka grain#1

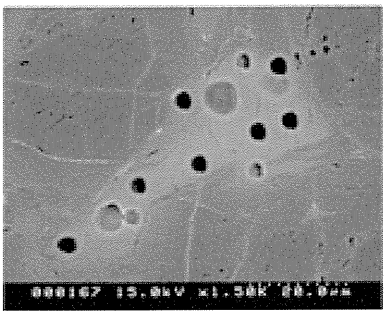

The photo of Sahara98044 grain#1

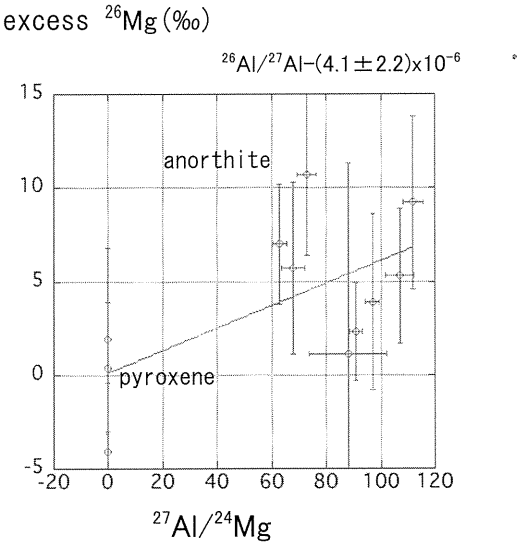

The isochron of Sahara98044 grain#1

^{39}Ar-^{40}Ar Studies of Lherzolitic Shergottites Yamato 000097 and 984028. J. Park[1,2,3], L. E. Nyquist[2], D. D. Bogard[2], D. H. Garrison[4], C.-Y. Shih[5], T. Mikouchi[6] and K. Misawa[7], [1]Lunar and Planetary Institute, 3600 Bay Area Blvd, Houston, TX 77058, USA, [2]ARES, Mail Code KR, NASA Johnson Space Center, Houston, TX 77058, USA, [3]Current address: Space Science Office, NASA Marshall Space Flight Center, Huntsville AL 35812, and University of Alabama in Huntsville, Huntsville AL 35805, USA, [4]ESCG/Barrios Technology, Houston, TX 77058, USA, [5]ESCG/Jacobs Engineering, Houston, TX 77058, USA, [6]Department of Earth and Planetary Science, University of Tokyo, Bunkyo-ku, Tokyo 113-0033, Japan, [7]Meteorite Research Center, National Institute of Polar Research, 10-3 Midoricho, Tachikawa, Tokyo 190-8518, Japan.

Introduction:
Yamato 984028 (Y984028) was discovered by the Japanese Antarctic Research Expedition (JARE) in 1998 and recently classified as a lherzolitic shergottite with large pyroxene oikocrysts enclosing rounded olivine and chromites. It also contains shock veining and maskelynite [1]. Y984028 is paired with the more recent lherzolitic shergottite finds Y000027/47/97 based on similarities in mineralogy and chemistry (e.g., [2]), as well as isotopic composition (e.g., [3, 4]). We present here the studied ^{39}Ar-^{40}Ar of Y-984028 whole rock (WR) and pyroxene (Px), in order to gain better understanding of trapped Ar components with a comparison of the possibly-paired Y000097 Ar release.

Ar-Ar results:
^{39}Ar-^{40}Ar age spectra and K/Ca ratios for whole rock (WR) and pyroxene mineral separates of Y984028 and plagioclase mineral separates of Y000097 [5, 6] are shown in Figs. 1, 2 and 3. Age spectra for Y984028 WR and Px are roughly ~2 Ga, indicating several Ar components, such as radiogenic 40Ar*, cosmogenic Ar and trapped Ar from multiple minerals, as well as multiple source origins. The ^{39}Ar-^{40}Ar age for Y000097 gives ~260 Ma [5, 6]. The reported Sm-Nd and Rb-Sr ages for Y984028 are 170±10 Ma and 170±9 Ma, respectively [4]. Y000097 yields a Rb-Sr age of 147±28 Ma and a Sm-Nd age of 152±13 Ma [5]. Apparently, Ar-Ar ages of Y984028 and Y000097 show trapped Ar components. Fig. 4 shows K/Ca of mineral phases in Y984028 determined by electron microprobe. This gives mineral modes and we can compare the K/Ca ratios from the different techniques and discuss the relative importance of each mineral in the K budget of Y984028 WR and Px. Open boxes in Fig. 4 can be interpreted as the multiple mineral phases in the Ar-Ar whole rock data (Fig. 1), which are complicated to be distinguished. The mineral pyroxene spectra (Fig. 2), although nominally that of a single phases, show an order of magnitude more variation in K/Ca than does the Ar spectra in WR. As shown in Fig. 4, pyroxene shows a large range in K/Ca, but because opx has low modal abundance compared to pigeonite and augite, the K/Ca ratio pyroxene is effectively restricted to the range 0.0001 to 0.01, i.e., to the last ~20% of the ^{39}Ar release.

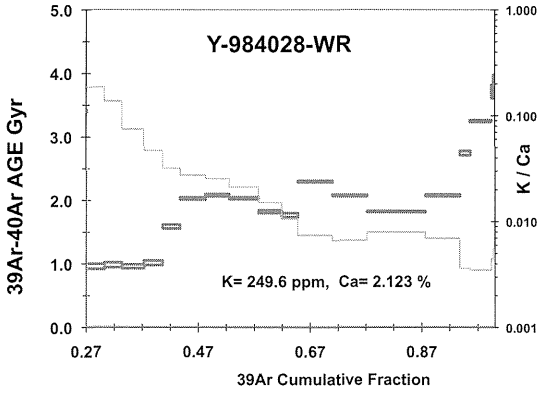

Fig. 1. ^{39}Ar-^{40}Ar ages and K/Ca ratio as a function of ^{39}Ar release for Y-984028 whole rock.

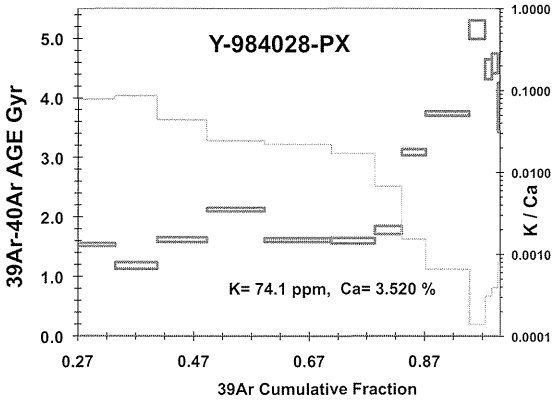

Fig. 2. ^{39}Ar-^{40}Ar ages and K/Ca ratio as a function of ^{39}Ar release for Y984028 pyroxene separate.

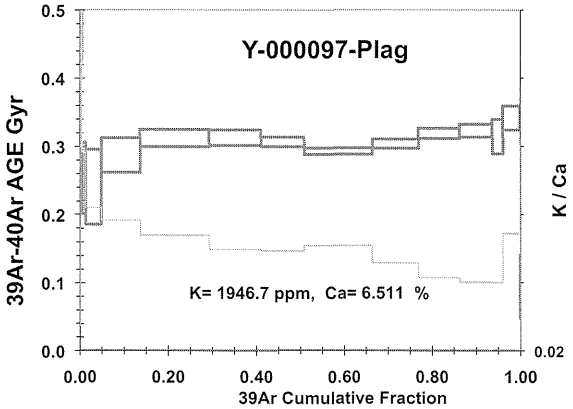

Fig. 3. ^{39}Ar-^{40}Ar ages and K/Ca ratio as a function of ^{39}Ar release for Y000097 plagioclase separate.

Besides, K/Ca ratio in Fig. 2 shows that the gas released during the first ~80% of the ^{39}Ar release must be from plagioclase (maskelynite) or olivine.

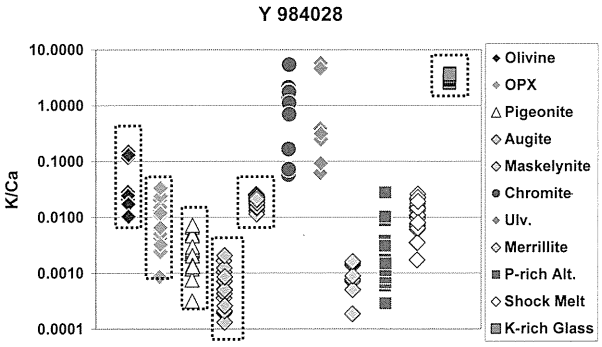

Fig. 4. K/Ca ratios for each minerals in Y984028.

Isochron plot for Y984028-Px:

Fig. 5 is the cosmogenic corrected $^{40}Ar/^{36}Ar_{(trapped)}$ versus $^{39}Ar/^{36}Ar_{(trapped)}$ of Y984028 pyroxene separate. Because we do not have an accurate way to determine the cosmogenic ^{36}Ar concentrations of the pyroxene, we used the minimum measured $^{36}Ar/^{37}Ar$ and an estimated value of cosmogenic ^{36}Ar of $1.9x10^{-9}$ cm^3STP/g, which is similar as $1.3x10^{-9}$ cm^3STP/g of Y984028 noble gas whole rock data [3]. The isochron slope of lower temperature extractions at 300-650 °C is consistent with an apparent age of ~170 Ma [4], with the similar initial $^{40}Ar/^{36}Ar$ of terrestrial atmosphere (~296). Intermediate temperature data (from 800-1100 °C), nominally consistent with a similar slope of the radiometric age of ~170 Ma [4] with an approximately Martian atmosphere trapped Ar composition with a ratio of $^{40}Ar/^{36}Ar$ as ~1800 [7]. Based on the K/Ca ratio, we know that ^{39}Ar released at both lower and intermediate temperatures is primarily from plagioclase and olivine. ^{39}Ar released at higher temperatures (1200-1500 °C) shows a higher slope, distinct from lower temperatures.

Isochron plot for Y000097-Plag:

Fig. 6 is the Y000097-Plag isochron plot of $^{40}Ar/^{36}Ar_{(trapped)}$ versus $^{39}Ar/^{36}Ar_{(trapped)}$ with multiple Ar-components; radiogenic, trapped Martian atmosphere, terrestrial atmosphere, inherited Ar. some of these components are more dominant in some gas fractions than others, making interpretation more complicated. Interestingly, we can find three isochron slopes with different ages. The slope at the lower temperature release (500-700 °C) gives an age of ~182 Ma, while most of the Ar released at intermediate temperatures (800-1200 °C), except the 1060 °C and 1110 °C fractions, gives a slope age of ~269 Ma, which is similar to the Ar age spectrum of Y000097. It is unclear why the 1060 °C and 1110 °C data differ, but it is plausible that these Ar releases have the presence of inherited, mantle ^{40}Ar, with a little higher initial $^{40}Ar/^{36}Ar$ ratio of ~627.

Discussions:

Ar isotopic components of Martian meteorites are complicated because they represent the sum of several Ar origins, such as Martian atmosphere, Martian mantle, inherited Ar, terrestrial atmosphere, and cosmogenic Ar. Obviously, Ar released at higher temperatures from pyroxene separates should not have any detectable signature of the terrestrial atmosphere. Reported analyses of $^{129}Xe/^{132}Xe$ from higher temperature extractions (1200-1800 °C) [3] give a value higher than the terrestrial Xe ratio of 0.98. We suggest the presence of Martian mantle ^{40}Ar, as well as excess ^{40}Ar assimilated from inherited magma [6, 8].

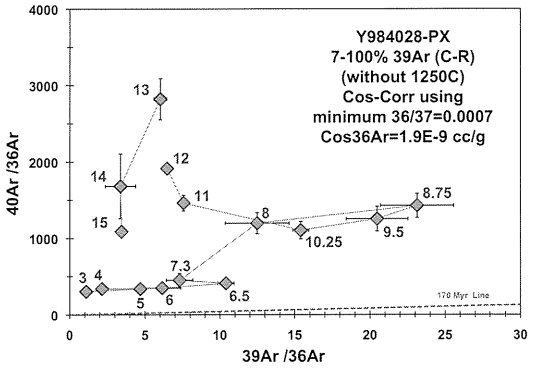

Fig. 5. $^{40}Ar/^{36}Ar$ *vs.* $^{39}Ar/^{36}Ar$ in Y984028 pyroxene separate.

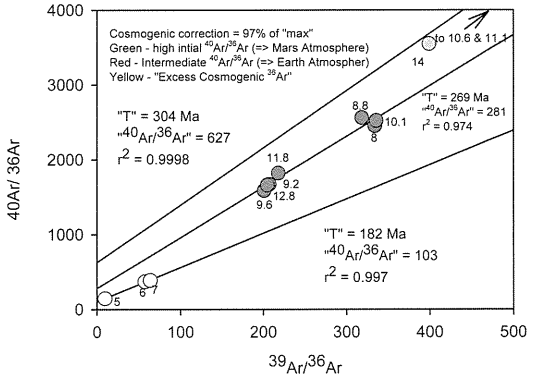

Fig. 6. $^{40}Ar/^{36}Ar$ *vs.* $^{39}Ar/^{36}Ar$ in Y000097 plagioclase separate.

References:

[1] Kojima H. and Kaiden H. (2008) *Meteorite Newsletter 17,* 1-5 (ed.). [2] Mikouchi T. et al., (2009) *Antarct. Meteorites*, XXXII, 35-36. [3] Nagao K. (2009) *Antarct. Meteorites*, XXXII, 43-44. [4] Shih C.-Y. et al., (2010) *Polar Science,* in press.[5] Misawa K. et al. (2008) *Polar Science, 2,* 163-174.[6] Bogard D. D. et al. (2009) *Meteorit. Planet. Sci., 44,* 905-923. [7] Bogard D. D. and Garrison D. H. (1998) *GCA, 61,* 1829-1835. [8] Bogard D. D. and Park J. (2008) *Meteorit. Planet. Sci. 43*, 1113-1126.

Petrogenetic Relationship of Geochemically-Enriched Shergottites as Inferred from MELTS Calculation. W. Satake, T. Mikouchi, and M. Miyamoto. Department of Earth and Planetary Science, Graduate School of Science, University of Tokyo, Hongo, Bunkyo-ku, Tokyo 113-0033, Japan (satake@eps.s.u-tokyo.ac.jp).

Introduction:

Shergottite is the largest group of Martian meteorites that crystallized at 160-550 Ma near the Martian surface as shallow intrusions or thick lava flows [e.g., 1]. Recent petrological and isotopic studies have revealed that shergottites show obvious correlations between oxidation state and geochemical characteristics and such correlation must have important information about their mantle sources and are directly relevant to Martian evolution [e.g., 2]. The difference in such geochemical characteristics can divide them into three subgroups: depleted, enriched and intermediate shergottites [e.g., 3]. Because samples in each group show generally similar crystallization and cosmic-ray exposure ages, there may be a petrogenetic relationship at least for some samples (Table 1). For example, the computational calculation using the MELTS program applied to depleted shergottites suggested that the bulk composition of Y984059 and Dar a Gani 476 could produce parent magmas of Dhofar 019 and QUE94201 by simple fractionation processes [4]. However, such sequential relationship has not been investigated for enriched shergottites. In our previous study we indicated that both NWA4468 and RBT04262 were derived from an oxidizing reservoir(s) by using synchrotron radiation (SR) Fe-XANES measurement of maskelynite [5]. This result is consistent with the observation that they are geochemically-enriched shergottites [6,7]. Because these enriched shergottites have more primitive compositions than other enriched shergottites, we investigated the formation sequence and relationship of enriched shergottites with MELTS calculation by using their estimated melt compositions.

Samples and methods:

We estimated the bulk compositions of the non-poikilitic areas in NWA4468 and RBT04262 by broad electron beam using electron microprobe (JEOL JXA-8900L). Then, we tested MELTS calculation using the obtained bulk compositions to explore the possibility to produce evolved enriched shergottites. MELTS is a software package designed to facilitate thermodynamic modeling of phase equilibria in magmatic system which provides the ability to compute equilibrium phase relations for igneous systems over the temperature range of 500-2000 °C and the pressure range of 0-2 GPa [8]. In this study, MELTS calculation was performed under 1 atm total pressure with the oxygen fugacity (fO_2) of log fO_2=QFM-1.0 that is the estimated fO_2 for enriched shergottites [e.g., 2,5].

Results and Discussion:

NWA4468 and RBT04262 are cumulate rocks that show similar petrography to lherzolitic shergottites [e.g., 9]. However, their non-poikilitic areas show obvious basaltic texture and appear to represent melt compositions. Therefore, we employed them as the starting melt composition of enriched shergottites. The obtained bulk compositions of the non-poikilitic areas in NWA4468 and RBT04262 are shown in Table 2. They have generally similar compositions as expected from their similar mineral compositions [6,7]. We calculated the residual melt compositions from the NWA4468 composition by assuming that crystallizing solids are removed from the system at each increment as reaction progresses.

Although most enriched shergottites are basaltic shergottites and they are obvious cumulates, Dhofar 378 and Los Angeles contain abundant plagioclase and are considered to be melt rocks whose bulk compositions represent their parent magma compositions [10,11] (Table 1). In this model, we thus assumed that the parent melts of both Los Angeles and Dhofar 378 may be produced from the residual melt of the non-poikilitic areas in NWA4468 and compared with the results from MELTS calculation. As shown in Figs. 1 and 2, atomic Fe/(Fe+Mg), CaO and Al_2O_3 of the non-poikilitic areas in NWA4468 are lower than those of Los Angeles and Dhofar378, and thus can be consistent with our assumption.

The results of MELTS calculation suggested that a similar composition to the bulk compositions of Los Angeles and Dhofar 378 could be produced at 1100 °C and 1090 °C, respectively from the non-poikilitic areas in NWA4468 although a few elements (e.g., Ca) show small discrepancy (Fig. 2 and Table 2). The NWA4468 composition gives better match than RBT04262 by the MELTS calculation. Since the estimate for the bulk composition of non-poikilitic areas in NWA4468 and RBT04262 have some errors, more appropriate estimate may lead even better match with Los Angeles and Dhofar 378.

Although this is a fairly rough estimate including some errors, this study demonstrates that NWA4468, RBT04262, Los Angeles and Dhofar378 may have been formed by the same magmatic event as they show similar crystallization and exposure ages (Table 1).

References:

[1] Nyquist L. E. et al. (2001) *Space Sci. Rev.*, *96*, 105-164. [2] Herd C. D. K. et al. (2002) *GCA*, *66*,

2025-2036. [3] Symes S. J. K. et al. (2008) *GCA*, *72*, 1696-1710. [4] Mikouchi T. and Koizumi E. (2008) *Meteorit. Planet. Sci.*, *42*, 5294. [5] Satake. W. et al. (2010) *LPSC XLI*, #1902. [6] Irving A. J. et al. (2007) *LPS XXXVIII*, #1526. [7] Anand M. et al. (2008) *LPS XXXIX*, #2173. [8] Ghiorso. M. S. and Sack. R. O. (1991) *Cont. Mineral. Petrol.*, *108*, 485-510. [9] Mikouchi T. and Kurihara T. (2008) *Polar Sci.*, *2*, 175-194. [10] Rubin A. E. et al. (2000) *Geol.*, *28*, 1011-1014. [11] Ikeda Y. et al. (2006) *Antarct. Meteorite Res.*, *19*, 20-44.

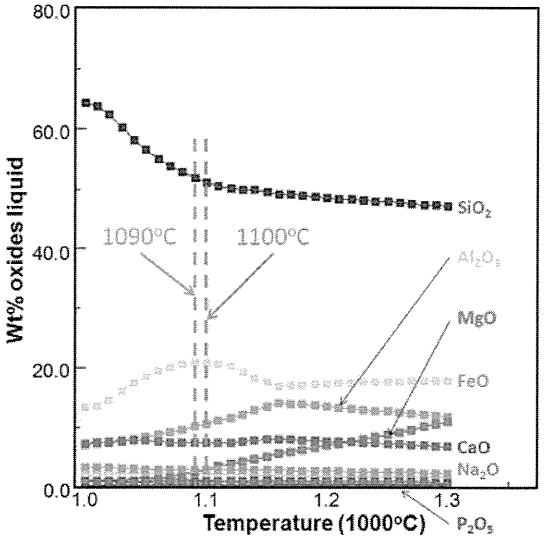

Fig. 1 Computed chemical composition of residual melt from the bulk composition of the non-poikilitic area in NWA4468 as a function of temperature. Total pressure is 1 bar, $\log f O_2$=QFM-1.0, assuming fractional crystallization.

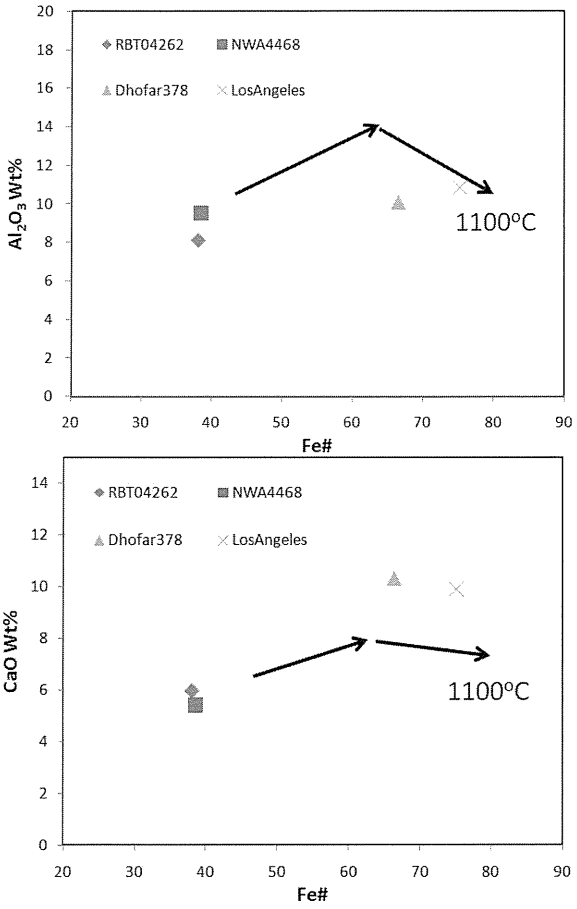

Fig. 2. Relation between Al_2O_3, CaO wt% and atomic Fe/(Fe+Mg) of estimated bulk compositions of RBT04262 and NWA4468 along with Dhofar 378, Los Angeles and residual melt .

Table 1. Petrological and chronological properties of enriched shergottites.

Sample	Petrological classification	Cummlate?	Atomic Fe / (Fe+Mg)	Crystallization age	Cosmic-ray exposure age
NWA1068	Olivine-Phyric	No	41	185±11 Ma	-
NWA4468	Lherzolitic	Yes	38	150±29 Ma	-
RBT04262	Lherzolitic	Yes	38	174±14 Ma	2.1 Ma
Dhofar378	Basaltic	No	66	157±24 Ma	0.79-1.19 Ma
Los Angeles	Basaltic	No	75	165±11 Ma	3.35±0.7 Ma
NWA856	Basaltic	Yes	51	186±24 Ma	-
Shergotty	Basaltic	Yes	54	165±11 Ma	3.05±0.5 Ma

Table 2. Estimated bulk compositions of the non-poiklitic areas in NWA4468 and RBT04262 along with 1100 °C residual liquid, Los Angeles, 1090 °C residual liquid and Dhofar 378 compositions.

	NWA4468	RBT04262	1100°C residual liquid	LosAngeles	1090°C residual liquid	Dhofar378
SiO_2	45.22	45.53	50.86	50.06	51.64	49.88
TiO_2	0.38	0.44	1.10	1.12	1.10	0.98
Al_2O_3	9.54	8.1	10.49	10.86	10.02	10.08
FeO	18.94	19.21	20.76	21.07	20.75	19.94
MnO	0.43	0.47	0.36	0.46	0.33	0.48
MgO	16.97	17.56	2.89	3.91	2.46	5.66
CaO	5.41	5.91	7.30	9.92	7.30	10.32
Na_2O	1.82	1.35	2.77	2.24	2.78	1.98
K_2O	0.17	0.15	0.41	0.36	0.45	0.17

Growth Textures of the NWA 4519 Ureilite with Reference to the Formation Processes.

H. Takeda[1], A. Yamaguchi[2] and M. Otsuki[3], [1]Dept. of Earth & Planet. Sci., Univ. of Tokyo, (Chiba Inst. of Technology, Forum Res.), [2]National Inst. of Polar Res., [3]Ocean. Res. Inst., Univ. of Tokyo,

Introduction:

Because of the discovery of the Almahata Sitta meteorite, which is the first example of the recovered asteroidal sample (2008TC_3 asteroid) [1], there are renewed interests in ureilites to understand the relationship between meteorite and its asteroidal parent body. 95 Antarctic ureilites were recorded among 240 total ureilite samples [2]. The magmatic origin of ureilites proposed early by Berkley et al. [3] and Goodrich et al. [4] us based largely on the mineral elongation lineation. They argued that the fabrics are characteristic of those formed by tabular minerals in a fluid laminar flow regime [4, 3]. Another model explained that such preferred orientation of mafic silicates was produced by a planetesimal scale collision and growth of crystals from an unmelted wall under a strong temperature gradient [5].

Although many Antarctic samples extended their compositional ranges of minerals and pyroxene phases, no new evidence of elongation texture has been found. We report unique textures of preferred orientation of mafic silicate crystals in Northwest Africa 4519 (hereafter "NWA 4519") [6] found in a hot desert, which seem to show new growth textures and chemical zonings of pyroxene indicating growth conditions. Then, we reexamine a model, in which important processes are crystal growth of mafic silicates in the presence of a little partial melt and removal of a part of such melt along grain boundaries [5].

Samples and Methods:

NWA 4519 has a deformed conical shape (114 g; 6.5 × 3.5 cm), and is partially fusion-crusted [6]. Two PTSs of NWA 4519 were made from different chips [6] from NIPR, and were examined by an optical microscope. One PTS of NWA 4519,2 has been studied by Electron probe micro-analyzer (EPMA) at Ocean Res. Inst. (ORI) of Univ. of Tokyo, and at NIPR. The area analysis technique of the JEOL 8900 EPMA at NIPR and ORI, was used to obtain elemental distribution maps, from which mineral distribution maps were derived.

Results:

NWA 4519 contains olivine and pyroxene with carbonaceous veins at grain boundaries. Compositions of Olivine (Fo_{83-80} [cores]; Fo_{89} [rims]) and pyroxene ($Ca_{8.6}Fe_{16.7}$) and oxygen isotopic compositions are within the ranges of the ureilites.

Growth Textures: Mafic silicate crystals seem to show a preferred orientation, two to three crystals up to 4.2 × 1.4 mm in size are joined with common elongation direction without carbonaceous veins to form a large aggregate (~4.2 × 3.8 mm) with carbonaceous materials around it (Fig.1 and 2). Mineral distribution map shows that olivine is more dominant than pyroxene (Fig. 3)

Chemical Zonings of Pyroxene: The elemental distribution maps of Mg and Ca of NWA 4519 show that enrichment of Ca at the top of an elongated pigeonite crystal (Fig. 3 and 4). The composition of this Ca-rich rim gives composition of augite $Ca_{37}Fe_5$

Discussion:

The texture of two to three crystals joined together without carbonaceous veins rule out the possibility of crystal sedimentation from the magma. This kind of texture is said to be produced by competitive crystal growth across the elongating crystals under strong temperature gradient along the elongation direction of crystals. A well known example is ice sheet covering a pond. Many acicular crystals of ice are grown perpendicular to the surface. The temperature of the surface of the pond is lower than the interior water. Many dusts floating on the surface of the pond may act as nucleation sites of the acicular crystals. Many such crystals grow perpendicular to the surface into the pond because of the temperature gradient. Because many crystals are growing competitively, the crystal will not grow perpendicular to the surface.

An experiment had been performed for crystal growth of packed olivine powders, with temperature gradient perpendicular to the wall of the furnace. Elongated olivine crystals are grown by grain coarsening with little melt between the grains. Such growth conditions may take place, when the ueilite parent body was heated by the planetessimal scale collisions.

A working hypothesis for the formation and evolution of the ureilite parent body involves high temperature episodes and a planetessimal scale collision, which might have facilitated compaction and recrystallization of mafic silicates [5]. During the episodes, Fe-Ni-S eutectic melt and a partial melt rich in Ca, Al, Fe, and Si might have been lost from a carbonaceous chondrite-like source material. More detailed conditions and processes of fractional melting and smelting on the parent body has been examined [7], and thermal evolution and physics of melt extraction [8] have been proposed recently, but no evidence of crystal elongation has been found. Our discovery of the growth textures and Ca chemical zonings in NWA 4519 may provide us with good evidence of the proposed mechanism.

Acknowledgements:

We thank the NIPR for the meteorite sample. This work was supported in part by funds from Cooperative Program of NIPR and ORI, Univ. of Tokyo.

References:

[1] Jenniskens P. et al. (2009) *Nature, 458,* 485-488. [2] Connolly Jr H. C. et al. (2009) *Meteoritical Bull.* 92, 1659-1660. *Meteoritics & Planet. Sci., 44,* 5444. [3] Berkley J. L. et al. 1980. *Geochim. Cosmochim. Acta* 44, 1579. [4] Goodrich C. A. et al. 1987. *Geochim. Cosmochim. Acta* 51, 2255. [5] Takeda H. (1987) *Earth & Planet. Sci. Lett.*, 81, 358-370. [6] Connolly H. C. Jr. et al. (2007) *Meteori. Bull.* 92, *Meteorti. Planet. Sci.* 42: 1647-1694. [7] Goodrich C. A. et al. (2007) *Geochim. Cosmochim. Acta* 71, 2876-2895. [8] Wilson L. (2008) *Geochim. Cosmochim. Acta* 72, 6154-6176.

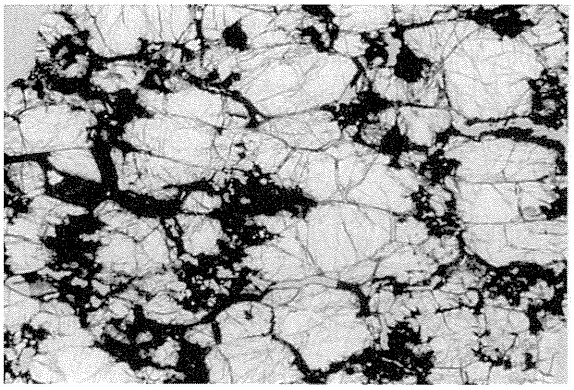

Fig. 1. Photomicrograph of PTS NWA 4519,1. Width: 6.6 mm. Parallel light.

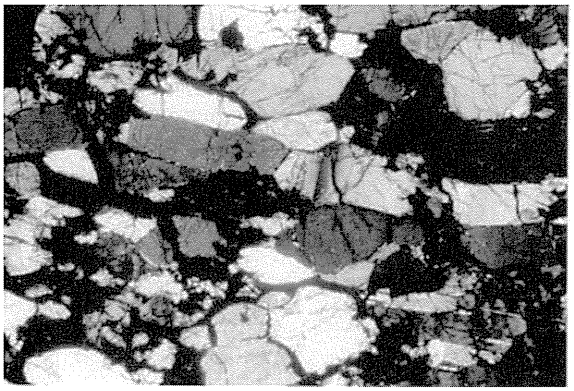

Fig. 2. The same area as that of Fig. 1. Cross polar.

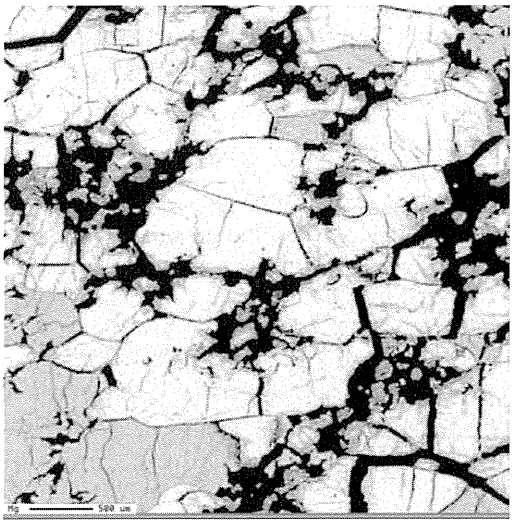

Fig. 3. Elemental distribution map of Mg of the NWA 4519 ureilite. Yellow: Olivine; Green: Pigeonite. Scale bar: 500 μ m.

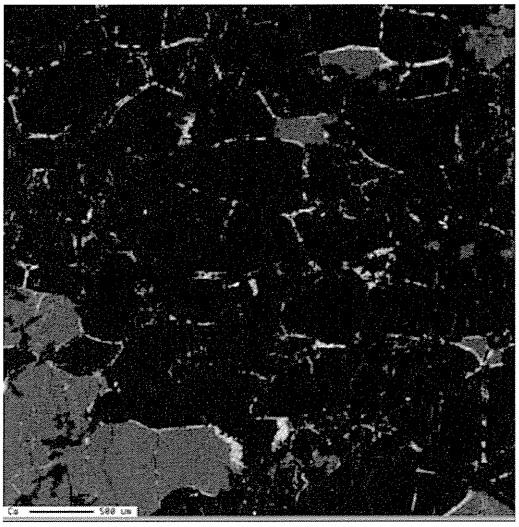

Fig. 4. Elemental distribution map of Ca of the NWA 4519 ureilite. Dark blue: Olivine; Green: Pigeonite; Greenish blue: Augite. Scale bar: 500 μ m. Note that the elongated pigeonite crystal along the horizontal direction has augite rim at the top (right) of the crystal.

Carbon isotope measurement of Murchison carbonate by SIMS: A comparison to isotope variation by the chemical method. S. Tsutsui, H. Naraoka, F. Kitajima and T. Nakamura, Department of Earth and Planetary Sciences, Kyushu University, 6-10-1 Hakozaki, Higashi-ku, Fukuoka 812-8581 Japan.

Introduction:

Carbonate in chondrites occurs mostly as calcite, which is a secondary alteration product associated with hydrous activity on the meteorite parent body. The carbonate in CI, CM and CR chondrites is characterized by significantly ^{13}C-enriched signature (ca. +40 to +80‰ relative to PDB), while that of CV and CO generally has a similar $\delta^{13}C$ value as terrestrial carbonates [1]. While oxygen isotopic ratio of the carbonate has been used to estimate the alteration temperature [2, 3], the ^{13}C-enriched carbon source(s) remains unclear. The ^{13}C-depleted CH_4 generation resulting from reduction of bicarbonate by H_2 may cause a ^{13}C-enriched pool for the carbonate formation [3]. However, some chondritic organic compounds such as carboxylic acids are ^{13}C-enriched, being a possible source for the carbonate [4].

The carbon and oxygen isotope measurement of carbonate has been generally conducted by CO_2 evolving from tens to hundreds of mg meteorites with 100% phosphoric acid [1-3]. Recently, we have performed the isotope analysis using sub- to a few mg of CM2 chondrites, revealing that the smaller sample is more heterogeneous isotopically (e.g. $\delta^{13}C$ = +27 to +52 ‰ relative to PDB for sub- to a few mg [4] compared to +32 to +42 ‰ for tens of mg [1]) in Murchison. The $\delta^{13}C$ value of carbonate is negatively correlated with that of the coexisting organic carbon. In this study, we analyze isotopic composition of calcite by secondary ion mass spectrometry (SIMS), comparing the $\delta^{13}C$ variation to discuss the carbon source of carbonate.

Experimental:

The carbonate occurrence was examined by SEM-EDS and Raman spectroscopy using the same Murchison specimen as used for the isotope analysis by the chemical method. The carbon and oxygen isotopic compositions of calcite are determined by SIMS (CAMECA ims-6f; 19.5 kV Cs^+ as a primary beam) with the NBS-19 standard.

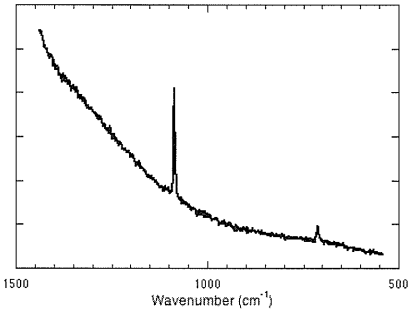

Fig. 1. Raman spectra of calcite in Murchison

Results and discussion:

The Ca and Mg mapping shows abundant sub-micron and a few up to ~50 μm carbonate in matrix as well as chondrule, which is consistent with previous studies [5]. The carbonates are identified as calcite by Raman spectra (Fig. 1). The calcite has the $\delta^{13}C$ value between +30 and +52‰ by SIMS, which is the same range for carbonate as obtained by the chemical method [4]. The SIMS analysis confirms high isotopic heterogeneity of calcite in a mm scale sample. The largest calcite in this study is enriched in ^{13}C (+49‰ and +52‰, Fig. 2), while smaller calcite is not enriched in ^{13}C (ca. +30‰).

The ^{13}C-enriched signature of large calcite may be suggestive of the main source in primarily ^{13}C-enriched carbon, as the alteration fluid could be limited in flow at distances of up to 100's μm [6]. If the ^{13}C-enriched pool caused by ^{13}C-depleted CH_4 generation contributes the carbonate formation, the ^{13}C-enriched fluid could not be an initial source. On the other hand, the initial carbonate fluid derived from organic matter is enriched in ^{13}C [7], being likely a carbon source for the carbonate.

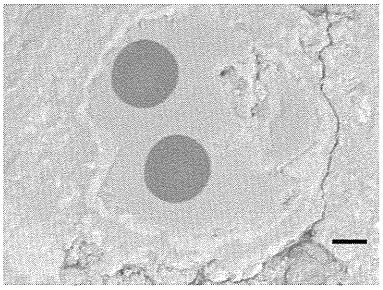

Fig. 2. BSE image of calcite in Murchison after SIMS analysis (scale: 10 μm)

Summary:

We performed carbon isotope analysis of Murchison calcite by SIMS, ranging from +30 to +52‰, which is a similar isotopic composition for carbonate obtained by the chemical method. The $\delta^{13}C$ distribution suggests that the ^{13}C-enriched organic component is a probable carbon source for carbonate in CM chondrites.

References:

[1] Grady M. M. et al. (1988) *GCA,* **52**, 2855-2866. [2] Benedix G. K. et al. (2003) *GCA,* **67**, 1577-1588. [3] Guo W. and Eiler J. M. (2007) *GCA,* **71**, 5565-5575. [4] Tsutsui S. et al. (2009) *Antarctic Meteorites XXXII*, 70. [5] Bunch T. E. and Chang S. (1980) *GCA,* **44**, 1543-1577. [6] Bland P. A. et al. (2009) *EPSL,* **287**, 559-568. [7] Oba Y. and Naraoka H. (2009) *MAPS,* **44**, 943-953.

Conditions of atmospheric entry of spherical silicates in dust rich layers of Dome Fuji ice core.

M. Uesugi, Department of Adaptive Machine Systems, 2-1 Yamadaoka, Suita, Osaka 565-0871, JAPAN

Introduction:

Recently, two silicate rich dust layers were found in Dome Fuji ice core and EPICA-Dome C in Antarctica [1]. Size of the dusts in the dust layer is from sub-μm to several tens μm. Their texture and chemical composition show that they would be melting products by high temperature heating. In addition, the dust particles form aggregates from tens to hundreds μm diameter. These features indicate that the dust particles were once totally melted, and coagulated during or after the resolidification.

Trajectory and thermal evolution of tiny dust grains during atmospheric entry were investigated in several previous studies. Love and Brownlee [2][3] constructed a comprehensive model for the calculation of thermal evolution of dust grains. However, they calculated for the cases larger than 2 μm, and did not include some effects important for the cases of smaller dust grains.

In this work, a model is developed for the numerical simulation of atmospheric entry of tiny dust grains. The code calculates thermal evolution and trajectory of the dust grains. Using the characteristics of the dusts in dust rich layer in Dome Fuji ice core, such as melting temperature and radius of the dust grains, the condition of their atmospheric entry are investigated by the numerical code.

The model calculation will also be extended to the investigation of the possibility of the coagulation of dust particles during the atmospheric entry in future work.

Models and calculations:

Basis of the model for the calculation of atmospheric entry of dust particles is almost same as Love and Brownlee [2]. As the improvement of the model, porosity change, exact calculation of the drag coefficient and heat transfer function between the dust particles and gas molecules, and size dependency of the emissivity for smaller dust grains, are included in the calculation.

Emissivity change of small dust grains

The Planck-averaged emissivity is proportional to the particle radius for small particles, but independent of size for large particles [4]. In this work, the emissivity is set to 0.8 for the dust particles with diameter ≥ 4 μm. It changes from 0.8 to 0.2 for dusts from 4 μm to 1 μm, and constant value 0.2 is applied for dust particles of ≤ 1 μm [5].

Porosity change of the dust grains

Effect of porosity change by the melting of fluffy dusts is also included in the model. Love et al. [6] showed that the mass density of IDPs range around 2 g cm^{-3}. Flynn and Sutton [7] show that porous IDPs have mass density around 0.6 g cm^{-3}. Tsuchiyama et al. [8] have also estimated the mass density of Stardust grains as 1 to 3 g cm^{-3} from the track volume. On the other hand, mass density of melted solar composition silicates, such as chondrules, is ~ 3.4 g cm^{-3} [9]. According to these studies, the initial density of dust particle was set to 1 g cm^{-3}. When temperature of the dust particle reaches melting temperature, the density quickly changes to 3.4 g cm^{-3}. Because the time scale of the surface oscillation of melted silicate is < 10^{-4} sec [10] and is much smaller than the time step of the calculation (10^{-2} sec), the density change is set to be completed within a time step. Relating the density change, the diameter of the dust grains also changes to keep mass conservation.

Evaporation of silicate material

Evaporation of the silicate material is important function of the calculation, because it affects not only final radius of dust particle, but also affects the thermal history of the dust particle by releasing latent heat of evaporation. Saturated vapor pressure of stony meteorites is given by

$$\ln P_v = C_1 - C_2/T_d \qquad (1)$$

where C_1 and C_2 are the constant and T_d is temperature of the dust particle [2][11]. Opik (1958) [12] showed the values of C_1 and C_2 for stony meteorite as 10.6 and 13500, respectively.

Evaporation rate of the dust particle in Fig. 2 of Love and Brownlee [3] is too large, though they used same equation of Eq. (1) in their studies. Some errors might exist in the calculation of P_v in their studies.

Parameters of silicate spheres in DF2961

Misawa et al. [1] indicate the possibility that dusts in upper layer (DF2641) of dust rich layer in Dome Fuji ice core would be formed by impact cratering or aerial burst on the East Antarctic ice sheet. They also suggest the possibility that the dust particles in lower layer (DF2691) are formed by atmospheric entry. In this work, size range and chemical composition of DF2691 are used for the calculations. Initial diameter of the dust grains is set from 0.1 to 10 μm. The melting temperature is calculated as 1261°C from the averaged chemical composition of dust spheres in DF2691.

Results and discussions:

Figure 1 shows the condition required for the total melting of dust particles during the atmospheric entry. Each line shows the boundary between the total melting and partial melting conditions for each case of the incident angle. All calculations in Fig. 1 are stated from 200 km altitude from Earth's surface.

In any cases, extremely large incident velocity is required for the total melt of the dust particles. These tiny particles, less around 1 μm, are quickly loses their initial velocity at the uppermost part of the Earth' atmosphere by the drag of gas molecules. Because the mass density of the atmosphere is small and drag heating of gas molecules is weak at the uppermost region of the atmosphere, thermal energy added by the drag heating is quickly radiated away before increase of the temperature of the dust particle. For the case of 0.1 μm dust particles, the required velocity for the total melting is around 110 km s^{-1}, even by the vertical incident to the atmosphere. Large incident velocities around 80 km s^{-1} relative to the Earth are accomplished by the cometary origin dust [13]. However, relative velocity much larger than 100 km s^{-1} unlikely occurs in solar material.

Figure 2 shows results of the calculations those started from different altitude. Initial condition of these calculations simulates the breaking up of larger meteoroid (> 1 mm) at each altitude. A parent meteoroid of the dust grains conserves its initial velocity during the atmospheric entry to a certain altitude, because of relatively larger inertia than small dust grains. As the mass density of the atmosphere increases, the parent meteoroid begins to break up by friction and/or ram pressure of gas molecules at the upper atmosphere, and small dust grains are released with large relative velocity to the gas molecules in a dense region of the atmosphere. The results clearly show that the dust grains are melted much lower velocity than Fig. 1 for the case of lower altitude. The absence of the deceleration at the uppermost region of the Earth's atmosphere leads to the effective drag heating at dense region of the lower atmosphere.

However, the parent meteoroids should be broken into extremely small pieces, less than 10^{-4} times of their parent meteoroids in diameter, in these cases. Flynn et al. [14] show that smallest grains of the broken pieces of Murchison hydrous CM2 meteorite are ~ 10^{-6} g, i.e. ~ 100 μm. It is highly unlikely that the disruption of chondritic meteorites produces amounts of fragments from sub-μm to μm diameter by impact or explosion. One of the possible origins of the dusts in DF2691 is cometary origin meteoroid. If parent meteoroids were originally composed of such tiny grains, they could break up into the smallest unit of their components. Studies of Stardust samples appear that most of the terminal grains are fragile aggregates of small grains [15], and support this hypothesis.

References: [1] Misawa et al., (2010) *EPSL, 289,* 287–297. [2] Love and Brownlee, (1991) *Icaurs, 89,* 26–43. [3] Love and Brownlee, (1994) *Meteoritics, 29,* 69–70. [4] Draine and Lee, (1984) *Astrophys. J., 285,* 89-108. [5] Desch and Connolly, (2002) *MAPS, 37,* 183–207. [6] Love et al., (1994) *Icarus, 111,* 227–236. [7] Flynn and Sutton (1990) *LPSC, XXI,* 375-376 [8] Tsuchiyama et al., (2009) *MAPS, 44,* 1203–1224. [9] Kuebler et al., (1999) *Icarus, 141,* 96–106. [10] Uesugi et al., (2003) *EPS, 55,* 493–507. [11] Bronshten (1983) *Physics of meteoric phenomena*, pp. 341. [12] Opik (1958) *Physics of meteor flight in the atmosphere*, pp. 174. [13] Flynn (1989) *Icaurs, 77,* 287–310. [14] Flynn et al. (2009) *PSS, 57,* 119–126. [15] Nakamura et al. (2009) *MAPS, 43,* 247–259.

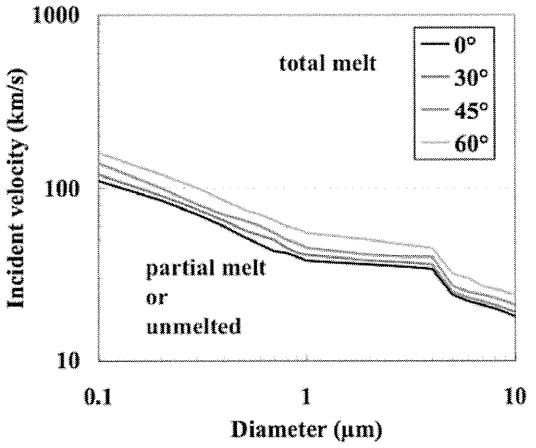

Fig. 1
A schematic diagram of condition for the total melting of dust grains. Each line shows the boundary between the condition for the total melting and partial melting of the dust grains for each incident angle. Emissivity increases by grain's diameter from 1 μm to 4 μm, and radiative cooling becomes gradually effective with the size increasing. Therefore, the temperature does not increase by increase of incident velocity so much, and boundary lines show plateau at the size range.

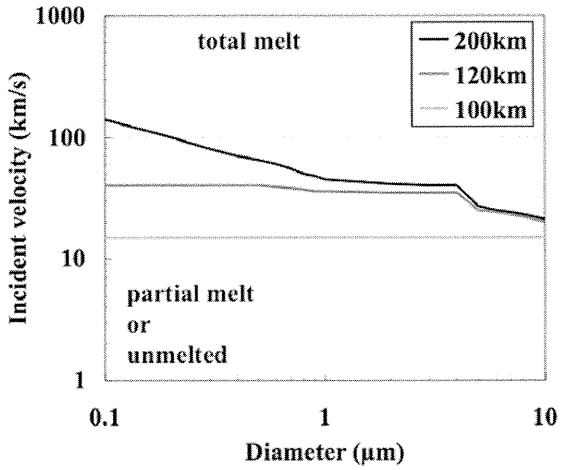

Fig. 2
Same diagram of Fig. 1, but the lines correspond to altitude of the onset of the heating. Incident angle is 45° and initial temperature of the particles is 400 K, for all cases.

Petrology and thermal history of Asuka and Yamato diogenites. A. Yamaguchi[1], J. A. Barrat [2] and M. Ito[3,4]. [1]National Institute of Polar Research, Tachikawa, Tokyo 190-8518, Japan. E-mail: yamaguch@nipr.ac.jp, [2]Université Européenne de Bretagne. [3]UBO-IUEM, CNRS UMR 6538, place Nicolas Copernic, 29280 Plouzané Cedex, France, [3]ARES, NASA Johnson Space Center, Houston, TX 77058, USA, [4]Lunar & Planetary Institute-USRA, Houston, TX 77058, USA.

Introduction:

Diogenites are a member of HED meteorites thought to be derived from an asteroid 4 Vesta. Isotopic and geochemical evidence supports the existence of magma ocean on early Vesta [1,2]. The magma ocean model predicts the presence of mafic cumulates beneath the residual magma ocean. Earlier studies showed that the orthopyroxene cumulates are diogenites [e.g., 3]. Major element compositions of pyroxenes (plotted on pyroxene quadrilaterals) form "trend" from diogenites to eucrites with no gaps supporting this hypothesis [3,4]. However, major and trace elements compositions in diogenitic pyroxenes indicate complex petrogenetic histories. Several workers suggested that diogenites crystallized from a few distinct magmatic bodies [5-7]. Recently, Barrat et al. [7] suggested that parental magmas of diogenite formed by remelting of earlier-formed mafic cumulates (harzburgites) beneath a magma ocean. Furthermore, Barrat et al. [8] suggested the REE variations of some diogenites can be explained in terms of interaction between the parental magmas and early-formed eucritic crust. Here we report petrology and thermal history of ten Antarctic diogenites to better understand the petrogenetic history.

Samples and analytical procedures

We studied polished thin sections (PTSs) of ten diogenites, Asuka (A)-87147, A-880785, A-880936, A-881239, A-881377, A-881548, A-881838, A-881839, A-881944, and Yamato (Y)-74097. Two PTSs were made from different portions of the main mass of A-881526 (110.2 gram) to ensure the distribution of olivine. Barrat et al. [7,8] reported the chemical compositions of these diogenites. PTSs of these diogenites were examined optically and with a scanning electron microscope (SEM) (JSM5900LV) equipped with an energy dispersive spectrometer (EDS) (Oxford Link-ISIS), and electron microprobe analyzers (EPMA) (JXA8200) at NIPR. Silica polymorphs were identified using a laser micro Raman spectrometer (JASCO NRS-1000) at NIPR.

Results:

Ferroan diogenites, A-881838 and A-881839 are breccias, and are probably paired because of the similar textures and mineral chemistry. The PTSs of these meteorites are composed of pyroxenes (~96-97 vol%) with minor amounts of plagioclase, silica minerals, chromite, and FeS. The PTS of A-881839 contains a greater abundance of plagioclase (3 vol%) in contrast to that of A-881838 (~1 vol%). The range of clasts and fragments are up to 4 mm. A-881839 PTS contains brecciated domains (~1.5 mm) composed of plagioclase grains (<0.2 mm) and elongated plagioclase (~0.1 x 0.2 mm). A-881838 contains a large grains of chromite (1.4 x 0.6 mm). Orthopyroxene grains in many cases contain fine (< several μm) blebs and fine (<a few μm) augite lamellae concentrated along the grain boundaries. Occasionally, there are large grains of augite (several tens of μm). The pyroxenes textures are similar to those in Y-75032 type achondrites [9].

A-881548 is partly brecciated and contains significant amounts of olivine. One PTS of A-881548 contain 46 vol% olivine. The other contains a larger amount of olivine (~80 vol%). However, a chip for chemical study showed no signature of olivine [8]. Thus, olivine grains in A-881548 are distributed heterogeneously. The sizes of the pyroxene and olivine grains in A-881548 is larger than ~1 cm. The grains of pyroxenes and olivine have generally sharp or slightly curved boundaries except brecciated areas. Minor minerals include chromite and Fe-FeS; no plagioclase and silica minerals are found.

A-881377 is a breccia composed of clasts of orthopyroxene and harzburgites. The sizes of the clasts are typically ~1-2 mm in size, but we found a large clast (5.3 x 4.4 mm). This diogenite contains a significant amount of olivine (5 vol%). The minor minerals include plagioclase (~1 vol%), Fe-FeS (0.4 vol%), and silica minerals. The common mineralogical features in pyroxenes in clasts and matrix indicate that this rock is a monomict breccia of harzburgitic diogenites. In the harzburgite clasts, fine droplets and worms of orthopyroxene and chromite occur along boundaries between larger grains of olivine and orthopyroxene.

Y-74097 is one of the Yamato-A type diogenites characterized by granoblastic textures mostly composed of pyroxene with traces of chromite, silica minerals, and FeS [10]. Cristobalite and tridymite are identified by Raman spectroscopy. Takeda et al. [10] suggested that the fine-grained areas cover areas up to 3 cm and seem to be covered by the coarse-grained area. In our PTS, there are large domains of fine-grained area surrounded by veins of clear coarser-grained area. There is one large chromite surrounded by clear pyroxene.

Diogenites, A-87147, -880785, -880936, -881239, -881526, and -881944 are breccias consisting of orthopyroxenenite clasts and fragments

of orthopyroxenes (up to several mm) showing typical textures of diogenites. Minor minerals include chromite, Fe-FeS and silica minerals.

The Mg' values (= molar Mg/(Mg+Fe) x 100) of bulk pyroxenes in the diogenites studied here vary from 70 to 78 covering the range of reported diogenites [e.g., 5,6,11] (Fig. 1). The ferroan diogenites (Mg' = 69.8-70.5) contain orthopyroxene probably inverted from low-Ca pigeonites. Minor element compositions (Al_2O_3, TiO_2, and Cr_2O_3) are within the range of diogenites but distinct from those of cumulate eucrites and Y-75032 type diogenites. Chromites in A-881388/89, A-881377 and A-881944 have larger ranges of Al/Cr ratios.

Two diogenites, A-881377 and Y-74097 have pyroxenes which are chemically zoned. The CaO abundances decrease toward core (~1.2-1.8 wt% for A-881377; ~1.0-1.6 wt% for Y-74097). The Al_2O_3 and TiO_2 are slightly enriched in the rims compared to those in the cores. Y-74097 pyroxenes have Mg' zoning (Mg' = ~74-76) whereas those of A-881377 do not have zoning. Takeda et al. [10] reported the chemical zoning only in the coarse-grained areas in Y-74097. In our observation, the chemical zoning extends over the entire recrystallized orthopyroxene crystals. The abundances of these elements continuously increase toward the rims with no gaps. The presence of chemical zoning indicates that the fine-grained areas were originally large (a few cm in size) single crystals before recrystallization. Original grain boundaries are more fractured than the interiors causing rapid grain growths forming clear coarse-grained rims by moderate thermal annealing.

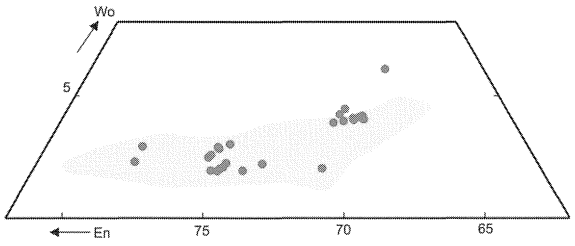

Fig. 1. Chemical compositions of bulk pyroxenes in diogenites studied here plotted in a part of pyroxene quadrilateral. Shaded area is the range of other diogenites [5,6,11]

Discussion:

It is widely believed that diogenites are cumulate rocks that crystallized in the deep crust [e.g., 3]. The fact that most diogenites are cumulate rocks seems to be correct on the basis of bulk trace element data [5,8]. This is also consistent with the fact that many diogenites have homogeneous major element compositions. However, at least five diogenites have reported to have chemically zoned pyroxenes; these are Garland [6], NWA 4215 [12], Dho 700 [13] and two diogenites studied here, A-881377, and Y-74097.

It seems that the initial cooling rates and subsolidus thermal history of diogenites are variable, similar to those of basaltic eucrites. Some diogenites cooled rapidly from melts and escaped from thermal metamorphism, and preserve chemical zonings in pyroxenes. Others cooled rapidly and were metamorphosed, or cooled slowly in the plutonic conditions so that there are no chemical zonings in pyroxenes. With respect to the thermal history, we propose two types of diogenites; equilibrated diogenites and unequilibrated eucrites, a similar scheme for basaltic eucrites [14,15]. Equilibrated diogenites have homogeneous pyroxenes with respect to major and minor elements whereas unequilibrated diogenites preserve igneous zoning that formed during initial crystallization.

We could not find relationship between thermal history and chemical compositions among the diogenites. Barrat et al. [7,8] classified the diogenites studied here into several chemical groups. A unequilibrated diogenite, Y-74013 and equilibrated diogenites, A-880785 and A-880936 are in the same chemical group. Although A-87147 and A-881377 have similar REE patterns, their textures and mineralogy are very different. A-881377 is an olivine-bearing, unequilibrated diogenite. A-881548 is an olivine diogenites but its REE pattern resembles the residue of a ferroan diogenite, A-881839. Clearly, the petrogenetic history of diogenites is complicated.

References:

[1] Righter K. and Drake M. J. (1997) Meteor. Planet. Sci. 32, 929-944. [2] Greenwood R. C. et al. (2005) Nature 435, 916-918. [3] Takeda H. (1979) Icarus 40, 455-470. [4] Takeda H. (1997) Meteor. Planet. Sci. 32, 841-853. [5] Mittlefehldt D. W. 1994. Geochim. Cosmochim. Acta 58, 1537-1552. [6] Fowler G. W. et al. 1994. Geochim. Cosmochim. Acta 58: 3921-3929. [7] Barrat J. A. et al. 2008. Meteor. Planet. Sci. 43, 1759-1775. [8] Barrat J. A. (2010) Geochim. Cosmochim. Acta, submitted. [9] Takeda H. and Mori H. (1985) Proc. 15th Lunar Planet. Sci. Conf., J. Geophys. Res. 90, C636-C648. [10] Takeda H. et al. (1981) Mem. NIPR Spec. Issue No. 20, 81-99. [11] Beck A.W. and McSween H.Y. (2010) Meteor. Planet. Sci., in press. [12] Barrat J. A. et al. 2006. Meteor. Planet. Science 41, 1045-1057. [13] Yamaguchi A. et al. Meteor. Planet. Sci., submitted. [14] Reid A. M. and Bernard B. M. (1979) Lunar Planet. Sci. 10, 1019-1021. [15] Takeda H. and Graham A. L. (1991) Meteoritics 26, 129-134.

K-rich Fragments in LL-chondritic Breccias.

T. Yokoyama[1], K. Misawa[1,2], and O. Okano[3], [1]The Graduate Univ. for Advanced Studies, Tachikawa, Tokyo 190-8518, Japan. E-mail: yokoyama.tatsunori@nipr.ac.jp. [2]AMRC, NIPR, Tachikawa, Tokyo 190-8518, Japan. [3]Faculty of Sci., Okayama Univ., Okayama 700-8530, Japan.

Introduction: Alkali-rich igneous fragments are found in brecciated LL-chondrites, Krähenberg (LL5) [1], Bhola (LL3–6) [2], and Yamato 74442 (LL4) [3, 4]. Abundances of alkaline elements in the fragments are ~0.5×CI for Na, ~12×CI for K, ~45×CI for Rb, and ~70×CI for Cs, showing alkaline element fractionations [5]. Because Na is depleted, these alkali-rich fragments were treated as K-rich fragments. Rare earth element (REE) abundances of the K-rich fragments are chondritic except for a negative Eu anomaly [5]. On the basis of their bulk compositions including REEs, it is suggested that alkali differentiation of the fragments may have resulted from an exchange between Na and K in feldspar via a vapor phase [5]. However, the timing of this alkali differentiation has not been discussed so far. The K-rich fragments in Krähenberg and Y-74442 yield old Rb–Sr ages of 4.662+/–0.014 Ga [1] and 4.571+/–0.022 Ga [6], respectively (recalculated using the decay constant of Rb; $\lambda=1.402\times10^{-11}y^{-1}$).

In order to understand fractionation process of alkaline elements in K-rich fragments, we have undertaken mineralogical and petrological studies. Trace element analyses and Rb–Sr isotopic studies on K-rich fragments in Bhola, and Y-74442 are in progress.

Experimantal: We observed thin sections of Krähenberg, Bhola, and Y-74442 under an optical microscope and a scanning electron microscope (SEM). Chemical compositions of K-rich fragments were analyzed by an electron probe micro analyzer (EPMA).

Results and Discussion: K-rich fragments in Krähenberg, Bhola, and Y-74442 are composed of euhedral olivine (10 – 100 μm in size) and a groundmass of brown glasses, which are enriched in alkaline elements (Fig. 1). Grain sizes of olivines in the Krähenberg and Bhola fragments are large in size and euhedral in shape compared with those of olivines in Y-74442 fragments. In the alkali-rich glasses, troilite (~10 μm in size), dendritic pyroxene (~1 μm in size), and dendritic chromite (~1 μm in size) are commonly observed. The sizes of constituent phases in the fragments are different for each meteorite, but modal abundances of olivine and glass are very similar: olivine=~60 vol%; groundmass glass including microcrystalline pyroxene=~40 vol%.

Chemical compositions of olivine in the K-rich fragments fall in compositional range of LL-chondrites (Fa_{26-32} [7]). Chemical compositions of K-rich glasses are overlapping on a ternary diagram (Na＋K＋Al-oxides, Ca＋Mg＋Fe-oxides, and SiO_2) (Fig. 2). Abundances of Rb in the whole rock of Y-74442 and Bhola samples are 8.09 ppm (~4×CI) and 6.47 ppm (~3×CI), respectively. Abundance of Sr in the whole rock of Bhola is chondritic (10.3 ppm).

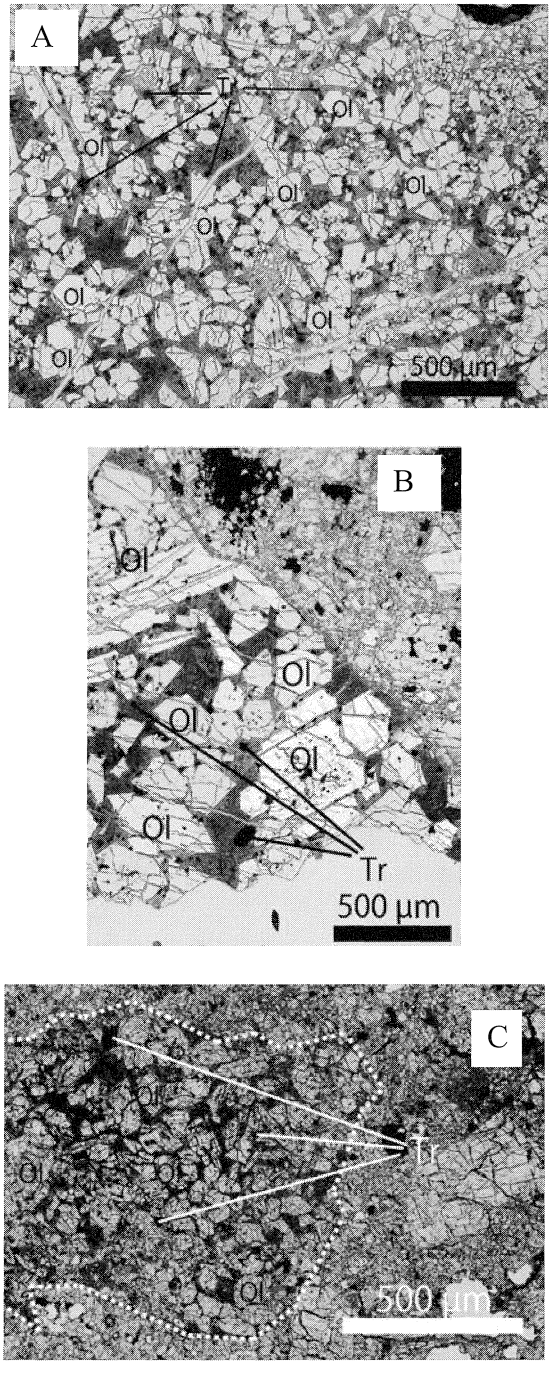

Fig. 1. Photomicrographs of K-rich fragments in Krähenberg, (A) Bhola (B), and Yamato-74442 (C). Transmitted light.

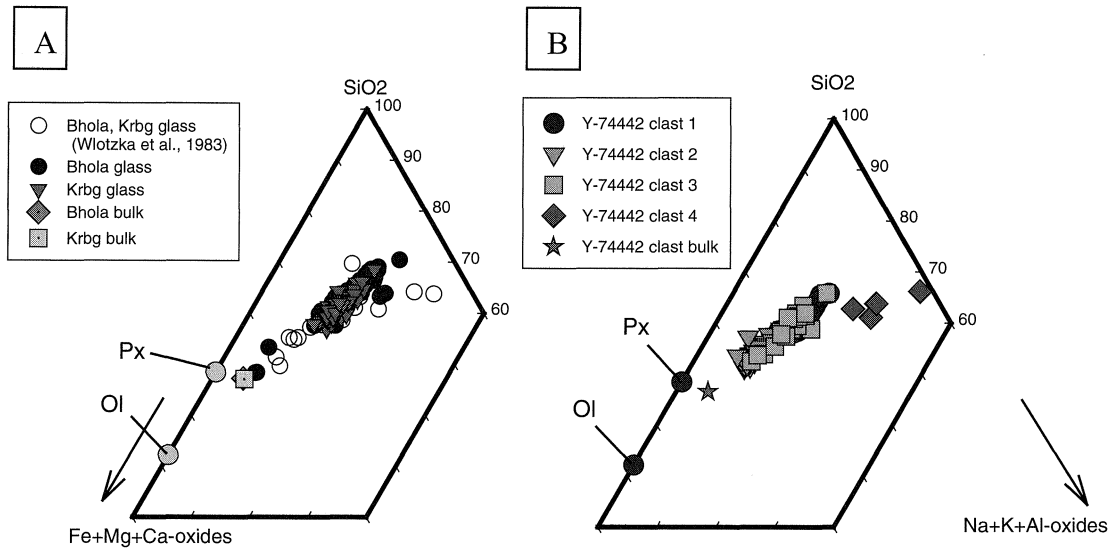

Fig. 2. Chemical compositions of groundmass glasses including microcrystalline pyroxene in Krähenberg and Bhola (A), and Y-74442 (B).

Although grain sizes of olivine are somewhat different, the textures and constituent phases of K-rich fragments in Krähenberg, Bhola, and Y-74442 are identical. Elemental abundances of K-rich fragments in Krähenberg, Bhola, and Y-74442 are plotted normalized to their hosts [8, 4], showing characteristic fractionation patterns; Na is depleted and K is enriched (Fig. 3).

Similarities in textures and chemical compositions of K-rich fragments indicate that K-rich fragments might have experienced common thermal histories; precursor materials of the fragments melted and then quenched (enough time scale to crystallize 100 μm-sized olivine grains). Identical bulk chemical compositions of K-rich fragments also suggest that they might come from related precursor materials. The observed enrichments of Rb in the whole-rock samples indicate that certain amounts of K-rich fragments were incorporated during brecciation processes on the parent bodies of Bhola and Y-74442.

Humayun and Clayton. [9, 10] determined K isotopic compositions of solar system materials and suggested that depletion of volatile elements occurred in the early solar system, on the basis of unfractionated K isotopic compositions including K-rich clasts in Krähenberg. If volatile element fractionations did not occur after the early depletion process, it is hard to fractionate alkaline elements by an exchange via vapor phase without mass dependent fractionations.

References: [1] Kempe W. and Müller O. (1969) *Meteorite Research*, pp. 418–428. [2] Noonan A. F. *et al.* (1978) *Geol. Survey Open File Report* **78–701**, pp. 311–312 [3] Yanai K. et al. (1978) *Mem. Natl Inst. Polar Res., Spec. Issue* **8**, 110–120. [4] Ikeda Y. and Takeda H. (1979) *Mem. Natl. Inst. Polar Res., Spec. Issue* **15**, 123–139. [5] Wlotzka F. *et al.* (1983) *Geochim. Cosmochim. Acta* **47**, 743–757. [6] Nishiya N. *et al.* (1995) *Okayama Univ. Earth Science Report* **2**, 91–102. [7] Dodd R. T. (1981) *Meteorites* pp. 368, Cambridge Univ. Press. [8] Miller J. *et al.* (1981) *Meteoritics* **16**, 69–76.[9] Humayun M. and Clayton R. N. (1995) *Geochim. Cosmochim. Acta* **59**, 2115–2130. [10] Humayun M. and Clayton R. N. (1995) *Geochim. Cosmochim. Acta* **59**, 2131–2148.

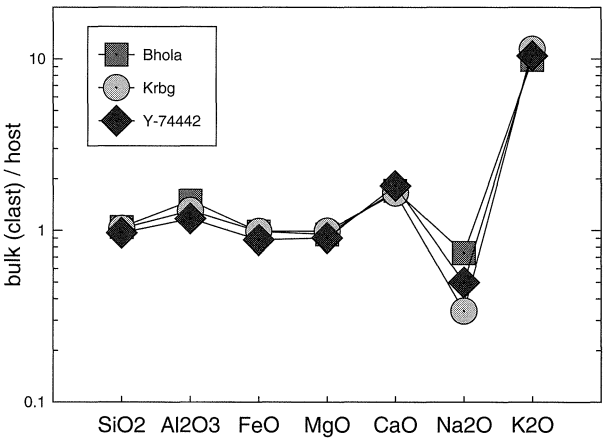

Fig. 3. Bulk compositions of K-rich fragments in Krähenberg, Bhola, and Y-74442, plotted relative to their host compositions. The host compositions of Krähenberg and Bhola, and Y-74442 are from [8], and [4], respectively.

Electron microprobe analyses in an Antarctic meteorite, Y980175 CV chondrite. M. Yoshitake[1], H. Kojima[1], [1]Antarctic Meteorite Research Center, National Institute of Polar Research, 10-3 Midori-cho, Tachikawa City, Tokyo 190-8518, Japan.

Introduction:

CV chondrites were divided into three subgroups, reduced, oxidized Allende-like (CV_{oxA}), and oxidized Bali-like (CV_{oxB}) [1]. It has been generally considered that the difference of subgroups has resulted from the differences in the formation and/or alteration conditions among them [1]. Therefore, the classification of subgroups is important to reveal the origin of the meteorite belonging to CV chondrites.

An Antarctic meteorite Yamato 980175 (Y980175) was originally defined as CV chondrite [2]. Recently our mineralogical and petrological study [3] reveled that this meteorite has the following features; 1) There is no fayalite (~ Fa_{95}), 2) Olivine grains have no chemical zoning in chondrules and AOAs, 3) There is no fayalitic olivine (~Fa_{50}) as alteration products in chondrules, 4) Magnetite and pentlandite are rare in matrix and chondrules, 5) Troilite grains widely occur in chondrules and matrix, 6) There is no Ca, Fe-pyroxene in matrix, 7) Matrix grains are small in size and not lath in shape. These features suggested that Y980175 meteorite was classified into the reduced subgroup in CV chondrite.

However, the Ni concentrations of Fe-metal and Fe-sulfide and the Mg/Fe ratio of olivine and pyroxene in chondrules are also important factors for the classification of subgroups in CV chondrite [1]. In this study, we investigated the chemical composition of those minerals in Y980175 by using an electron microprobe analyzer in order to constrain the classification of this meteorite.

Experimental procedure:

The sample in this study was a polished thin section. The surface of the sample was coated with carbon film. The petrological and mineralogical studies were performed by an optical microscope, a scanning electron microscope (SEM, JEOL JSM-5900LV), and an electron microprobe analyzer (EPMA, JEOL JXA-8200) at National Institute of Polar Research.

Results and discussion:

Y980175 consists mainly of chondrules, calcium-aluminum rich inclusions, (CAIs), amoeboid olivine aggregates (AOAs), and matrix. Most chondrules and CAIs occur as fragments, suggesting that Y980175 is a breccia. The details are shown in [3].

Fe-metal and sulfide in Y980175 occur as small (< ~ 10μm) grains in matrix and chondrules. EPMA analyses of the Fe-metal grains show that there are Ni-poor and Ni-rich metals in matrix and chondrules. The Ni concentrations of Ni-poor metal are 1.8 ~ 6.1 wt%, indicating that the metal phase is kamacite. The Ni concentrations of Ni-rich metal are 35.0 ~ 59.1 wt%, indicating that the metal phase is taenite. Those kamacite and taenite contain small amount of S (< 0.11 and < 0.07 wt%, respectively) (Fig. 1). They also contain variable and small amounts of Cr (kamacite; < 1.1 wt%, taenite; < 0.60 wt%), Co (kamacite; 0.11 - 4.1 wt%, taenite; < 1.9 wt%) and Cu (kamacite; < 0.08 wt%, taenite; < 0.27 wt%). Fe-sulfide in Y980175 is Ni-poor. The Ni concentrations of Fe-sulfide are < 0.47 wt %. Fe-sulfide also contains minor amounts of Cr (< 2.1 wt%), Co (< 0.08 wt%), and Cu (< 0.08 wt%). Those results indicate that most Fe-sulfide phase is troilite. Figure 2 shows the histograms of the Ni concentration in Fe-metal and Fe-sulfide of Y980175, comparing with those of other CV chondrites. The variations of the Ni concentrations in Fe-metal and Fe-sulfide are similar to reduced subgroup in CV chondrites.

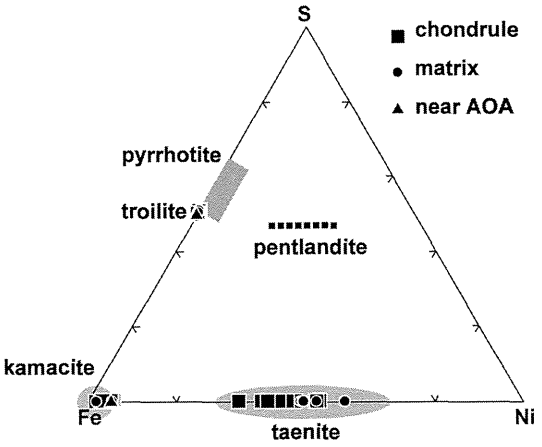

Fig. 1 Fe-sulfide and Fe-metal compositions (atomic %). A total of analysis is 80.

Most chondrules in Y980175 have a porphyritic texture. They consist mainly of olivine, low-Ca pyroxene phenocrysts, and mesostasis. Olivine and low-Ca pyroxene are enriched in Mg. They show less Fe-Mg zoning. The Mg/Fe ratios (Mg/(Mg + Fe) atom%) of the olivine are > ~ 0.79. The Mg/Fe ratios of the low Ca pyroxene are > ~ 0.92. Low-Ca pyroxene also contains variable and small amounts of TiO_2 (< 1.14 wt%) and Al_2O_3 (0.36 – 3.85 wt%). The Mg/Fe ratios of olivine and low-Ca pyroxene in Y980175 are similar to those in the meteorite belonging to the reduced CV chondrite [5].

As described above, our present results support the conclusion from our previous study [3]. The Y 980175 meteorite can be classified into the reduced

subgroup in CV chondrite.

References:

[1] Krot A. N. et al. (1998) *Meteorit. Planet. Sci., 33,* 623-645. [2] Kojima H. and Yamaguchi A. (2008) *Meteorite Newsletter 16.* [3] Yoshitake M. and Kojima H. (2009) *Antarctic Meteorites XXXII.* 81-82. [4] McSween H. Y., Jr. (1977) *GCA.* 41 pp. 1777-1790. [5] Krot A. N. (1995) *Meteoritica. 30.* 748-775.

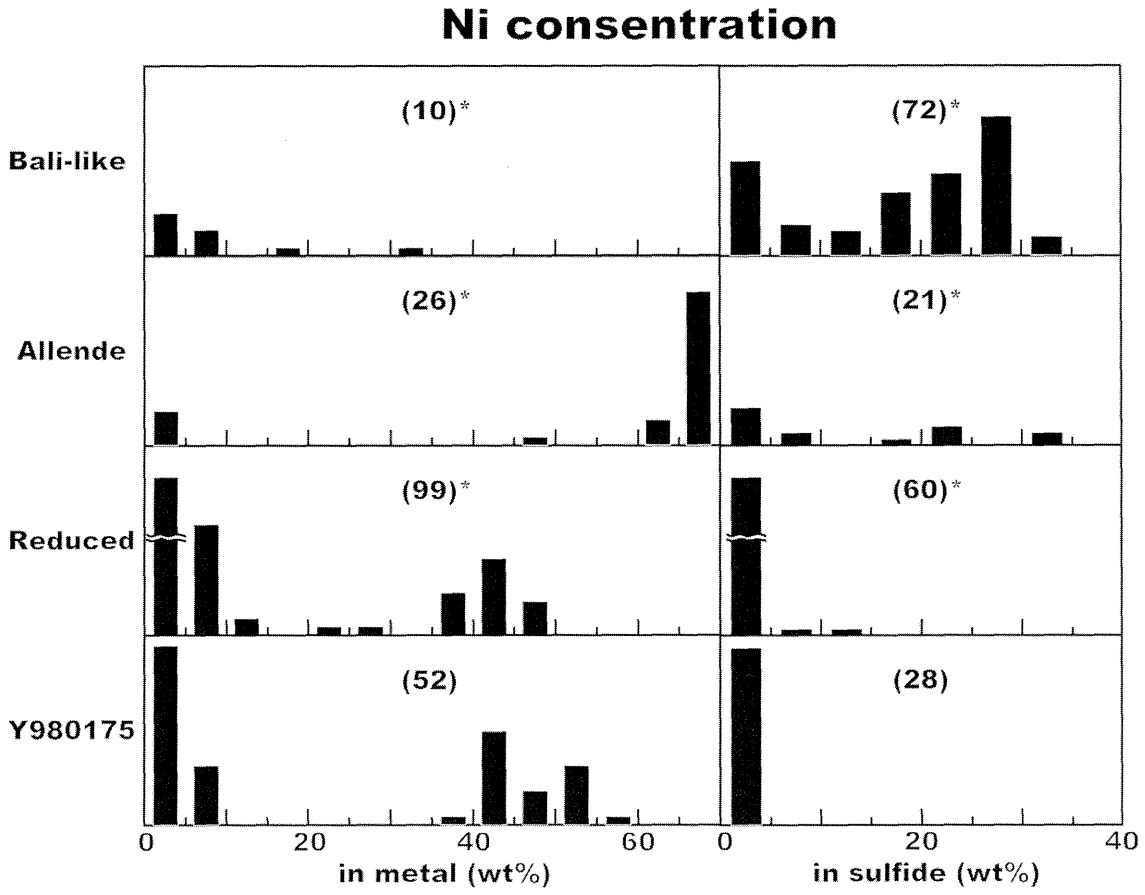

Fig. 2. Histogram of Ni concentration in Fe-metal and Fe-sulfide. The number of microprobe analyses is noted in parentheses. Dates of * are from McSween 1977 [4].

The Dhofar 961 Meteorite Group: A View into the Interior of South Pole Aitken Basin?

R. A. Zeigler, R. L. Korotev, and B. L. Jolliff. Dept. of Earth and Planetary Sciences, MacDonnell Center for Space Sciences, Washington University, St. Louis MO 63130 zeigler@levee.wustl.edu.

Introduction: Although it is nearly impossible to know the precise provenance of any individual lunar meteorite, by comparing the compositions of lunar meteorites to global remotely sensed data sets (e.g., Clementine or Kaguya), it is clear that we have numerous lunar meteorites originating from most of the major lunar crustal terranes: the Feldspathic Highlands Terrane (N=37; FHT), the Procellarum KREEP Terrane (4-5; PKT), and the lunar maria (10). An open question is whether or not we have a lunar meteorite from within the South Pole Aitken (SPA) Basin, a separate terrane as defined by [1]. The SPA Basin encompasses over 5% of the lunar surface and statistical calculations indicate that if there are 40 source craters for the lunar meteorites, there is a nearly 90% chance that one or more lunar meteorites originates from within the SPA basin [2].

Previously we postulated that on the basis of bulk composition, Dhofar 961 is the most likely lunar meteorite to have a provenance within the SPA basin [3-4]. Two other lunar meteorites, Dhofar 925 and 960, are considered paired with Dhofar 961 based on their find locations and initial petrographic descriptions [5-6]; however, although Dhofar 925 and 960 are identical in bulk composition, they are significantly different from Dhofar 961 (Fig. 1), being considerably less mafic and less enriched in incompatible trace elements (ITE). Another lunar meteorite, Sayh al Uhaymir (SaU) 449 is also identical in bulk composition to Dhofar 925 and 960 and has a similar initial petrographic description [7]. This raises two questions: 1) Are Dhofar 925, 960, 961 and SaU 449 truly paired and 2) if so, are the bulk compositions of Dhofar 925/960 and SaU 449 also consistent with an origin in the South Pole Aitken Basin?

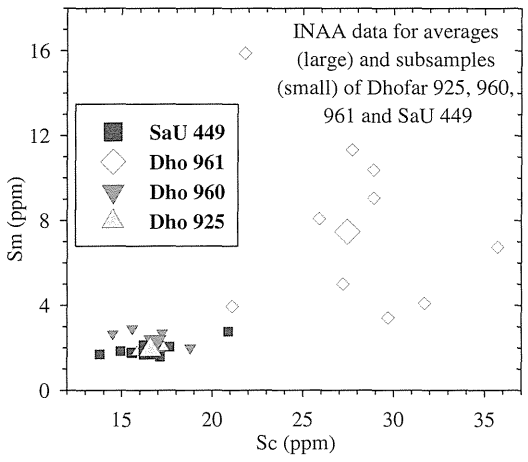

Figure 1: Sm vs. Sc in SaU 449 and Dhofar 925, 960, 961 subsamples (small symbols) and average compositions (larger symbols). Unpublished data, this lab.

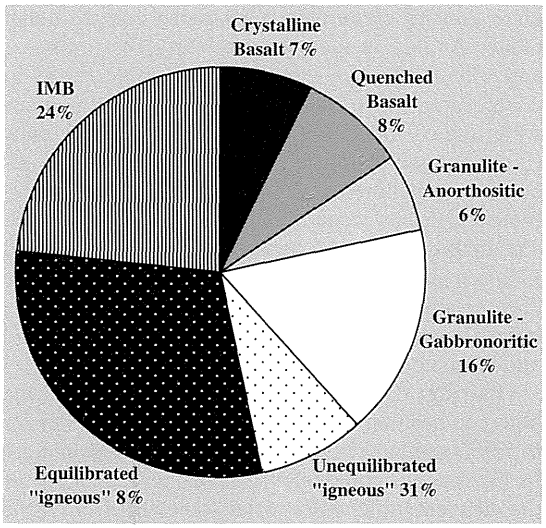

Figure 2: Percentage of clasts in each of the main lithic clast groups. Total number of lithic clasts, 350.

Here we summarize the initial results of a detailed petrographic study [8] of new sections of all 4 stones that show they are in fact paired. Furthermore, we show that the bulk composition of the Dhofar 925/960 and SaU 449 stones are consistent with the composition of portions of the SPA Basin interior using Lunar Prospector γ-ray spectroscopy data (LP-GRS).

Samples: For this study, we were able to obtain the main mass of Dhofar 961, which we polished (the cut end) and studied in our JEOL 8200 Superprobe (total area ~1.5 cm^2). Additionally we were able to obtain new polished thick sections of Dhofar 925 (0.1 cm^2), Dhofar 960 (0.2 cm^2), Dhofar 961 (0.6 cm^2), and SaU 449 (0.1 cm^2).

Petrography: All stones in the Dhofar 961 group are glassy-matrix regolith breccias. Each stone contains large and modally abundant impact melt breccia (IMB) clasts. The regolith breccia areas are extremely immature (nearly fragmental) with only a few impact spherules found. We found a wide variety of mineral and lithic clasts, but relatively few glass clasts. Shock-melt veins and areas occur in each stone and seem to be concentrated at the edges of the large IMB clasts. Terrestrial alteration products are pervasive in all sections, with fractures commonly filled with carbonate ($CaCO_3$), sulfates (principally Ca and Sr, rarely Ba and Pb), and Fe-oxides. FeNi metal grains are typically large (up to ~1 mm), rimmed/replaced by Fe-oxides or siderite or both, and more commonly found in the IMB clasts.

The mineral and lithic clasts in the regolith breccia portions of different stones are similar in abundance, textures, and composition, varying only

slightly in relative abundance of different phases. Plagioclase is the most abundant mineral clast, followed by pyroxene and then olivine in all sections. Trace amounts of silica, glass, ilmenite, chromite, and Cr-ulvöspinel clasts are also observed. Plagioclase mineral clasts have a restricted compositional range (An_{88-98}), while pyroxene ($En_{2-85}Wo_{3-43}Fs_{13-82}$) and olivine ($Fo_{5-92}$) show a considerable range in composition. Over 350 lithic clasts in all four stones were studied and classified into the following groups (Fig. 2): gabbronoritic granulite, anorthositic granulite, crystalline basalt, quenched basalt, unequilibrated "igneous", equilibrated "igneous", and IMB. The IMB clasts can be furtherer divided into Fe- and ITE-rich and Fe- and ITE-poor varieties. These lithic clast groupings are based on similarities in texture, mineral assemblage, and mineral composition and apply equally to clasts found in all four stones..

Pairing: Despite significant differences in the bulk composition of Dhofar 961 compared to Dhofar 925/960 and SaU 449 (Fig. 1), all of these stones are in fact paired. Although the absolute abundance of the different lithic clasts varies somewhat from stone to stone, textures, mineral assemblages, and mineral compositions are identical in lithic clasts found in all of the stones, particularly the gabbronoritic and anorthositic granulite clasts, the equilibrated igneous clasts, and the ITE-rich IMB clasts. The differences in bulk composition of Dhofar 961 vs. Dhofar 925/960 (and SaU 449) can be accounted for solely by different proportions of the main types of IMB present in each stone. The Fe- and ITE-poor IMBs are the dominant lithic clast in Dhofar 925/960 and SaU 449 (40-70 modal %), whereas the Fe- and ITE-rich IMB clasts dominate in Dhofar 961 (50- 60%).

Provenance: Previously [4], we determined the most likely provenance for the Dhofar 961 stone by comparing the average composition of Dhofar 961 (Table 1) to the average composition of 5° regions of the Moon as derived by the Lunar Prospector γ-ray spectroscopy data for Si, Ti, Al, Fe, Mg, Ca, K, Th, and U [9]. We compute differences between Dhofar 961 and the LP-GRS data (whole Moon) in percentages and used the sum of squares of the differences to sort for the best matches. Using this technique, the eight best matches to Dhofar 961 occur within the SPA Basin (Fig. 3). Using the same techniques, can a similar match be made for the bulk composition of Dhofar 925/960? Although the composition of Dhofar 925/960 is less diagnostic and many places on the Moon are a good compositional match, five of the top fifteen matches (including the top two) are within the SPA Basin in close spatial proximity to several of the best Dhofar 961 matches (Fig. 3). Furthermore, if we extend the number of matches, the proportion within the SPA Basin stays the same, at ~33% (i.e., 15 of the top 45 sites, etc.). This suggests that despite the compositional range among the Dhofar 961 stones, the South Pole Aitken Basin is still the most likely source region for these meteorites.

Acknowledgments: This work was funded by NASA grant NNG04 GG10G. We are indebted to Don Edwards, Norbert Classen, and Tony Irving for access to new samples. We would like to thank the NIPR for their hospitality in hosting us for this meeting.

Table 1: Compositions of Dhofar 961 group stones:

	961	449/ 925/960
SiO_2	45.9	44.9
TiO_2	0.63	0.33
Al_2O_3	17.9	22.9
FeO	11.1	7.6
MgO	10.3	9
CaO	12.7	14.2
Mg'	62	68
K	830	581
Th	3.1	0.9
U	1	0.4

K,Th, U values in ppm, all others in wt%.

References: [1] Jolliff B. L. et al. (2000) *JGR 95*: 4197-4216. [2] Korotev R. L. et al. (2009) *MAPS 44*, 1287–1322. [3] Jolliff B. L. et al. (2008a) *Microscopy & Microanalysis 2008 Meeting*, abstract # 941. [4] Jolliff B. L. et al. (2008b) *LPS 39*, abstract #2519. [5] Russell S. S. et al. (2004) *MAPS 39*, A215-A272. [6] Russell S. S. et al. (2005) *MAPS 40*, A201-263. [7] Connolly H. C. Jr. (2007) *MAPS 43*, 571-632. [8] Zeigler R. A. et al. (2010) *LPS 41*, abstract #1985. [9] Prettyman T. et al. (2006) *JGR 111*, E002656.

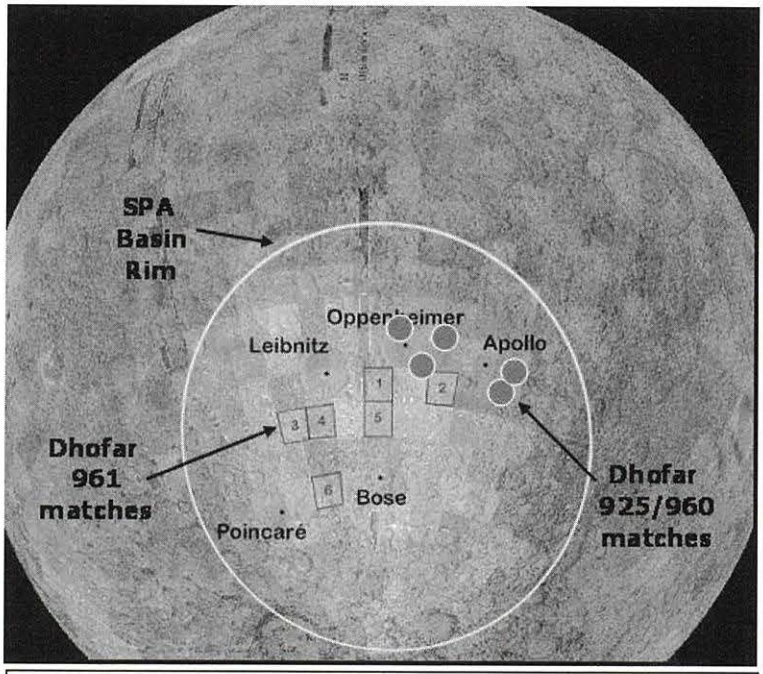

Figure 3: Locations of the best matches within the SPA Basin between the average composition of Dhofar 961 (numbered squares) and the average composition of Dhofar 925/960 (circles) with 5-degree LP-GRS data. Base image is a composite of shaded relief, Clementine 750 nm, and LP-GRS FeO map.

AUTHOR INDEX